

東京大学大学院新領域創成科学研究科

基盤科学研究系

先端エネルギー工学専攻

2004 年度修士論文

Characterization of
Post Laser Supported Detonation
by Interferometry

干渉法によるポストレーザー支持爆轟波の
特性解明

学籍番号 36209

氏名 福田 章雄

指導教員 小紫 公也 助教授

(2005 年 2 月 14 日提出)

Abstract

Clarifying the propagation mechanism of Laser Supported Detonation (LSD) wave is very important for efficient energy conversion from laser to blast wave in pulse-laser propulsion, which is a candidate of next low-cost launch system. The propagation of LSD wave is determined by physical parameters, for example, electron density and electron temperature, behind its wave front. However, the propagation mechanism has not been discussed quantitatively until now, as far as the author knows, because of the measurement difficulty, which is derived from two reason. One is that LSD wave has a small scale propagating with very high velocity ($M=5-30$), the other is that LSD regime has a high gradient structure about physical parameters such as electron density and electron temperature.

In this thesis, Mach Zehnder interferometry method was applied to measurement of electron density in LSD regime because 2-dimensional electron density profile could be obtained in only one measurement, that is, a reproducibility of phenomenon was not required so strictly. In this study, although the electron density in LSD regime could not be measured because a good contrast interference figure was not acquired due to the effect of refraction, the electron density in laser absorption regime after the LSD termination could be measured. As a result, the electron density in laser absorption regime after the LSD termination was found to hold near the critical density of incident laser for a moment after the LSD transition. In addition, the electron density distribution well matched with the plasma shape estimated from a shadowgraph image at the same time. Furthermore, the electron density decay process is found to be dominated by the effect of electron diffusion.

Finally, the electron density behind LSD wave front was calculated with experimentally measured velocity by using the simple one-dimensional LSD model in the assumption of chemical/thermal equilibrium. As a result, the calculated electron density in LSD regime was much lower than the experimentally measured electron density in laser absorption regime after the LSD termination. The disagreements between the calculated and experimental results pointed out that the assumption of a chemical/thermal equilibrium state in LSD regime is inappropriate.

Acknowledgements

The author would like to express his sincerest gratitude to Professor Kimiya Komurasaki (Department of Advanced Energy, University of Tokyo) for providing the scientific perspective to the author with his lively discussion and encouragement.

The author would like to express my sincere thanks to Professor Yoshihiro Arakawa (Department of Aeronautics and Astronautics, University of Tokyo) for his insightful advices.

The author gives his thanks to Dr. Koichi Mori (Institute of Fluid Science, Tohoku University), who told me how to use experimental apparatus and how to measure. Also the author gives his thanks to Dr. Hiroshi Katsurayama (currently JAXA) for his many advices about how to think the high temperature physics and about the way of computation.

The author is grateful to Mr. Yasuro Hirooka (Nissan Motor Corporation), who was his collaborator in this study and told him the principle of measurement method.

The author wishes to thank to Mr. Masato Ushio, who supports not only his research but also his life in this laboratory.

Also the author wishes to give his thanks to Mr. Hiroyuki Koizumi (the Department of Aeronautics and Astronautics, University of Tokyo), Dr. Makoto Matsui (Department of advanced Energy, University of Tokyo), Mr. Takayoshi Inoue (a doctor candidate at the Department of Aeronautics and Astronautics, University of Tokyo) for providing him their help and kindness.

Finally, the author wishes to thank all members in Arakawa laboratory and Komurasaki laboratory, the Univeristy of Tokyo, who provide a comfortable life as a researcher.

Table of Contents

Abstract

Acknowledgement

Table of Contents	4
List of Figures	6
Chapter1 Introduction	10
1.1 Background	10
1.1.1 Current and Future Launch System	10
1.1.2 Laser Propulsion	11
1.1.3 Air-breathing laser propulsion	12
1.1.4 Studies on Thrust Performance	13
1.2 Vision of Laser Propulsion System	16
1.2.1 Our Scenario of Flight Mode	16
1.2.2 Laser-transmitting base	19
1.3 Scope of This Study	20
1.3.1 Studies in our Laboratory	20
1.3.2 Laser Absorption and Blast Wave Generation Process	22
1.4 Objective	27
Chapter2 Measurement Method of electron Density	28
2.1 Intrusive Method	28
2.2 Nonintrusive Method	28
2.2.1 Emission Spectroscopy Method	28
2.2.2 Thomson Scattering Method	29
2.2.3 Interferometry Method	30
Chapter3 Theory of Mach Zehnder Interferometry	32
3.1 Principle of Mach Zehnder Interferometry	32
3.1.1 Coherency	32
3.1.2 System of Mach Zehnder Interferometry	32
3.1.3 Refractive Index	33
3.1.4 Fundamental Relationships of Fringe and its shifts	34
3.1.5 Abel Deconvolution	39
3.1.6 Way of Extracting Electron Density	40
3.2 Numerical Abel Deconvolution	41
3.2.1 Reasons for Using Numerical Abel Deconvolution	41

3.2.2	Computation of Abel Deconvolution	41
3.2.3	Performance of Program	41
3.3	Data Processing	51
3.3.1	Method to Count the Number of Fringe Shifts	51
3.3.2	Polynomial Fitting and Numerical Abel Deconvolution of Phase Data.....	53
Chapter4	Measurement Apparatus and Results	54
4.1	Experimental Apparatus	54
4.2	Imaging Optics	61
4.2.1	Light Source System	61
4.2.2	Built-up Imaging System	63
4.2.3	Time Synchronization System	66
4.3	Imaging Setup.....	67
4.4	Shadowgraph Images.....	68
4.5	Interference Images	69
4.6	Electron Density Profile.....	70
4.6.1	2-Dimentional Electron Density Profile.....	70
4.6.2	Comparison of the Plasma Shape.....	76
4.6.3	Radial Electron Density Profile	77
4.6.4	Longitudinal Electron Density Profile	77
4.6.5	Density Gradient and Peak Density at Plasma Front	79
4.6.6	Displacement of Post LSD front	81
4.7	Discussion	82
4.7.1	Peak Density Decay	82
4.7.2	Plasma temperature	82
4.7.3	Decay process	87
Chapter5	Calculation of electron Density behind LSD Front.....	88
5.1	Thermodynamic Relation.....	88
5.2	Thermodynamic Relationship.....	89
5.3	Chemical Equilibrium Calculation.....	90
5.4	Computational Results	92
5.5	Discussion	95
Chapter6	Conclusion	96

List of Figures

Figure 1.1 Schematic of different varieties of laser propulsion.	13
Figure 1.2 Performance of laser pulsejets in the atmospheric air	15
Figure 1.3 Performance of laser propulsions at reduced pressures.	15
Figure 1.4 Schematic of the three modes in the laser propulsion.....	17
Figure 1.5 100-kg-Vehicle trajectory through the three modes of laser propulsion in a vertical launch.....	18
Figure 1.6: Energy flow of laser-powered launch system.....	20
Figure 1.7 Engine cycle of laser pulsejet.....	21
Figure 1.8 Schematic of three ways of generating electron seeds, which is considered to be essential to the propagation of LSD wave.....	23
Figure 1.9: Shadowgraphs of $f = 2.2[E_i = 10 \text{ J}]$ in the atmospheric air,	25
Figure 1.10: Displacements of the shock front and plasma front.....	26
Figure 1.11: Schematic of LSD wave	26
Figure 3.1: Schematic of Mach Zehnder Interferometry.....	33
Figure 3.2:Schematic of an axisymmetric object.....	39
Figure 3.3 :Distribution $Q(x)$ obtained by integrating $f(r)$ by the line of sight	40
Figure 3.4:Original step function with no division in the discontinuously changing regime of $Q_I(x)$	43
Figure 3.5:Radial distribution applying Abel deconvolution to the test function $Q_I(x)$	43
Figure 3.6:Original and reconstructed distributions.....	44
Figure 3.7:Error distribution between the original and reconstructed distribution	44
Figure 3.8:original step function with ten equally-spaced divisions in the discontinuously changing regime of $Q_I(x)$	45
Figure 3.9:Radial distribution applying Abel deconvolution to the test function $Q_I(x)$	45
Figure 3.10:Original and reconstructed distributions.....	46
Figure 3.11:Error distribution between the original and reconstructed distribution	46
Figure 3.12:original step function with unequally-spaced 9 intervals in the discontinuous regime, which is obtained by eliminating one point from the discrete points in the test 2.	47
Figure 3.13:Radial distribution applying Abel deconvolution to the test function $Q_I(x)$	47
Figure 3.14:Original and reconstructed distributions.....	48
Figure 3.15:Error distribution between the original and reconstructed distribution	48
Figure 3.16:Original step function with ten equally-spaced divisions in the discontinuously changing regime of $Q_I(x)$	49
Figure 3.17:Radial distribution applying Abel deconvolution to the test function $Q_I(x)$	49

Figure 3.18:Original and reconstructed distributions.....	50
Figure 3.19:Error distribution between the original and reconstructed distribution	50
Figure 3.20: Typical interference pattern in our measurement.....	51
Figure 3.21: The way of counting the fringe shift number from obtained interference pattern ..	52
Figure 4.1: Picture of TEA CO ₂ laser. (a) Exterior of IRL-1201, (b) laser-discharge tube and gap-switch	55
Figure 4.2: Electrical circuit for the TEA CO ₂ laser.	56
Figure 4.3: Relation between the laser pulse energy and the fill-pressure in the laser-discharge tube.....	56
Figure 4.4: Photon-drag detector	57
Figure 4.5: Laser pulse shape typical for IRL-1201.	58
Figure 4.6: Relation between the decay-constant at the exponentially-decaying tail and the fill pressure in the laser discharge tube.....	59
Figure 4.7: Off-axial parabola mirror.....	60
Figure 4.8: Schematic of laser light system	61
Figure 4.9: Picture of experimental setup of light source system	62
Figure 4.10: Picture of ICCD camera	65
Figure 4.11:Schematic of InstaSpec TM V Head.....	65
Figure 4.12:Image of Delay Generator	66
Figure 4.13: Imaging Setup.....	68
Figure 4.14:Shadowgraphs in the atmospheric air.	69
Figure 4.15:Interferograms in the atmospheric air.	70
Figure 4.16:2-dimentional electron density profile. $t=3.75\mu s$	71
Figure 4.17:2-dimentional electron density profile. $t=4\mu s$	71
Figure 4.18: 2-dimentional electron density profile. $t=4.25\mu s$	72
Figure 4.19: 2-dimentional electron density profile. $t=4.5\mu s$	72
Figure 4.20: 2-dimentional electron density profile. $t=4.75\mu s$	73
Figure 4.21:2-dimentional electron density profile. $t=5\mu s$	73
Figure 4.22:2-dimentional electron density profile. $t=5.25\mu s$	74
Figure 4.23:2-dimentional electron density profile. $t=5.5\mu s$	74
Figure 4.24:2-dimentional electron density profile. $t=5.75\mu s$	75
Figure 4.25:2-dimentional electron density profile. $t=6\mu s$	75
Figure 4.26:Comparison of the shape of the plasma judged from the shadowgraphs image (a) with the shape of the electron distribution judged from interference figure(b)	76
Figure 4.27: Typical radial electron density profile	77
Figure 4.28 : Geometric relationship between the laser axis and assumed axis for the electron	

density profile	78
Figure 4.29: Longitudinal distribution of the electron density over a cross section in the laser induced plasma in air at different time	78
Figure 4.30: Variation of the electron density gradient at the plasma front	79
Figure 4.31: Variation of the peak electron density at the plasma front	79
Figure 4.32: Variation of the Averaged Electron Density in the longitudinal direction in the case of $E_i=10\text{J}$, $f=2.2$, atmospheric pressure	80
Figure 4.33: Definition of the width of the laser absorption regime after LSD termination	80
Figure 4.34: Variation of the width of the laser absorption regime after LSD termination	81
Figure 4.35: Displacement of the shock front, emission front and laser absorption wave front after the LSD termination	81
Figure 4.36: Self-similar solution of the strong point explosion	83
Figure 4.37: Longitudinal distribution of the plasma temperature over a cross section in the laser induced plasma in air at different time	83
Figure 4.38: Variation of the averaged plasma temperature on the longitudinal axis	84
Figure 4.39: Laser power density irradiated on the plasma surface during the laser absorption regime after the LSD termination	85
Figure 4.40: Characteristic time of the energy loss by bremsstrahlung radiation with the plasma temperature fixed to 15000K	85
Figure 4.41: Calculated electron density with some pressures in the wide range of the temperature	86
Figure 4.42: Distribution of the electron density and the pressure in the assumption of the strong point explosion at $t = 4.25[\mu\text{s}]$	87
Figure 5.1: Schematic of one dimensional LSD model	88
Figure 5.2: Measured history of LSD wave displacement	92
Figure 5.3: Measured history of the velocity of LSD wave with $f=2.2$	93
Figure 5.4: Calculated history of the electron density behind LSD wave front with the focusing lens with $f=2.2$ in atmospheric air and the critical density of the electromagnetic wave, which wavelength is $10.6\mu\text{m}$	93
Figure 5.5: Calculated history of the temperature behind LSD wave front with $f=2.2$ in atmospheric air	94
Figure 5.6: Calculated history of the laser power density irradiated on LSD wave front	94
Figure 5.7: Calculated history of the mole fraction behind LSD wave front with $f=2.2$ in the atmospheric air	95

List of Tables

Table 1.1 Assumption for the 100-kg-Vehicle trajectory calculation for the velocity increment	17
Table 1.2 High-power laser characteristics	19
Table 1.3 :The past studies for the air-breathing laser propulsion in our laboratory since 1999.	22
Table 1.4: LSD threshold using different values of E_i and f	27
Table 2.1: Comparison of $n_e I$ needed for the one fringe shift in using various type of the laser.	31
Table 2.2: Comparison of the popular methods for measuring electron density,	31
Table 4.1: Specification of TEA CO ₂ lasers	55
Table 4.2: Specification of Photon-drag detector (Hamamatsu photonics, B749).	58
Table 4.3:Comparisons of applicable light sources classified by the observed region and observing method.....	63
Table 4.4: Comparisons of the applicable lens classified by the conjugate ratio	63
Table 4.5:Specification of optical equipments	67
Table 5.1:Chemical equations used in the equilibrium calculation in air with 11 species	91
Table 5.2: Numbers of the fundamental element c in species s	91

Chapter1

Introduction

1.1 Background

It has been passed nearly half century since human beings first ventured out into the unknown and curious world, the space. Although various missions are planned and executed all over the world during this long time, access to the space still now accompanied various problems. One of the problems is a very high cost for sending a load to the space. The high cost is mainly stemmed from the complexity of launch vehicle system and very low payload ratio. In such a situation, laser propulsion is attracted as one of the next launch system, which would realize low cost launch and high payload ratio.

1.1.1 Current and Future Launch System

The area of our activities in the space has been expanded until today since 1958, when the Sputnik was launched in former Soviet Union. A lot of space satellites and space-exploration vehicles have been launched in many countries and provided us various benefits. These make it possible to observe the Earth, which informs us the weather and the environment, and to communicate with people at any place in any time, which is used as satellite broadcasting etc. Manned space vehicles also have been launched and provided us various benefits. These make it possible for scientists to experiment with various themes in the microgravity environment, which would give us new materials, and for doctors to study the effects of space environment on a human body, which will become a precious medical information in our future space life.

In this way, the steppingstone for future manned activities in the space has continued to be steadily constructed. On the other hand, a lot of attracting space developing plans, for example, space factory¹, Solar Power Station², and homeostasis lunar base³, is proposed until today, though most of these plans were scraped because of the high launch cost.

The launch vehicles could be classified into two styles: Expendable Launch Vehicles (ELV) and Reusable Launch Vehicles(RLV). ELV requires the quite heavy systems, so the payload whose weight launched to the Low Earth Orbit(LEO) is less than 4%.⁴ In addition, ELV are once-only launch vehicles, so the launch cost is as high as 5000(\$/kg).⁵ On the other hand, RLV are possible to be launched over and over. Although RLV has been developed to reduce the launch cost through reutilization, the launch cost is much higher than RLV because of the system of RLV is more complex.

One of the future RLV vehicles is the space plane, which is expected to the great reduction of oxidant on board by the scramjet engine loading because oxygen is supplied from an air.⁶ However, in practice, the effective combustion technology in the scramjet engine has not established yet in spite of its long study. In such uncertainty, many countries have ceased its development. In addition, if the technology of the scramjet engine were established, space plane could become the high cost

launch system as well as Space Shuttle.

1.1.2 Laser Propulsion

Laser propulsion is a candidate for low-cost launching system, and can be considered as the mass driver, in which the vehicle is accelerated by the laser power transmitted remotely from the ground-based or space-based laser. Laser propulsion was first proposed by Kantrovitz in 1972 soon after the invention of laser.⁷ To his proposal, many studies on the laser propulsion were activated especially in U.S.A, Russia, Germany and Japan.

Laser propulsion uses laser energy to thrust, which is very different from the chemical propulsion which uses the combustion energy, the electric propulsion which uses the electromagnetic energy, Laser propulsion is classified into the following two modes according to the laser transmission mode.

<CW laser propulsion>

One kind of laser propulsion is CW laser propulsion which uses the continuous wave laser. CW laser beam focused in the engine generates Laser Sustained Plasma (LSP) and maintained by the laser energy absorption through the inverse bremsstrahlung process. LSP supplies its enthalpy to the cold propellant gas, which flows around LSP. The heated propellant gas passes through the throat and expands in the nozzle. In this expansion stage, the gained enthalpy is converted into the kinetic energy. In this way, thrust generates.

CW laser propulsion is considered to be applied to the transitions between the orbits and the attitude control in the space because the CW laser, which power is presently several KW class, is not enough to launch the vehicles from the ground. Applying CW laser propulsion in the space has the advantage that various propellant gases could be selected freely.

<RP laser propulsion>

Another kind of laser propulsion is RP laser propulsion which uses the repetitive pulse laser. Pulse laser beam focused in the ablator on board or in the air generates laser induced plasma and blast wave. The flow energy converts into the thrust. The details on the process of this thrust generation describe in the section 1.3.1. RP laser propulsion is considered to be applied to the ground launch system because the RP laser, which power is presently several MW class, is considered to generate more thrust relative to the CW laser propulsion in terms of the laser power. By comparison with the chemical rocket, applying RP laser propulsion to ground launch system has the advantages that there is no need to be the complex and heavy propulsion systems on board because laser energy is transmitted from the base located in the space or on the ground. In addition, the air-breathing laser propulsion, which propellant is an air, has another advantage that it does not need to consume the fuel on board, so high payload ratio could be realized.

This study is focused on air-breathing RP laser propulsion, so, in the following sentences, laser propulsion means the air-breathing RP laser propulsion.

1.1.3 Air-breathing laser propulsion

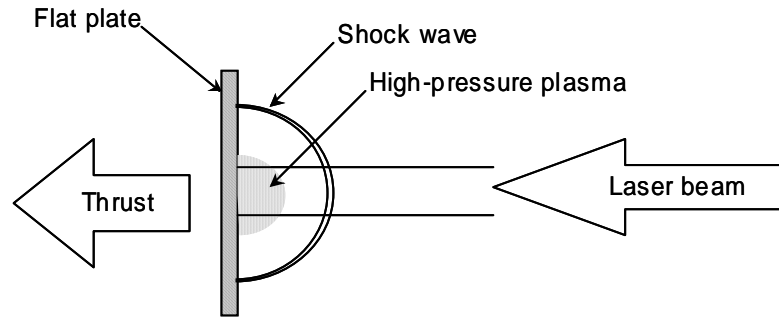
Although Kantrovitz proposed laser ablation rocket, in which laser beam is irradiated to an ablator on board to produce thrust, air breathing laser propulsion is more advantageous than the ablation rocket because it does not consume fuel on board. Therefore, a lot of studies about laser propulsion have been concentrated on the air-breathing mode.

From 70's through 80's, many studies were performed for 'flat-plate' type.^{8 9 10 11} Intense laser beam was irradiated on a metallic plate surface in the atmospheric air to produce a high-pressure region on the surface as illustrated in Fig. 1.1 (a).^{1 2}

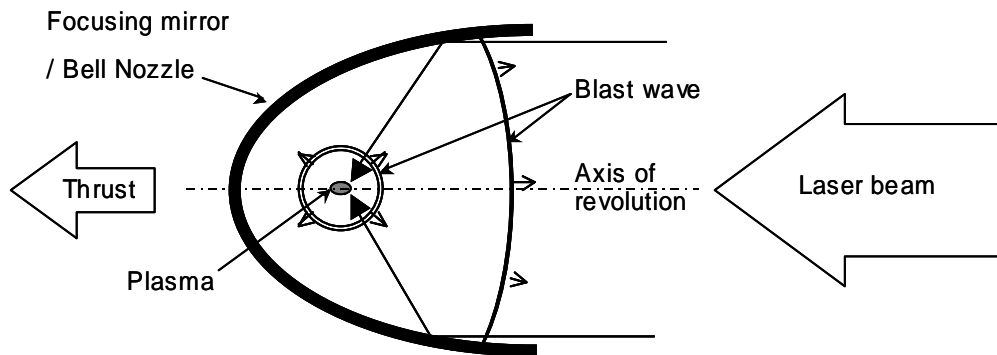
Pirri et al. first studied laser pulsejet with a bell nozzle illustrated in Fig. 1.1 (b). The laser beam was focused by a parabola mirror to produce plasma. Expansion of the plasma drives a spherical blast wave in the surrounding air, and impulsive thrust is generated on the nozzle wall while a blast wave expands in the nozzle. Ageev et al. also studied the laser pulsejet experimentally using a parabola and a conical nozzle with a 5-J-pulse CO₂ laser.^{1 3} In DLR (German Aerospace Center), a 53-g-Bell nozzle was launched to 60 cm high using a repetitive pulse laser whose average power was 7.9 kW (laser pulse energy was 175 J/pulse and repetition frequency was 45 Hz).^{1 4}

In 1998, Myrabo et al. published the results of their flight demonstrations using a 10-kW-class repetitive pulse CO₂ laser.^{1 5} Their demonstrations were world first, and recent researches on laser propulsion were activated by their report. A 'Lightcraft' used in the demonstrations is illustrated in Fig. 1.1 (c). An impulsive thrust is imparted on a spike nozzle, which focuses laser beam onto a cowl to produce plasma. Its mechanisms of impulse generation are same with those in the laser pulsejet though the geometry of focusing optics is different from the Bell type nozzle. One remarkable feature of the Lightcraft design is a front intake from which the air is taken and compressed.

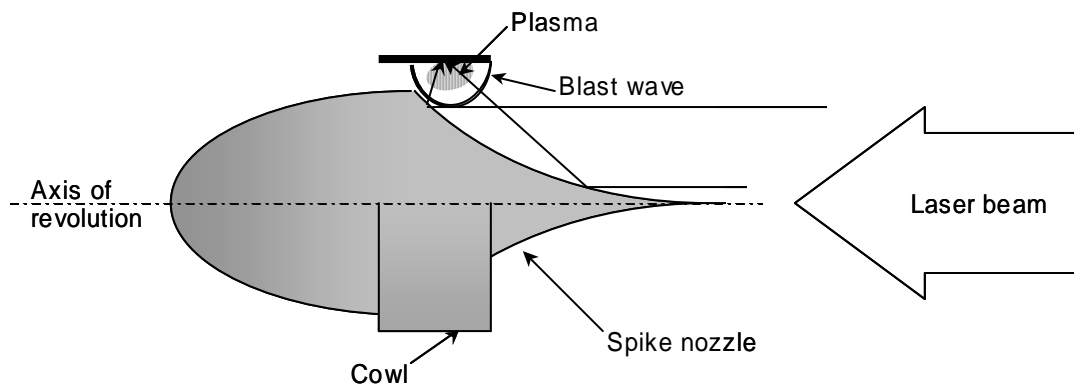
A Laser In-Tube Accelerator (LITA)^{1 6} is another variety of laser propulsion. LITA is a laser-driven ram accelerator where a projectile is accelerated by successive laser-induced explosions in a tube filled with a rare gas. Its thrust generation mechanisms are also quite similar to those of the laser pulsejet.



(a) Flat plate type laser propulsion



(b) Laser pulsejet with a Bell nozzle



(c) Lightcraft designed by Myrabo

Figure 1.1 Schematic of different varieties of laser propulsion.

1.1.4 Studies on Thrust Performance

Single-pulse performance of the air-breathing pulse laser propulsion has measured experimentally. The parameter evaluating the performance is the momentum-coupling coefficient C_m , which is

defined as the ratio of the impulse I and the irradiated laser pulse energy:

$$C_m \equiv \frac{I}{E_i}$$

Fig1.2. shows experimentally measured C_m for the various thruster configurations as a function of laser pulse energy E_i . All the experiments were performed in the atmospheric air using CO_2 pulse laser. The laser pulsejet with the bell nozzle is recorded the best performance in the other configurations, and C_m increase with the laser energy E_i . On the other hand, C_m of the flat-type thruster decreased with E_i .

The ambient air pressure is the one of the important parameters in determining the performance of the laser propulsion. Bohn et al. measured C_m of Bell type laser- pulsejet in the air at reduced pressure as shown in Fig.1.3. C_m was found to decrease monotonously with the decrease in the ambient pressure p_a with either laser pulse energy.

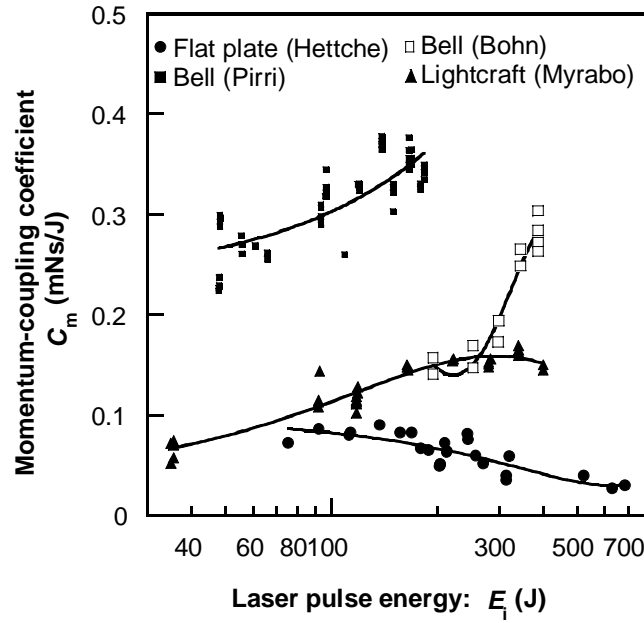


Figure 1.2 Performance of laser pulsejets in the atmospheric air:relation between the momentum coupling coefficient C_m and the laser pulse energy E_i for a given nozzle design (reproduced after Hettche et al.,⁷⁾ Myrabo et al.,¹⁷⁾ and Wang et al.¹⁸⁾ C_m is affected both by laser pulse energy.

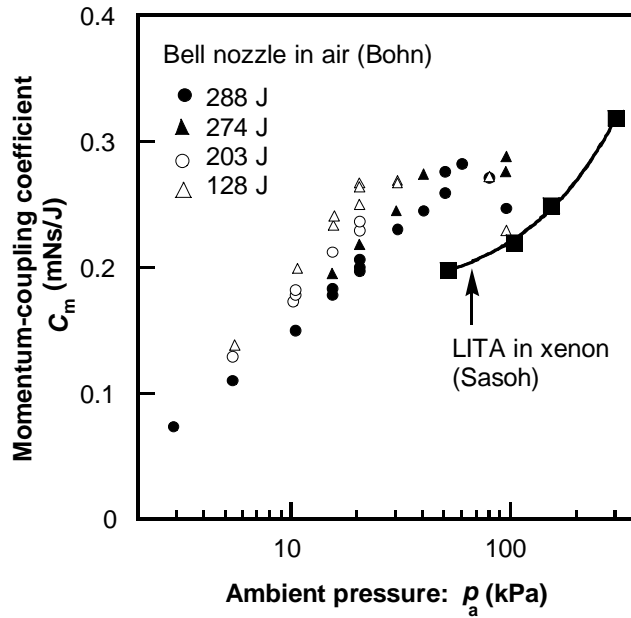


Figure 1.3 Performance of laser propulsions at reduced pressures (reproduced after Bohn et al.¹⁹⁾ and Sasoh et al.²⁰⁾). Bohn et al. measured C_m using a parabolic Bell nozzle in a vacuum chamber. Sasoh et al. measured C_m using a Laser In-Tube Accelerator (LITA) with xenon gas; C_m apparently decreased with the decrease in the ambient gas pressure in both cases despite the difference in the ambient gas composition.

1.2 Vision of Laser Propulsion System

Our perspective of the total system of air-breathing laser propulsion, the flight mode and laser-transmitting base are introduced in this section.

1.2.1 Our Scenario of Flight Mode

The laser-powered launch system would be applicable to the material supply for the construction of a Solar Power Satellite, for example. Our scenario of launch is introduced here to survey the overall picture of the system. Payload is launched through three modes; Laser pulsejet, laser ramjet, and laser rocket, as shown in Fig.1.4. Near the ground, the vehicle is accelerated until the velocity of the vehicle reach to $M=2$. This mode is called laser pulsejet. When the velocity of the vehicle reach to $M=2$, the air intake open and the air is drawn in at the front of the vehicle and compressed to compensate the reduction of the ambient pressure. This mode is called ramjet mode. In ramjet mode, compared to the pulsejet mode, the time to exhaust and refill air in the nozzle is much shorter because the intake flesh air sweep away the high-temperature and low-pressure air toward the rearward of the vehicle. Therefore, compared to the laser pulsejet mode, the laser pulse could send to the vehicle with high frequency in the ramjet mode. The rocket mode is initiated at the altitude where the adequate air pressure can not be acquired through the ram compression. In the rocket mode, the hydrogen on board is injected into the nozzle is injected into the nozzle with the pressure of the propellant tank higher than the pressure of the nozzle. and used as the working fluid.

The velocity increment by the laser propulsion at 10 km/s is required to launch a payload to GEO. An engine cycle analysis was adapted to the estimation of the thrust performance, and the specifications of the engine model are summarized in Table 1.1. Figure 1.5 shows the vehicle trajectory calculated by Katsurayama et al.²¹ for the vertical launch.²⁴⁾ A vehicle is gradually accelerated through a trajectory from the sea-level up to 200 km above sea level, and it will not suffer from excessive aerodynamic heating and load. A 100-kg-vehicle was accelerated to 10 km/s in one minute, and the payload ratio of the vehicle was 0.6.

Table 1.1 Assumption for the 100-kg-Vehicle trajectory calculation for the velocity increment

Transmitted Laser	Average power (MW)	500
Vehicle	Initial mass (kg)	100
	Structure coefficient	0.1
Pulsejet mode	C_m (N/MW)	100
Ramjet mode	Absorption efficiency (%)	40
	Diffuser efficiency (%)	97
Rocket mode	Absorption efficiency (%)	40
	Propellant Specific impulse (s)	H_2 ~ 950

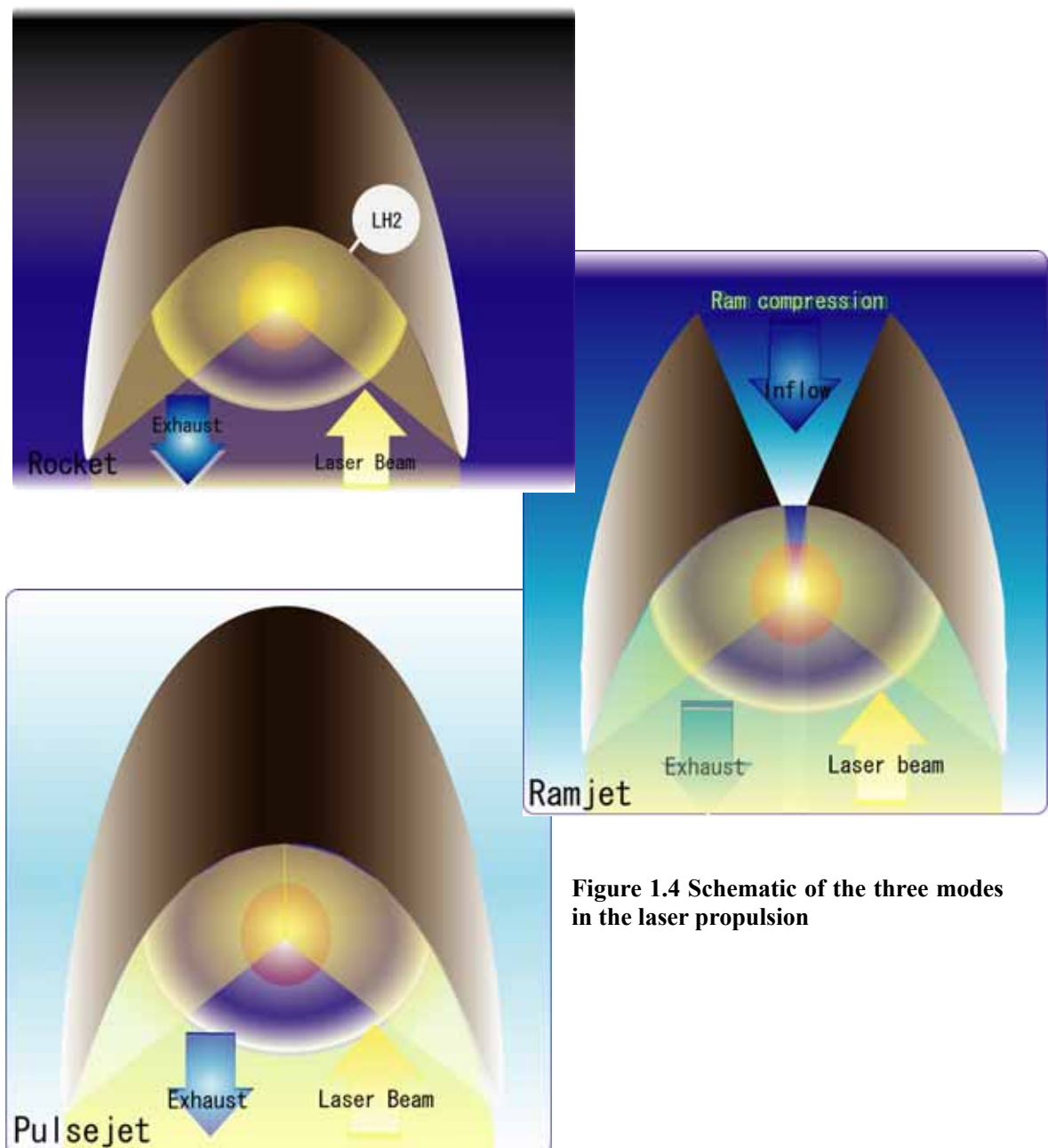


Figure 1.4 Schematic of the three modes in the laser propulsion

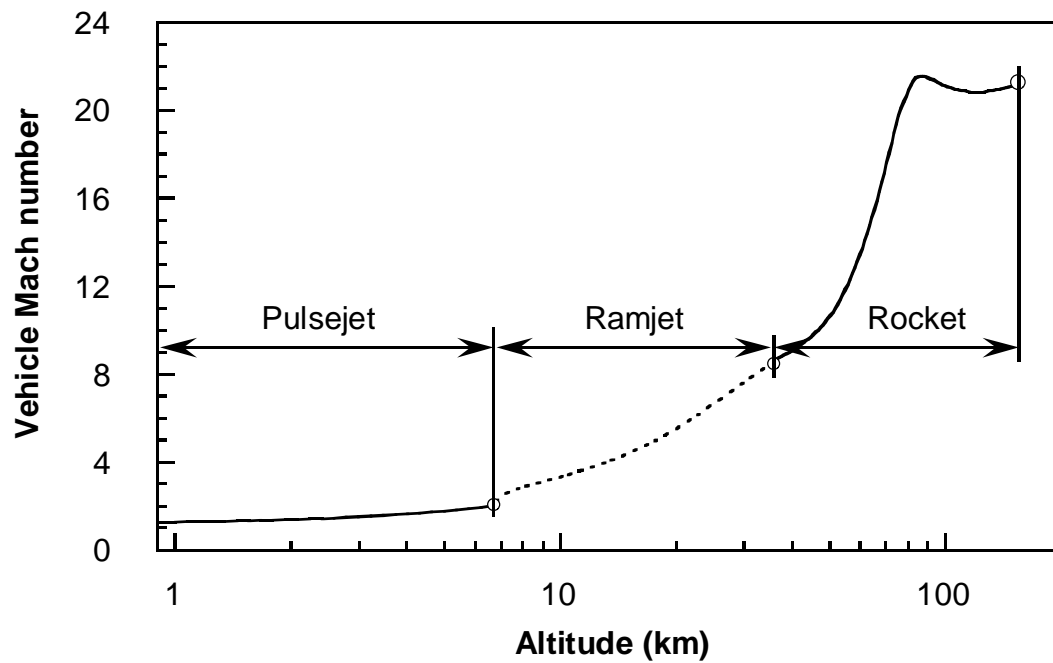


Figure 1.5 100-kg-Vehicle trajectory through the three modes of laser propulsion in a vertical launch; Final velocity increments was set at 10 km/s, and payload ratio was calculated at 0.6 from this trajectory estimation.

1.2.2 Laser-transmitting base

High power laser system

High-power-laser candidates

Typical characteristics of the high-power lasers are summarized in Table 1.2. CO₂ laser is one of the typical high-power gas lasers. A high-power CO₂ laser, whose laser pulse energy has become up to 1 kJ, has been realized today.^{2 2} In addition, the repetition frequency of laser pulse has approached 1000 pulse per seconds with the recent advances in the diode switch and Magnetic Pulse Compression (MPC) techniques.^{2 3} A high-average-power pulse CO₂ laser is within the scope of practical use. Typical Diode-Pumped Solid State Laser (DPSSL) is Nd:YAG or Nd:Glass laser. Although Nd:Glass laser is used for the inertial confinement thermonuclear fusion experiments, typical average power of DPSSL has been much lower than the CO₂ laser. High-power laser diodes (LD) have been developed in recent times. In order to put out high-power, many laser diodes should be arrayed in two-dimensional. Its remarkable advantage is high energy-efficiency. The problem of the arrayed LD is its poor beam quality. As for the beam quality, the gas-laser is generally more advantageous than the solid-state lasers. Typical beam quality factor M^2 of CO₂ lasers is lower than 2.0, and the Nd:YAG lasers, in the order of 100 with average power at 1 kW.^{2 4} In addition, a CO₂ laser beam at the wavelength of 10.6 μm is absorbed slightly on the way of transmission through the atmosphere. To these considerations, CO₂ lasers are the most promising driver for the laser propulsion.

Table 1.2 High-power laser characteristics

Laser	CO ₂	DPSSL (Nd)	Arrayed LD
Wave length (μm)	10.6	1.06, 0.53	0.8 - 1
Efficiency (%)	< 20	< 22	< 70
Average power (kW)	100	7.2	2.5 (/cm ²)
Pulse energy (J)	1000	20	-

High power generation system

For a single launching in one minute, laser energy of 30 GJ is released, and total electric energy of 150 GJ (42 GWh) should be transmitted to the CO₂ laser facilities. In order to avoid the disturbance in commercial electric power generation systems, an energy storage system is required. The superconducting magnetic energy storage (SMES) is most attracting for this purpose. SMES is now on the developing stage for the use of the compensation of large load fluctuations, for examples in linear motor cars and steel plants. It will be applicable to the storage energy between 10 to 600 MWh, and its efficiency will approach more than 90 %. Figure 1.6 shows the energy flow of the over-all systems. The heat rejection from the laser should become an important problem. The heat from the

laser might be used to regenerate the electrical energy using a steam turbine, and the over-all energy efficiency might be improved though such a combined laser system has not been developed until today.

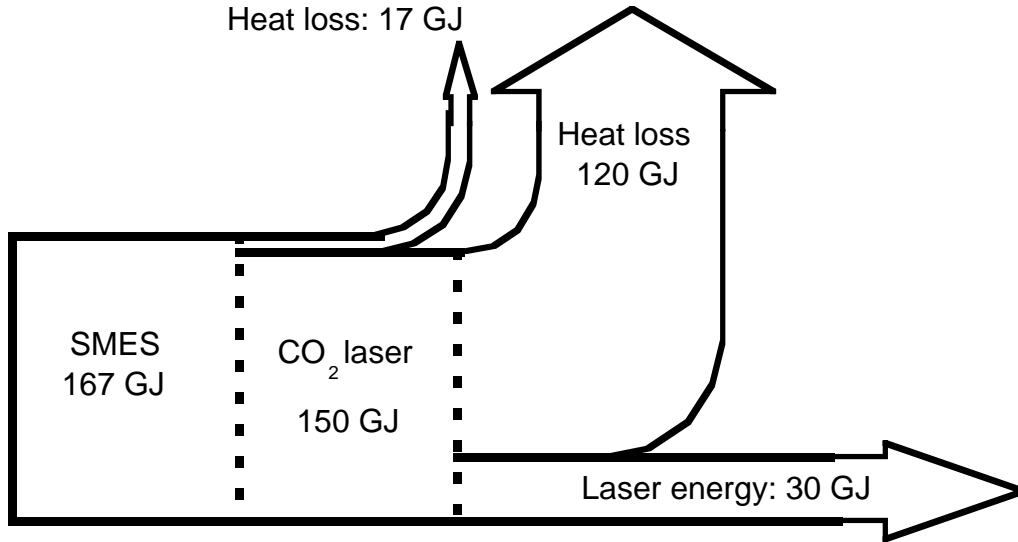


Figure 1.6: Energy flow of laser-powered launch system.

1.3 Scope of This Study

The total impulse generation processes are divided into four process: (1)Laser absorption and Blast wave energy conversion process, (2)Blast wave expansion process, (3)Impulse generation process and (4)Refill process. Laser absorption and blast wave energy conversion process has not clarified yet. To understand laser absorption and blast wave energy conversion mechanism, the physical parameters of the laser absorption layer such as the electron density and the electron temperature are very important.

The purpose of this study is to evaluate the electron density profile behind the blast wave and to clarify the characteristics of plasma density in the absorption regime.

1.3.1 Studies in our Laboratory

As illustrated in the previous section, air-breathing pulse-laser propulsion will be a promising mass driver. However the thrust performance was modeled simply in conventional analyses because we do not have a scaling law of thrusters. In order to further enhance the thrust performance and reduce the infrastructure cost, clarifying the processes determined the thrust performance are needed..

As illustrated in Fig.1.7, the total impulse generation processes are divided into four processes:

- 1 . Laser absorption and Blast wave energy conversion process
- 2 . Blast wave expansion process,
- 3 . Impulse generation process.
- 4 . Fulfill process

In the laser absorption and blast wave energy conversion process, the thrust performance is influenced by the specification of the laser, the geometric focusing optics, and the atmospheric conditions. On the other hand, in the following impulse generation processes, it is influenced mostly by the nozzle shapes.

In our laboratory, the processes have been studied experimentally and numerically. The past studies are tabled as Table 1.3. The number added to the head of each experiment and calculation column in Table 1.3 corresponds to the thrust generation process number shown in Fig1.7.

It should be noted that the laser absorption and blast wave generation process in the laser pulse jet is essentially same with those in the laser ramjet and laser rocket. In addition, this process has primary importance in the laser propulsion studies because it firmly fixes the maximum thrust performance.

The laser absorption and blast wave generation processes are the main of this study in four processes, so this process is described in the following section in detail.

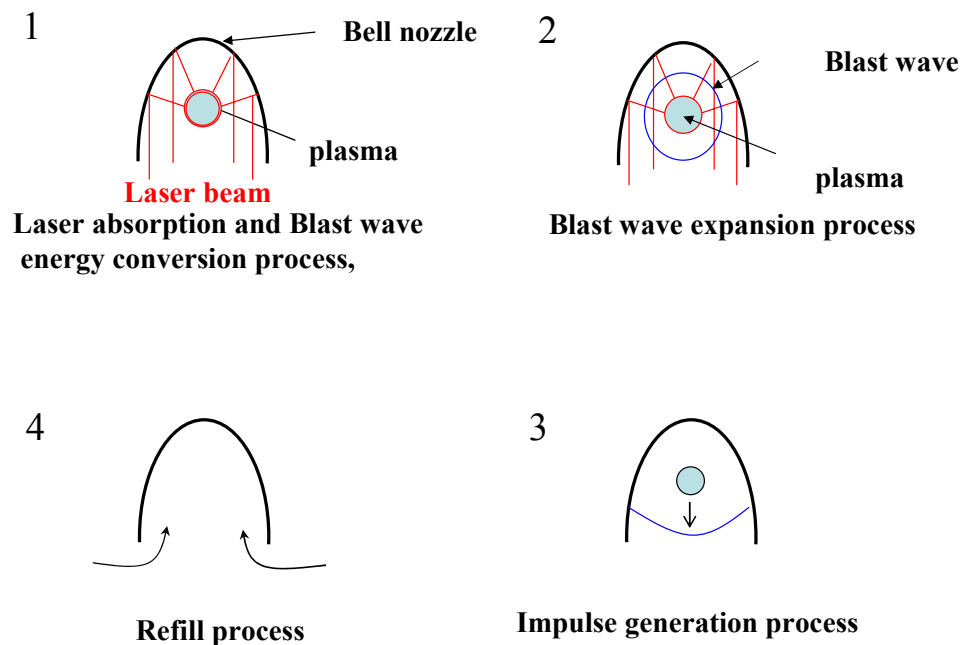


Figure 1.7 Engine cycle of laser pulsejet

Table 1.3 :The past studies for the air-breathing laser propulsion in our laboratory since 1999

<Pulsejet mode >

Year	Experiment	Calculation
1999	(1)Visualization of the plasma in the atmospheric pressure ^{2 5}	(2)Propagation of the blast wave by the 1-dimentional model
2000	(3)Measurement of the pressure of the blast wave ^{2 6}	-
2001	(1)Measurement of the electron temperature and density by the emission spectroscopy ^{2 7}	-
2002	(4)Measurement of the Cm using the conical nozzle thruster ²⁵	(4)Exhaust and refill process in the conical nozzel ^{2 8}

<Ramjet mode>

Year	Experiment	Calculation
2000	(1)Visualization of the plasma in the M=2 flow ²⁵	(2&3)Thrust performance of the light craft using 2-dimentional model ^{2 9}

<Rocket mode >

Year	Experiment	Calculation
2004	-	(1)Propagation of LSD wave in the hydrogen with simple LSD model ²⁹

<System>

Year	System
2003	Evaluation of the total performance of the laser propulsion system ^{29,3 0}

1.3.2 Laser Absorption and Blast Wave Generation Process

Initiation of break down

Laser breakdown of the atmospheric air is initiated by focusing an intense laser pulse. The power density threshold for the breakdown was measured at the order of 10^9 - 10^{10} W/cm² using CO₂ laser.

Laser breakdown process and laser-induced plasma generation process are as follows.^{3 1} In the first stage, N₂ and O₂ molecules in the air are ionized by the multiphoton absorption which occurs when the simultaneous absorption energy of n photons, $n h \mu$, exceeds the ionization potential. The minimum ionization energy of O₂ is 12.5eV and N₂ is 15.8eV, so it could be estimated as $n=11$ for O₂ and $n=14$ for N₂ in CO₂ laser. The electron which generate in this first stage are called the first generation electron. In the second stage, the first generation electron is accelerated by the inverse-bremsstrahlung effect and remove electrons from the other molecules and atoms. In this way, an electron avalanche develops. When the characteristic length of the ionization regime is parallel to the Debye length, a laser-induced plasma generates.

Laser absorption process

After the laser induced-plasma is generated, the intense laser beam continues to be irradiated on the surface of this plasma. The laser energy is absorbed by this plasma mainly through the inverse bremsstrahlung process. It is well known that the laser absorption mechanism is classified into two

regimes. At laser power densities greater than the order of 10^7 W/cm^2 , laser absorption occurs in Laser Supported Detonation (LSD) regime.^{3 2, 3 3, 3 4} On the other hand, at power densities lower than 10^6 W/cm^2 , it occurs in Laser Supported Combustion (LSC) wave. LSD wave travels at a supersonic velocity along the laser light channel in the direction opposite to the beam incidence. Although the mechanism of LSD wave propagation is not still clarified, existing an electron seed in the front of the strong laser absorption regime are considered to be essentially important. The electron seed is considered to be produced by mainly three effects, SHOCK compression effect, electron diffusion effect and photoionization or photoexcitation effect as shown in Fig.1.8. The dominant effect in three effects is determined by the laser power density irradiated on LSD front.

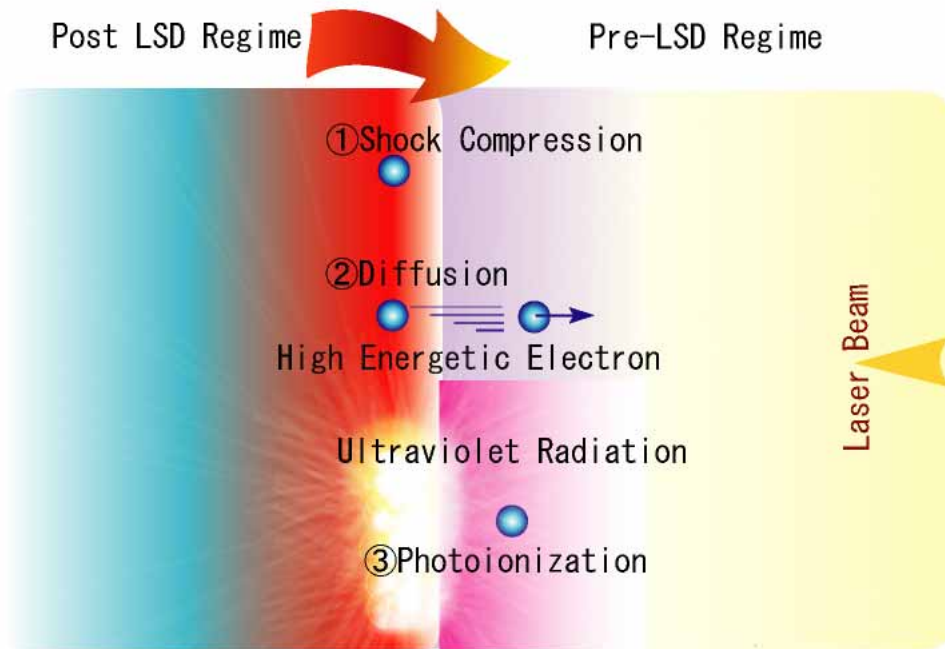


Figure 1.8 Schematic of three ways of generating electron seeds, which is considered to be essential to the propagation of LSD wave

Similarly to the chemical detonation wave, LSD wave is thought to have a Zel'dovich-Nuemann-Doring (ZND) wave structure, in which cold gas ahead of the wave is compressed and heated in a shock front called the von-Neumann spike.^{3 5}

In general, very high temperature region radiate the ultraviolet-ray. The high energetic photon emitted from this region could directly remove or excite the electron of the molecules in the cold gas ahead of the thermal boundary layer. This is called photoionization and photoexcitation. The speed of the propagation of the discharge front is very high and in the hydrogen at 40pa, the speed is estimated to be 10^6 m/s .^{3 6} Photoionization and photoexcitation is appeared in the radiation

detonation phenomenon, for example, in the extraordinary explosion.

In LSD regime, very high energetic electrons, which are distributed in the foot of electron distribution function, are considered to exist. By the diffusion of the high energetic electrons, the laser absorption precursor is generated ahead of LSD front. This effect is reported to be essential to generate LSD wave in room temperature by Shiraishi.^{3 7}

The laser beam irradiated on LSD front could be reflected because the electron density in such a strong absorption regime would be near to the critical density for the incident laser beam. By principle of superposition, the reflected wave and the incident wave make the composite wave, which amplitude is twice as much as each one and which electromagnetic energy is four times as much as each one. In this high electromagnetic energy, the cold gas ahead of LSD front occurs breakdown by multiphoton effect and this regime become new absorption regime.

In the LSC regime, laser absorption occurs in plasma mostly at uniform pressure. The absorption wave has a structure similar to a deflagration wave: it is called an LSC wave. The wave propagates in the direction opposite to beam incidence at a subsonic velocity due to heat conduction. After cold gas ahead of the wave is heated and ionized through heat conduction, it expands to absorb the laser beam.

The propagation of LSD regime terminates when the laser power density on the LSD wave front decreases to LSD threshold. Since CO₂ laser beam is absorbed mostly by the electrons through the inverse-bremsstrahlung process, and the fractional absorption of laser power correlates closely with electron density in the absorption layer. During the propagation of LSD wave, the shock wave interacts with the laser absorption region, and the irradiated energy is delivered efficiently to the motion of the surrounding air through the expansion work of the plasma. On the other hand, the laser energy absorbed in laser absorption regime after the LSD termination cannot generate a high pressure wave and has no contribution to the increment in the energy of the surrounding air motion. The laser energy absorbed in laser absorption regime after the LSD termination may be converted into the radiation energy and the internal energy frozen in the plasma region.

Here, the LSD regime absorption efficiency η_{LSD} as the fraction of the laser energy irradiated during LSD regime to the total laser pulse energy is introduced as follows

$$\eta_{LSD} \equiv \frac{\text{Cumulative energy irradiated to LSD wave}}{\text{Total laser pulse energy}}. \quad (1-1)$$

Larger duration of LSD existence in using the same laser system brings higher energy conversion efficiency from the laser pulse energy to the energy of the surrounding air motion.

Mori investigated systematically the LSD termination with different value of focusing f-number, laser energy and atmospheric pressure by using shadowgraph method.^{3 8} Figure 1.9 shows the shadowgraphs of an exploding plasma and blast wave induced by a 10-J-CO₂-laser. Figure 1.10 shows the displacement of the shock front and the plasma front from the focus in the direction

opposite to the laser incident channel. The coincident of each front occurs during LSD regime. After LSD regime termination, the shock front propagates further and the plasma front stays. The intersection point of the two curves indicates the timing of the transition from LSD regime to LSC regime.

Laser Power density on the LSD wave-surface S is expressed as

$$S = \frac{W}{\pi r_{LSD}^2} \quad (1.2)$$

where W is the laser power and r_{LSD} is the radius of the LSD wave-surface front as shown in Fig.1.11. r_{LSD} is defined as

$$r_{LSD} = \frac{z_{LSD}}{2f} \quad (1.3)$$

The LSD threshold for the regime transition is summarized in Table 1.4 , where E_i is the pulse laser energy. Although this threshold is found to increase with f and decrease with E_i , it is found to be relatively insensitive to the f -number

Although the LSD termination is evaluated by the shadowgraph method, the plasma parameters, such as electron temperature and electron density, is still unknown. Knowing these parameters is essential to clarify the physical mechanism of the LSD wave propagation. Harabe measured the electron density and the electron temperature using the emission spectroscopy method²⁷, the measured value is the averaged value over the plasma volume and many assumptions are introduced. Therefore, the physical structure of the LSD regime, which has the very small scale, could not be discussed in detail.

The objective of this thesis is to characterize the absorption regime by measuring the electron density profile using interferometric method with high spatial resolution.

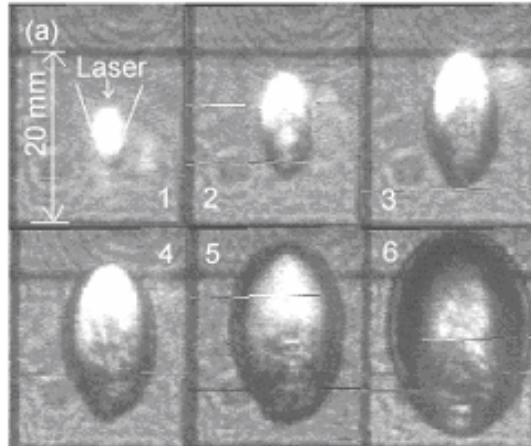


Figure 1.9: Shadowgraphs of $f = 2.2$ [$E_i = 10$ J in the atmospheric air, (1) $t = 0.25$, (2) 1.0, (3) 2.0, (4) 3.0, (5) 4.0, (5) 6.0 μ s]

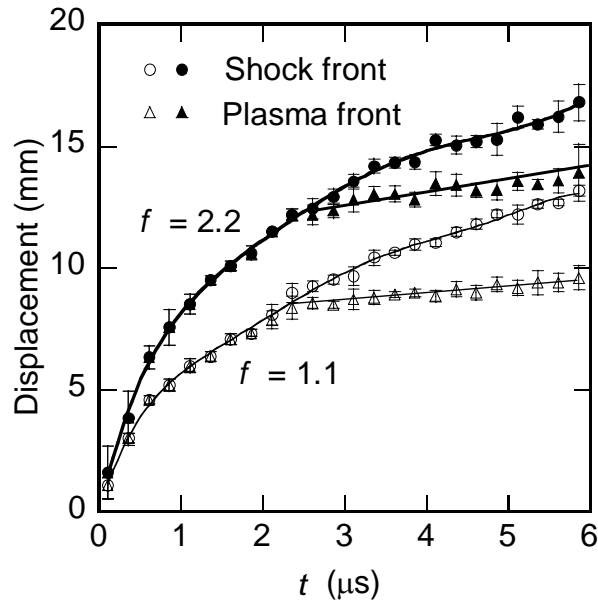


Figure 1.10: Displacements of the shock front and plasma front in the case of $E_i = 10$ J

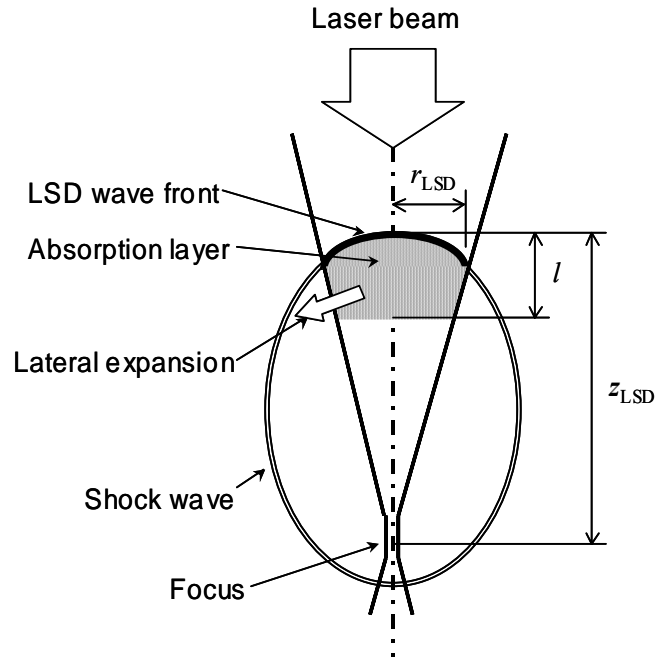


Figure 1.11: Schematic of LSD wave

Table 1.4: LSD threshold using different values of E_i and f .

E_i (J)	f	Threshold (MW/cm ²)
4	1.1	6.5 \pm 0.1
	2.2	7.4 \pm 0.1
10	1.1	2.6 \pm 0.4
	2.2	3.7 \pm 0.4
		1 – 10

1.4 Objective

- Using interferometry, the electron density profile in the laser absorption layer is measured in detail to characterize the laser absorption layer in the laser absorption regime after the LSD termination.

Chapter2

Measurement Method of electron Density

In order to measure the electron density profile in a plasma, various measurement methods have been developed. The methods are broadly classified into Intrusive method and nonintrusive method. By comparing with the characteristics of these measurement methods, interferometry is found to be the first candidate of the powerful methods for obtaining the 2-dimensional electron density profile in the laser absorption regime, which has very small length and propagates with very high velocity.

2.1 Intrusive Method

Langmuir probe method is one of the popular method among intrusive methods. Langmuir probe method give information on the local plasma parameters, such as plasma density, plasma potential and partly on the electron temperature. From the experiment point of view a Langmuir probe is very simple. However, LSD wave propagates along the laser light channel in the opposite direction to beam incidence, so the probe continue to be irradiated by the high power laser beam and is capable to be ablated. In addition, as common in the intrusive method, the probe gives the plasma crucial fluctuation to a plasma. Therefore, the Langmuir probe method is considered not to be applicable to measure the electron density in the laser absorption regime.

2.2 Nonintrusive Method

Emission spectroscopy method, Thomson Scattering method and Interferometry method are popular method among nonintrusive methods. Emission spectroscopy and Thomson Scattering give directly the information on the local plasma parameters, such as plasma density and the electron temperature. On the other hand, interferometry method gives only the information on the 2-dimensional distribution of only the electron and neutral particle density. However, Interferometry method has some merits in observing the electron density profile in the laser absorption regime, which has the very small scale and travels with the supersonic velocity.

2.2.1 Emission Spectroscopy Method

Emission spectroscopy method gives information on the various local plasma parameters, such as the electron density, the electron temperature and the constitute species density. Typical measurable electron density by this method is the order of $10^{21} \sim 10^{26} [\text{m}^{-3}]$.^{3 9 4 0} Considering that the electron density in the laser absorption regime would be near the critical density, which is estimated about $9.95 \times 10^{24} [\text{m}^{-3}]$ in the case of CO_2 laser [$\lambda=10.6\mu\text{s}$], the emission spectroscopy method could be applicable. However, emission spectroscopy method would have four problems in measuring the electron density in the laser absorption regime.

First, the laser absorption regime radiates high bremsstrahlung, which might be comparable to the

atomic or the molecular emission, so the analysis might be difficult.

Second, the laser absorption regime has the very small scale and propagates with supersonic velocity, so the alignment of the optical system, such as a focusing lens, would be very difficult. In addition, obtaining the distribution of the electron density in the laser absorption regime is needed to measure the small phenomenon several times, so the strict reproducibility of the phenomenon is required.

Third, although the laser absorption regime is considered to be in the highly thermal nonequilibrium state, standard method of emission spectroscopy requires an assumption of local thermodynamic equilibrium (LTE), or at least partial local thermodynamics equilibrium (PLTE), where electrons are in thermodynamic equilibrium with the atomic excited states, in order to determine temperature.

Fourth, the laser absorption regime might be optically thick enough for the emission spectroscopy method not to be applied..

2.2.2 Thomson Scattering Method

Thomson scattering method gives information on the various local plasma parameters, such as the electron density, the electron temperature even in the case of the incoherent scattering. In addition, the ion density and the ion temperature is also obtained in the case of the collective scattering.^{4 1} The electron temperature is obtained by measuring the spectral width, and the electron density is obtained by measuring the spectral intensity of the scattered light. Typical measurable electron density by this method is the order of $10^{17} \sim 10^{27} [\text{m}^{-3}]$.^{4 2} To obtain only the electron density and the electron temperature, incoherent scattering is desirable because of the easiness of analysis. Whether the scattering process is incoherent scattering or collective scattering depends on the electron temperature, the wavelength of the incident laser and the angle of the scattering light to be observed. Considering that the electron density in the laser absorption regime would be near the critical density, which is estimated about $9.95 \times 10^{24} [\text{m}^{-3}]$ in the case of CO_2 laser [$\lambda=10.6\mu\text{s}$], and the electron temperature is several or several dozen electronvolts, Thomson scattering method could be applicable by using the visible light laser such as excimer laser [$\lambda=248\text{nm}$] or Nd:Yag ($\lambda=532\text{nm}$) pulse laser, or ruby laser [$\lambda=694\text{nm}$]. In addition, Thomson scattering method is not required assumptions of LTE or PLTE differently from the emission spectroscopy. Therefore, Thomson scattering method is more powerful application than the emission spectroscopy method.

However, Thomson Scattering method has some problems in measuring the electron density in the laser absorption regime.

First, the laser absorption regime radiates high bremsstrahlung, which might be comparable to the scattering light, so the analysis might be difficult. However, differently from the emission spectroscopy method, this problem could be solved when the incident laser intensity increase.

Second, the strict reproducibility of the phenomenon is required as describing in the previous section. This is the main problem in measuring the electron density distribution in the laser absorption regime by using Thomson Scattering method.

2.2.3 Interferometry Method

Interferometry method gives information on the electron density and the neutral particle density. The indicator of the typical measurable electron density by this method is represented as the multiplication the electron density n_e and the scale length of the plasma l as shown in Table 2.1.^{4 3}

Considering that the electron density in the laser absorption regime would be near the critical density, which is estimated about $9.95 \times 10^{24} \text{ [m}^{-3}\text{]}$ in the case of CO₂ laser [$\lambda=10.6\mu\text{s}$], the interferometry method could be applicable.

However, interferometry method has some problems in measuring the electron density in the laser absorption regime. The laser absorption regime has a high electron density and high density gradient. When the electron density approaches to the fraction of a percent of the critical density for the probe beam, opacity effects can significantly limit this diagnostics. In addition, the change of the interferometer contrast due to probe beam reflection in the laser absorption regime with density gradients reduces the fidelity of interferometry measurement.

The other problems is that the standard analytical method of interferometry requires an assumption of single ionization. However, this assumption consist in the laser absorption regime because the ionization is restricted for the electron density not to over the critical density, $9.95 \times 10^{24} \text{ [m}^{-3}\text{]}$.

On the other hand, Interferometry method has a crucial advantage compared with Thomson Scattering method or emission spectroscopy method. The crucial advantage is that the interferometry method does not require the strict reproducibility in comparison with the other methods because the information on the electron density distribution is obtained by just one measurement. In addition, the measuring position is obvious because the whole phenomenon is pictured. The other advantage is the easiness of the alignment in the interferometry method compared with the alignment in Thomson Scattering method or emission spectroscopy method because the expanded probe beam is used.

As a result, interferometry method is found to be the first candidate of the powerful method for obtaining the 2-dimentional electron density profile in the laser absorption regime, which has very small length and propagates with very high velocity.

The characteristics of the three methods are summarized in Table 2.2.

Table 2.1: Comparison of $n_e l$ needed for the one fringe shift in using various type of the laser

	wavelength	$n_e l [\text{m}^{-2}]$
Excimer laser	248nm	9.0×10^{21}
Nd:Yag laser	532nm	4.2×10^{21}
Glass laser	1.06 μm	2.1×10^{21}
CO ₂ laser	10.6 μm	2.1×10^{20}

Table 2.2: Comparison of the popular methods for measuring electron density, emission spectroscopy method, Thomson scattering method and interferometry method.

	Emission Spectroscopy	Thomson scattering	Interferometry
Alignment	Difficult	Very difficult	Easy
Reproducibility	Strict	Strict	Non-strict
Assumption	LTE or PLTE	-----	Single ionization
Typical electron density	$10^{21} \sim 10^{26} [\text{m}^{-3}]$	$10^{17} \sim 10^{27} [\text{m}^{-3}]$	Table 3.2
Physical properties	Electron temperature Electron density Constitute species density	Electron temperature Electron density Ion density Ion temperature	Electron density Neutral particle density

Chapter3

Theory of Mach Zehnder Interferometry

In this chapter, the theory of Mach-Zehnder Interferometry, which is applied in this study, is presented. In addition to describe the principle of the Mach-Zehnder Interferometry, the numerical Abel inversion, which was introduced in the analysis of the fringe discontinuity produced by the strong shock front, is described. At the end, the data processing to derive the electron density profile from the fringe shifts is described.

Principle of Mach Zehnder Interferometry

In this section, the principle of Mach-Zehnder Interferometry is presented. Similarly to the other type of interferometry, for example Michelson interferometry, Mach-Zehnder Interferometry applies the coherency of a light to determine the refractive index of a measured objective, which is integrated by the line of sight. When the measured objective has an axisymmetric structure, the radial refractive index distribution of the measured objective can be also determined. Using this radial refractive index, the electron density profile of the plasma are derived.

Coherency

Coherency plays an important role in modern physics. It is very hard to find a single domain of physics where this concept is not applied.

In a general sense, a coherent process is defined as follows:

It is characterized by the existence of some well-defined deterministic phase relationship, or in other words, some phase is not subject to the random noise.

The coherent effect plays an important role in the appearance of the interference pattern, as known. The effect of coherency to the fringe is described in the section 3.1.4 in detail.

System of Mach Zehnder Interferometry

The system of the Mach-Zehnder interferometry consists of two half mirrors and two plane mirrors as shown in Fig.3.1. The light emitted from the light source is separated into two light by one half mirror, which are called a reference light and a probe light. The probe light propagates in the test section and is combined with the reference beam by the other half mirror. When these all optical components are aligned appropriately and fixed rigidly, a fringe pattern is obtained. The principle of the fringe generation is described in section 3.1.4, in detail. To get the best contrast fringe pattern, the half mirrors dividing the light intensity equally must be used and the lengths of the probe and reference channel must be equal.

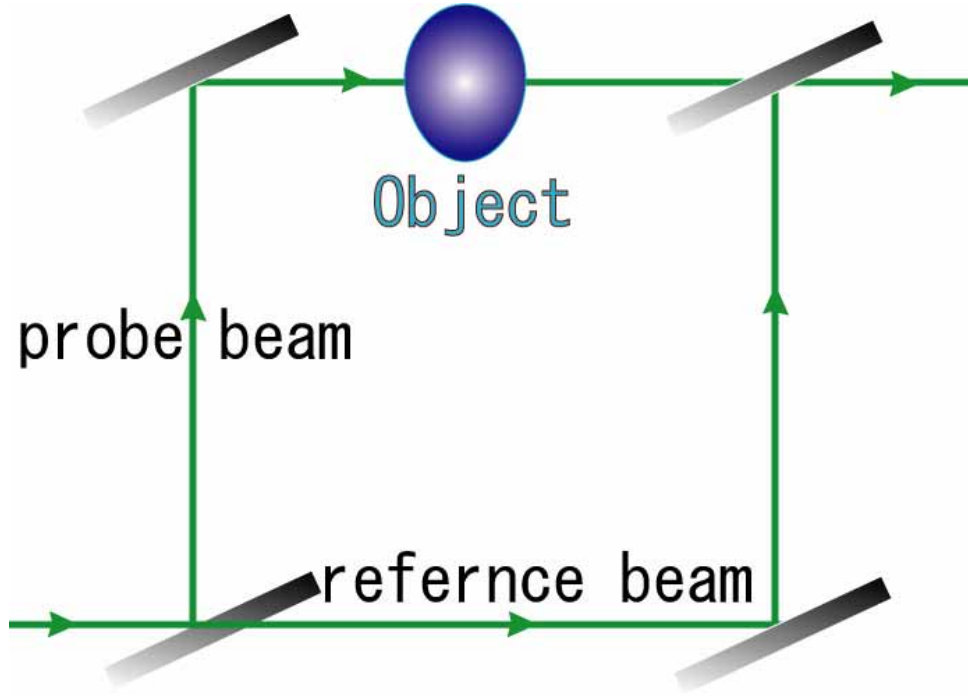


Figure 3.1: Schematic of Mach Zehnder Interferometry

Refractive Index

A refractive index is defined as the ratio of the phase speed of the light in a given medium and in a vacuum. In this study, this medium corresponds to a laser-induced plasma, which consists of electrons, ions and neutral particles, and a blast wave which consists of neutral particles.

In general, the refractive index of the medium μ , which consists of many species, is approximately expressed as follows

$$\mu - 1 = \sum K_j n_j \quad (3.1)$$

where K_j and n_j are the relative refractive index of species j and the number density of species j , respectively. As mentioned above, in this study, the medium consists of three species, an electron, an ion, a neutral particle.

The relative refractive indexes of an ion and a neutral particle are approximately constant, $K_i = 7.4 \times 10^{-30} [m^3]$, $K_n = 1.1 \times 10^{-29} [m^3]$.

On the other hand, the relative refractive index of an electron is not constant and its value is estimated from the dispersion relation of the electromagnetic wave propagating in a plasma under the assumption of no magnetic field. The dispersion relation is as follows^{4 4}

$$\omega^2 = \omega_{pe}^2 + k^2 c^2 \quad (3.2)$$

$$\omega_{pe} = \sqrt{\frac{n_e e^2}{m_e \epsilon_0}} \quad (3.3)$$

where ω , k is the angular frequency and the wavenumber of the electromagnetic wave in a plasma, respectively, and ω_{pe} is the plasma frequency. c , ϵ are the light velocity and the permittivity of free space, and n_e , m_e , e are the electron number density of a plasma, the electron mass and electron charge, respectively. The refractive index of an electron to the electromagnetic wave, which angular frequency is ω , is

$$u_e = kc / \omega \quad (3.4)$$

Using Eqs. (3.2) and (3.4), the following equation are derived.

$$\mu_e = \left(1 - \left(\frac{\omega_{pe}}{\omega} \right)^2 \right)^{1/2} \quad (3.5)$$

Under the additional assumption $\omega \gg \omega_{pe}$, Eq.(3.5) is

$$\mu_e - 1 = -\frac{\omega_{pe}^2}{2\omega^2} \quad (3.6)$$

From Eq. (3.1), the relative refractive index is expressed as follows

$$K_e = -\frac{e^2}{8\pi^2 c^2 m_e \epsilon_0} \lambda^2 \quad (3.7)$$

where λ is the wavelength of the electromagnetic wave. From Eq.(3.7), $-K_e$ is found to proportional to the square of the wavelength.

Fundamental Relationships of Fringe and its shifts

Although a number of interference phenomena are known that can be interpreted consistently only by using the theory of quantum optics, it would be very complex and beyond necessity in this study. Therefore, the classical theory of the electromagnetic wave is applied to derive the fundamental relationship about the interference phenomenon.

Electromagnetic wave notation of classical theory

Using the notations of the classical electromagnetic theory of light, a monochromatic wave is represented as follows

$$\mathbf{E}(x, y, z, t) = \mathbf{a}(x, y, z) \cdot \exp(-i(\omega t + \phi(x, y, z))) \quad (3.8)$$

where $\mathbf{E}(x, y, z, t)$ is the complex electric field intensity vector, $\mathbf{a}(x, y, z)$ is the amplitude vector at the

give point of space, ω is the angular frequency of the electromagnetic wave. The quantity $\varphi(x,y,z)$ is the initial phase of the oscillations at the given point of space.

In the assumptions of the plane electromagnetic wave, $\varphi(x,y,z)$ can be determined simply and represented as follows

$$\varphi(x, y, z) = -\mathbf{k} \cdot \mathbf{r} + \delta \quad (3.9)$$

where the \mathbf{k} is the wave number of the electromagnetic wave, \mathbf{r} is the position vector, and δ is the initial phase of the oscillation at the zero point.

The complex quantity $E(x,y,z,t)$ can be represented in the form of two multipliers, one of which depends only on the time, and the other only on the coordinates of the given point,

$$\mathbf{E}(x, y, z, t) = \mathbf{A}(x, y, z) \exp(-i\omega t) \quad (3.10)$$

where $A(x,y,z)$ is called the complex vector of the amplitude and represented as follows

$$\mathbf{A}(x, y, z) = \mathbf{a}(x, y, z) \exp(-i\varphi(x, y, z)) \quad (3.11)$$

and the magnitude of this complex vector of the amplitude $A(x,y,z)$ is called complex amplitude A .

Superposition of Wave Field

If several light simultaneously propagate in the space, in accordance with the wave superposition, the resultant field is represented as follows.

$$\mathbf{E}(x, y, z, t) = \sum_i \mathbf{E}_i(x, y, z, t) \quad (3.12)$$

If all waves have the identical frequency, using the complex form of writing, Eq.(3.12) is transformed into the follows equation.

$$\mathbf{E}(x, y, z, t) = \mathbf{A} \exp(-i\omega t) = \exp(-i\omega t) \sum_i \mathbf{A}_i \quad (3.13)$$

where A is the complex amplitude of the composite wave. Hence,

$$\mathbf{A} = \sum_i \mathbf{A}_i \quad (3.14)$$

Thus, instead of the summation of the electric field intensity vector, the complex amplitude vector are summed by omitting the time factor $\exp(-i\omega t)$. This simplification is not possible in the case of the summation of the waves with the different frequencies.

In addition, with the assumption that the electric intensity vectors being added are parallel, the summation of the complex amplitude vectors can transform the summation of the complex amplitudes as follows.

$$A = \sum_i A_i \quad (3.15)$$

Interference of two Plane Monochromatic Waves of Identical Frequency

The superposition of the two electromagnetic waves, which has the wavenumber k_1 and k_2 ,

respectively, are considered here. In accordance with Eq.(3.11), the notation of the complex amplitude vector is as follows.

$$\mathbf{A}_1 = \mathbf{a}_1(r) \exp(-i(\delta_1 - \mathbf{r} \cdot \mathbf{k}_1)) \quad (3.15)$$

$$\mathbf{A}_2 = \mathbf{a}_2(r) \exp(-i(\delta_2 - \mathbf{r} \cdot \mathbf{k}_2)) \quad (3.16)$$

In the assumption that the electric field intensity vectors for both waves are perpendicular to the plane wave surface, the complex amplitude of the resultant wave, in accordance with Eq.(3.15), is as follows.

$$A(\mathbf{r}) = A_1(\mathbf{r}) + A_2(\mathbf{r}) = a_1 \exp(-i(\delta_1 - \mathbf{r} \cdot \mathbf{k}_1)) + a_2 \exp(-i(\delta_2 - \mathbf{r} \cdot \mathbf{k}_2)) \quad (3.17)$$

For homogeneous plane waves propagating in the nonabsorbing medium, their amplitude is independent of its position vector \mathbf{r} .

The resultant intensity is as follows

$$\begin{aligned} I(\mathbf{r}) &= A(\mathbf{r}) \cdot A^*(\mathbf{r}) = a_1^2 + a_2^2 + a_1 a_2 \exp(-i((\delta_1 - \delta_2) - \mathbf{r} \cdot (\mathbf{k}_1 - \mathbf{k}_2))) \\ &\quad + a_1 a_2 \exp(i((\delta_1 - \delta_2) - \mathbf{r} \cdot (\mathbf{k}_1 - \mathbf{k}_2))) \\ &= a_1^2 + a_2^2 + 2a_1 a_2 \cos(\mathbf{r} \cdot (\mathbf{k}_1 - \mathbf{k}_2) - (\delta_1 - \delta_2)) \end{aligned} \quad (3.18)$$

Form Eq.(3.18), it follows that the total intensity is changed periodically reaching maxima (antinodes) at points for which

$$\mathbf{r} \cdot (\mathbf{k}_1 - \mathbf{k}_2) - (\delta_1 - \delta_2) = 2m\pi \quad (3.19)$$

where m is an integer.

The condition

$$\mathbf{r} \cdot (\mathbf{k}_1 - \mathbf{k}_2) - (\delta_1 - \delta_2) = (2m + 1)\pi \quad (3.20)$$

corresponds to minima of the intensity (nodes).

If the difference $(\delta_1 - \delta_2)$ is constant in time, then the position of the lines of the nodes and antinodes determined by Eqs.(3.19) and (3.20) remains unchanged in space, i.e. a stable interference pattern is observed.

For the usual light source emits the light, which changes the phase chaotically with time, the quantity $(\delta_1 - \delta_2)$ changes chaotically; this leads to the blurring interference pattern. The average value of $\cos(\mathbf{r} \cdot (\mathbf{k}_1 - \mathbf{k}_2) - (\delta_1 - \delta_2))$ during the time of measurement, which is sufficiently great, is equal to zero, and Eq.(3.18) give the simple addition of the intensities of the two

$$I(r) = a_1^2 + a_2^2 = I_1 + I_2 \quad (3.21)$$

It is evident that if the phases of the light waves emitted by independent source change sufficiently slowly, which occur in highly stable lasers, we can also observe an interference pattern from two independent sources, especially when the intensity is measured fast enough.

When conventional (non-laser) sources of light are used to obtain an interference pattern, the phases δ_1, δ_2 is usually dependent each other. This is assured if the interfering waves are parts of the same primarily wave, as seen Young's experiment. The primary wave is divided similarly in number of other interference devices by wave front division or by the amplitude division(Michelson

Mach-Zehnder interferometry). In such cases, the phases δ_1, δ_2 do not change chaotically with time, which mean that the two light has coherency, their difference $\delta_1 - \delta_2$ remains constant, which produce the stable interference pattern.

Spatial frequency of the fringe

In the assumption of $(\delta_1 - \delta_2) = 0$, which is valid for the Mach-Zehnder Interferometry, the condition for the formation of the antinodes,

$$\mathbf{r}(\mathbf{k}_1 - \mathbf{k}_2) = 2m\pi \quad (3.22)$$

Equation (3.22) represents planes perpendicular to the vector $\mathbf{\kappa} = \mathbf{k}_1 - \mathbf{k}_2$.

Because $|\mathbf{k}_1| = |\mathbf{k}_2| = 2\pi/\lambda$, the vector $\mathbf{\kappa}$ is the base of the isosceles triangle whose sides are the vectors \mathbf{k}_1 and \mathbf{k}_2 . The distance from these planes to the origin of coordinates is

$$a_m = \frac{2m\pi}{|\mathbf{\kappa}|} \quad (3.23)$$

The distance between adjacent planes d , labeled m and $m+1$, is

$$d = a_{m+1} - a_m = \frac{2\pi}{|\mathbf{\kappa}|} \quad (3.24)$$

It follows

$$|\mathbf{\kappa}| = 2|\mathbf{k}_1| \sin \frac{\alpha}{2} = \frac{4\pi}{\lambda} \sin \frac{\alpha}{2} \quad (3.25)$$

Therefore

$$d = \frac{\lambda}{2 \sin \left(\frac{\alpha}{2} \right)} \quad (3.26)$$

The spatial frequency of this fringe pattern is

$$\nu = \frac{1}{d} = \frac{2 \sin \left(\frac{\alpha}{2} \right)}{\lambda} \quad (3.27)$$

Infinite Fringe and Finite Fringe

The fringe pattern, which spatial frequency is equal to zero in the case of $\alpha=0$ in Eq.(3.26), is called infinite fringe pattern. $\alpha=0$ means that the plane wave surfaces overlap completely. Applying such an infinite-fringe interferometry for the two dimensional flows, direct comparison between the computational fluid dynamic (CFD) simulation and experiment is reasonably straight-forward, because fringes in infinite-fringe interferograms correspond to density contours.

On the other hand, the fringe pattern, which spatial frequency is non-zero in the case of $\alpha \neq 0$ in Eq.(3.26), is called finite fringe pattern. $\alpha \neq 0$ means the plane wave surfaces intersect at the angle α . Contrary to the infinite-fringe interferometry, the finite-fringe interferometry can be applied not only

for the two dimensional flows but also for the axisymmetric or three dimensional flows. In this study, this finite-fringe interferometry were used because the measured object is an axisymmetric flow.

Fringe shift by the measured object

When the measured object exists in the channel of the one of the waves divided from the primary wave, the phase delay δ_{object} is occurred because of its refractive index and the plane wave surface is distorted. The complex amplitude of this wave is represented as follows

$$\mathbf{A}_1 = \mathbf{a}_1(r) \exp(-i(\delta_1 - \mathbf{r} \cdot \mathbf{k}_1 - \delta_{object})) \quad (3.28)$$

and from the superposition of two wave, the complex amplitude of the resultant wave is

$$A(\mathbf{r}) = A_1(\mathbf{r}) + A_2(\mathbf{r}) = a_1 \exp(-i(\delta_1 - \mathbf{r} \cdot \mathbf{k}_1 - \delta_{object})) + a_2 \exp(-i(\delta_2 - \mathbf{r} \cdot \mathbf{k}_2)) \quad (3.29)$$

Similarly to Eq.(3.18), the resultant intensity is as follows

$$I(\mathbf{r}) = A(\mathbf{r}) \cdot A^*(\mathbf{r}) = a_1^2 + a_2^2 + 2a_1a_2 \cos(\mathbf{r} \cdot (\mathbf{k}_1 - \mathbf{k}_2) - \delta_{object} - (\delta_1 - \delta_2)) \quad (3.30)$$

In this case, the condition of reaching maxima and minima is represented as follows, respectively

$$\mathbf{r} \cdot (\mathbf{k}_1 - \mathbf{k}_2) - \delta_{object} - (\delta_1 - \delta_2) = 2m\pi \quad (3.31)$$

$$\mathbf{r} \cdot (\mathbf{k}_1 - \mathbf{k}_2) - \delta_{object} - (\delta_1 - \delta_2) = (2m + 1)\pi \quad (3.32)$$

From Eqs.(3.21) and (3.32), the positions which are antinodes and nodes in the absence of the measured objective is no longer antinodes and nodes position in the presence of the measured object. This is the reason for generating the fringe shifts.

Contrast of Interference Pattern

The contrast or visibility of a periodic structure p is defined as the quantity

$$p = \frac{I_{max} - I_{min}}{I_{max} + I_{min}} \quad (3.34)$$

where I_{max} and I_{min} are the intensities of the light wave in the antinodes and nodes of the fringe pattern, which are represented as follows

$$I_{max} = a_1^2 + a_2^2 + 2a_1a_2 \quad (3.35)$$

$$I_{min} = a_1^2 + a_2^2 - 2a_1a_2 \quad (3.36)$$

Therefore,

$$p = \frac{2a_1a_2}{a_1^2 + a_2^2} = \frac{2\sqrt{I_1I_2}}{I_1 + I_2} = \frac{2\sqrt{\alpha}}{\alpha + 1} \quad (3.37)$$

Here $\alpha = a_1^2 / a_2^2 = I_1 / I_2$ is the ratio of the intensities of the interfering waves. The contrast of an interference pattern is maximum and equals unity when $\alpha = 1$, i.e., when the amplitudes of the waves being added are equal.

Abel Deconvolution

An interference pattern shift indicates the projected phase of the measured object on the camera (or screen) along the channel of the probe beam, in other words, the integrated phase of the measured object by the line of sight. In addition to the interferometry, projection data is also obtained in some experiments, for example, spectroscopy and holography. These obtained projection data can reconstruct the local value by using the Abel deconvolution in the case of an axisymmetric object as shown in **Fig.3.2**. The object is symmetrical relative to the y axis. The beam passes through the object in the direction z. In this case, the measured value $Q(x)$, as shown in Fig.3.3, which is obtained by integrating the radial distribution $f(r)$ along the line of sight, is represented as follows

$$Q(x) = 2 \int_x^\infty \frac{rf(r)}{\sqrt{r^2 - x^2}} dr \quad (3.38)$$

Using the Abel deconvolution, the radial distribution is obtained as follows

$$f(r) = -\frac{1}{\pi} \int_r^\infty \frac{\left(\frac{dQ(x)}{dx} \right)}{\sqrt{x^2 - r^2}} dx \quad (3.39)$$

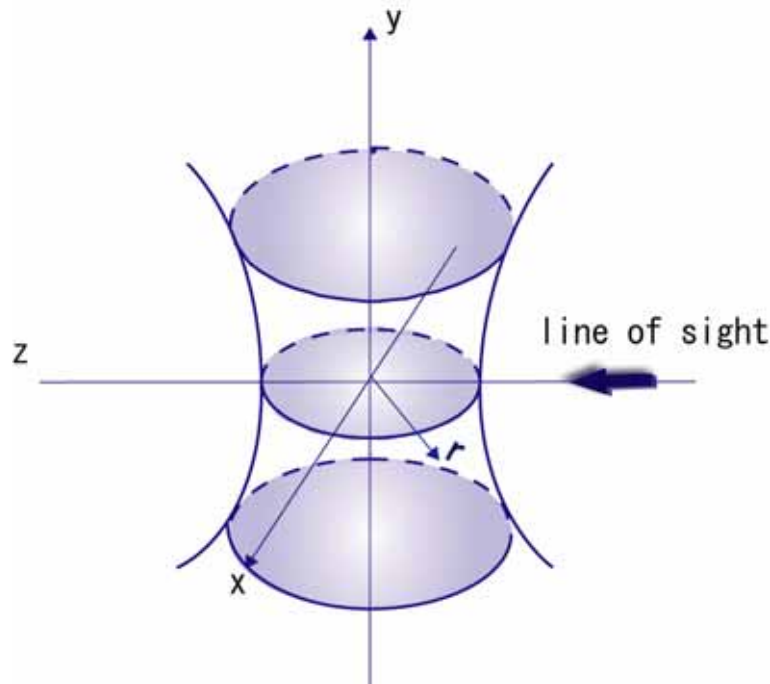


Figure 3.2: Schematic of an axisymmetric object

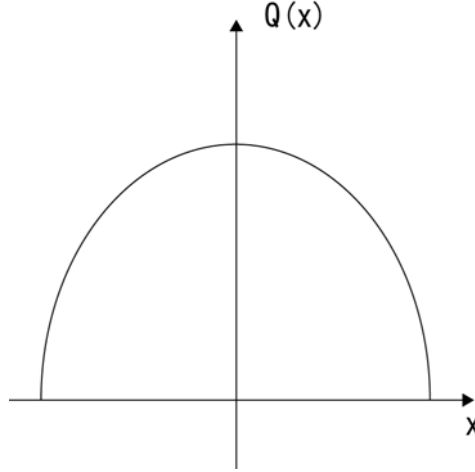


Figure 3.3 :Distribution $Q(x)$ obtained by integrating $f(r)$ by the line of sight

Way of Extracting Electron Density

In general, the projected phase on the camera ϕ is represented as follows

$$\phi = \frac{2\pi}{\lambda} \int (N_{ref}(z) - N_{flow}(z)) dz \quad (3.40)$$

where z is the direction of the channel of the probe laser beam, N is the refractive index, the subscripts, "ref" and "flow" is represented in the case without and with a flow in the test area, respectively, λ is the wavelength of the laser as light source.

For the axisymmetric object, the radial distribution of the refractive index obtained from the projected phase on the camera by using Abel deconvolution is as follows.^{4 5}

$$\Delta N(r) = N_{ref} - N_{flow} = \frac{-\lambda}{2\pi^2} \int_r^\infty \left(\frac{1}{\sqrt{x^2 - r^2}} \frac{d\phi}{dx} \right) dx \quad (3.41)$$

where $\Delta N(r)$ is the difference of the refractive index between the no-flow field and the flow field. N_{flow} is contributed not only to the neutral particles in blast wave but also to the electrons and the ions in the plasma. Considering these contributions, the refractive index is represented as follows^{4 6}

$$N_{ref}(r) = K_n n_0 \quad (3.42)$$

$$N_{flow}(r) = K_n n_n(r) + K_i n_i(r) + K_e n_e(r) \quad (3.43)$$

where K is a relative refractive index and n is a number density. The subscripts, n , i , e , represent a neutral particle, an ion, an electron, respectively. n_0 is the number density of the neutral particle in the atmospheric air.

Under the assumption of the singly ionized plasma, $n_e(r) = n_i(r)$, the electron density distribution is derived from Eqs.(3.41)-(3.43) as follows

$$n_e(r) = \frac{K_n(n_0 - n_n(r)) + \Delta N(r)}{K_e + K_i} \quad (3.44)$$

If the spectrum of the laser beam is the visible range as in this study, $K_e \gg K_i$ consists. In addition, $n_0 \gg n(r)$ would consist inside the plasma, which is the rarefied and high-ionized regime. Therefore, Eq.(3.44) is approximated as follows

$$n_e = \frac{\Delta N(r) + K_n n_0}{K_e} \quad (3.45)$$

Numerical Abel Deconvolution

In this section, the numerical Abel deconvolution used in this study is described. The program constructed for the numerical Abel deconvolution in this study was applied to test three basis test functions, a step function, a gauss function, and a polynomial function, for confirming the validity of this program. As the results, good agreements between the original and reconstructed functions are found. This agreements support the availability of this program for these test functions.

Reasons for Using Numerical Abel Deconvolution

The best performance of the Abel deconvolution would be appeared when the projected phase data can be fitted to a linear combination of the basis functions for which the Abel deconvolutions are known. But, in this study, the linear combination of the basis functions, which is well-suited to the discontinuous jump of the projected phase across the shock wave could not be found. Therefore, in this study, the regime around the discontinuity of the projected phase is needed to reconstructed by using the numerical Abel deconvolution method.

Computation of Abel Deconvolution

The numerical Abel deconvolution has been developed for a long time because the measured value is rarely well-fitted to the basis function for which Abel deconvolutions are known.^{4 7 4 8}

In calculating the Abel integral equation, Eq.(3.39) is not usually used because the integrand is diverged at $x=r$, which leads to make the algorithm very difficult. Therefore, this equation is transformed into the altered form to eliminate the singular point as follows

$$f(r) = -\frac{1}{\pi} \int_r^\infty \sqrt{x^2 - r^2} \frac{d}{dx} \left(\frac{1}{x} \frac{dQ(x)}{dx} \right) dx \quad (3.45)$$

In Eq.(3.45), the singular point is appeared only when both r and x is equal to zero, so, in comparison with Eq.(3.39), this equation is readily calculated.

Performance of Program

Numerical Abel deconvolution is introduced in order to calculate the Abel integral equation around

the regime, where the projected phase jumps discontinuously, so the step function, which has a discontinuous regime, was selected as the test function for this program at first.

The Abel deconvolution error is defined here that the deviation of the reconstructed function from the original function $Q_I(x)$. The reconstructed function is obtained by using the following equation

$$Q_1(x) = 2 \int_x^{\infty} \frac{rf_1(r)}{\sqrt{r^2 - x^2}} dr \quad (3.46)$$

where $f_1(r)$ is the radial distribution derived from $Q_I(x)$ by using Abel deconvolution. By using Eq.(3.46), the radial distribution quantity converts into the quantity integrated along the line of sight.

In this section, the three types of testing are described. They are classified by the way of dividing the discontinuous regime. In the test 1, the original step function $Q_I(x)$ is divided equally to have one interval in the discontinuous regime. In the test 2, the original step function $Q_I(x)$ is divided equally to have ten intervals in the discontinuous regime. At the end, in the test 3, the original step function $Q_I(x)$ is divided non-equally intervals, which is obtained by eliminating one point from the discontinuous regime in the test 2.

<Test1>

Figure 3.4 shows the original step function $Q_I(x)$ divided equally to have one interval in the discontinuous regime. Figure 3.5 shows the result of applying the Abel deconvolution to $Q_I(x)$. Figure 3.6 shows the original and reconstructed distribution and Fig.3.7. shows the Abel deconvolution error.

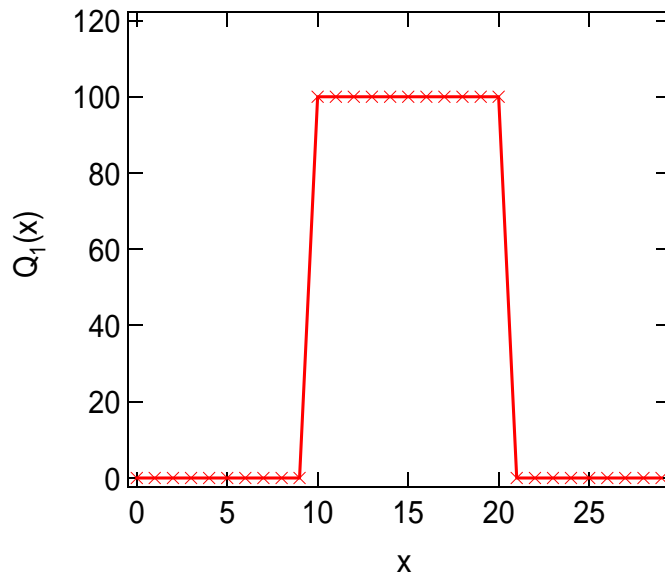


Figure 3.4: Original step function with no division in the discontinuously changing regime of $Q_I(x)$

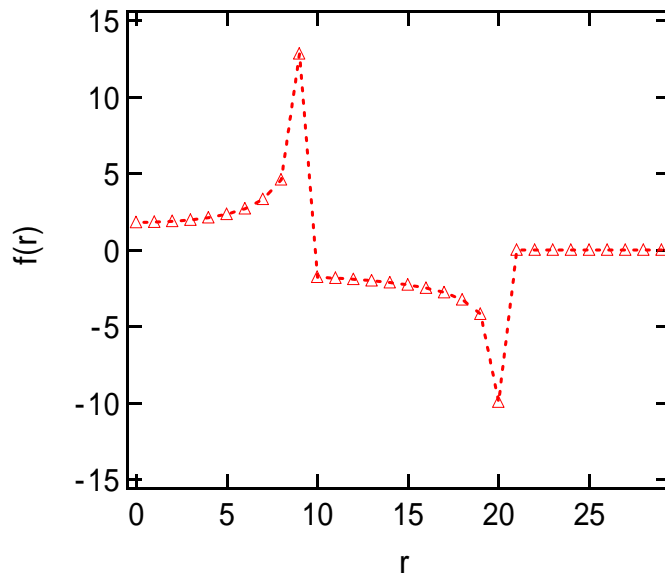


Figure 3.5: Radial distribution applying Abel deconvolution to the test function $Q_I(x)$

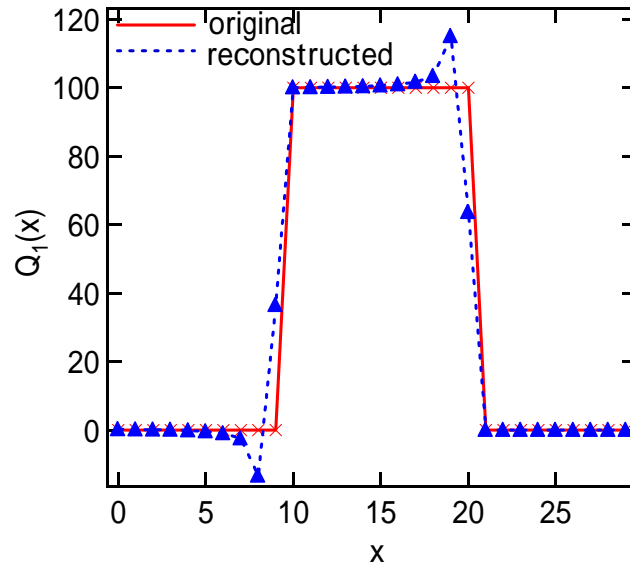


Figure 3.6:Original and reconstructed distributions

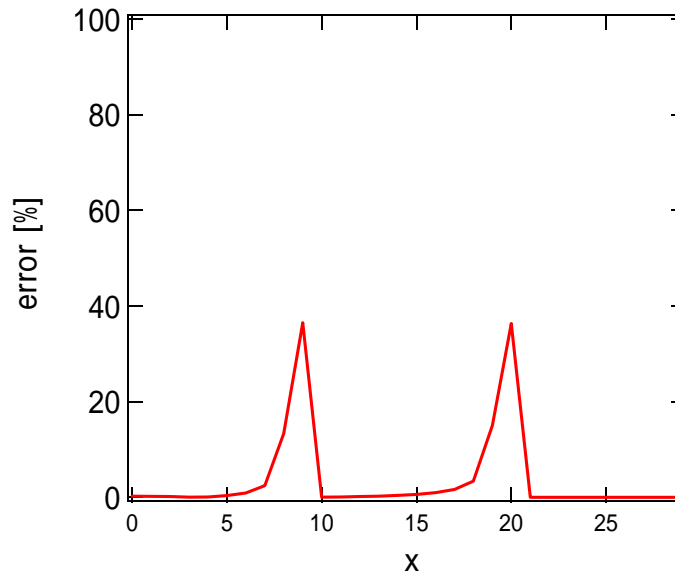


Figure 3.7:Error distribution between the original and reconstructed distribution

<Test2>

Figure 3.8 shows the original step function $Q_I(x)$ divided equally to have ten interval in the discontinuous regime. Figure 3.9 shows the result of applying the Abel deconvolution to $Q_I(x)$. Figure 3.10 shows the original and reconstructed distribution and figure 3.11 shows the Abel deconvolution error.

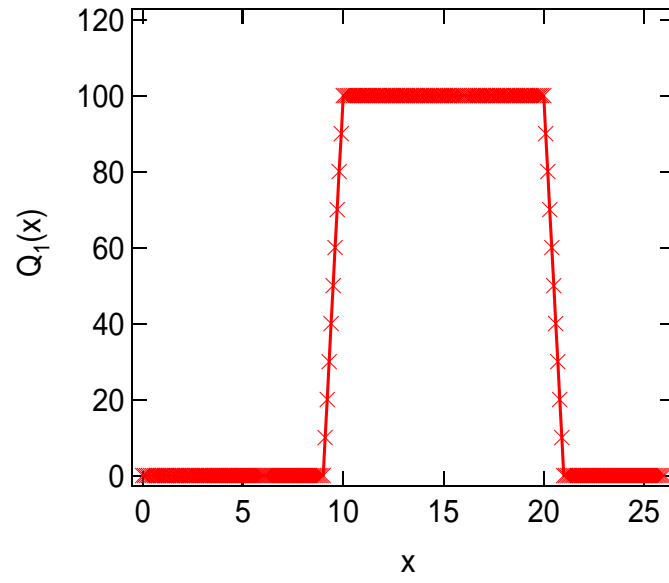


Figure 3.8: original step function with ten equally-spaced divisions in the discontinuously changing regime of $Q_I(x)$

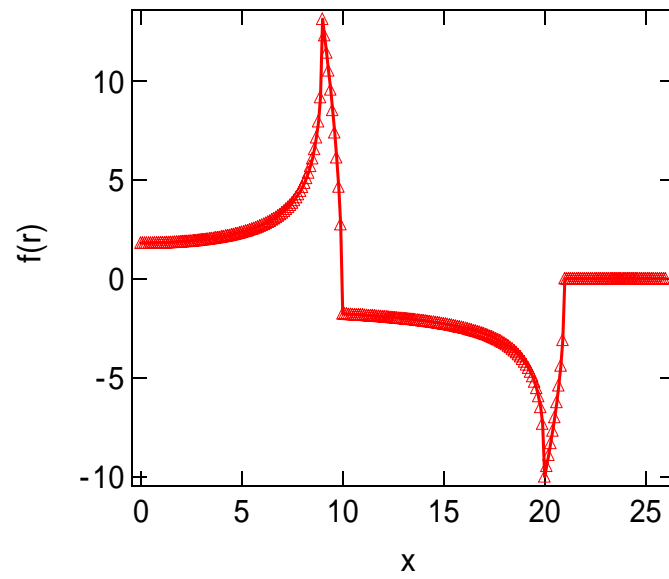


Figure 3.9: Radial distribution applying Abel deconvolution to the test function $Q_I(x)$

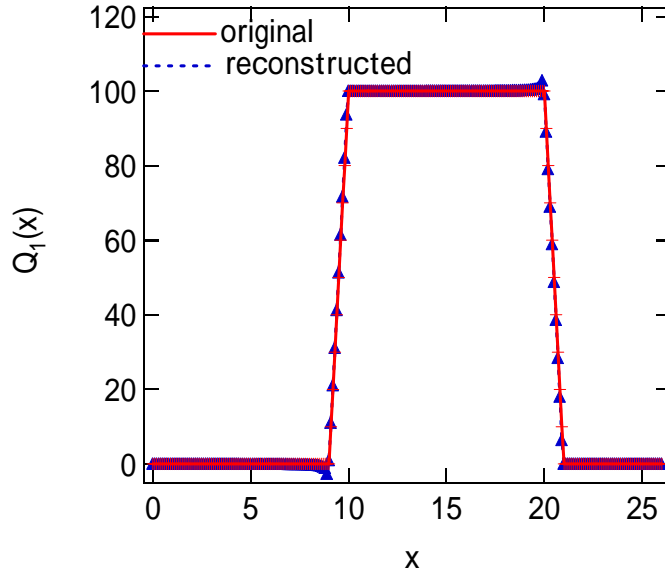


Figure 3.10:Original and reconstructed distributions

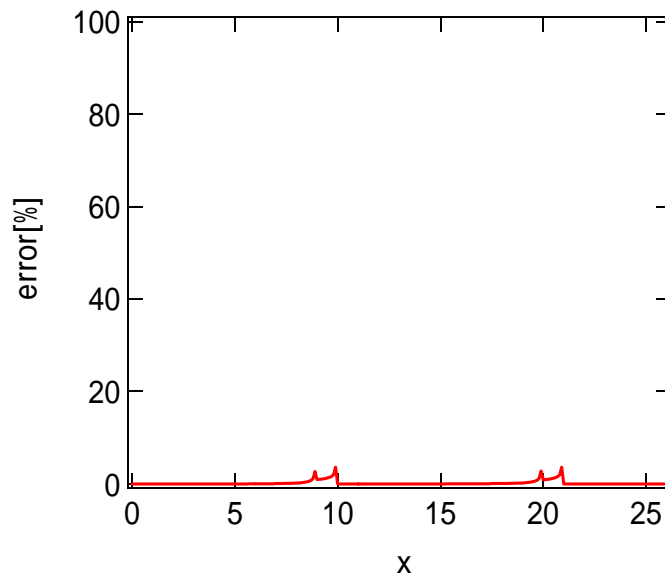


Figure 3.11:Error distribution between the original and reconstructed distribution

Figure 3.12 shows the original step function $Q_I(x)$ divided non-equally. The unequally-spaced discrete points are obtained by eliminating only the one point, $(x, Q(x)) = (20.8, 20)$, from the discrete point in the test 2. Figure 3.13 shows the result of applying the Abel deconvolution to $Q_I(x)$. Figure 3.14 shows the original and reconstructed distribution and figure 3.15 . shows the Abel

deconvolution error.

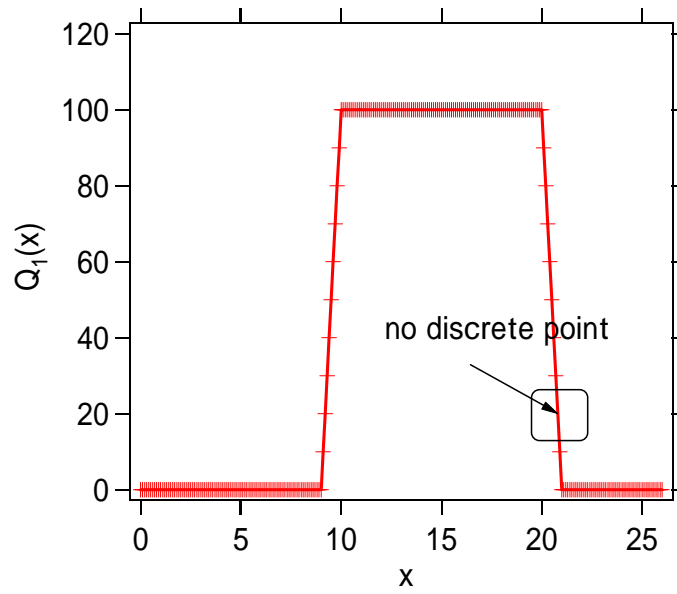


Figure 3.12:original step function with unequally-spaced 9 intervals in the discontinuous regime, which is obtained by eliminating one point from the discrete points in the test 2.

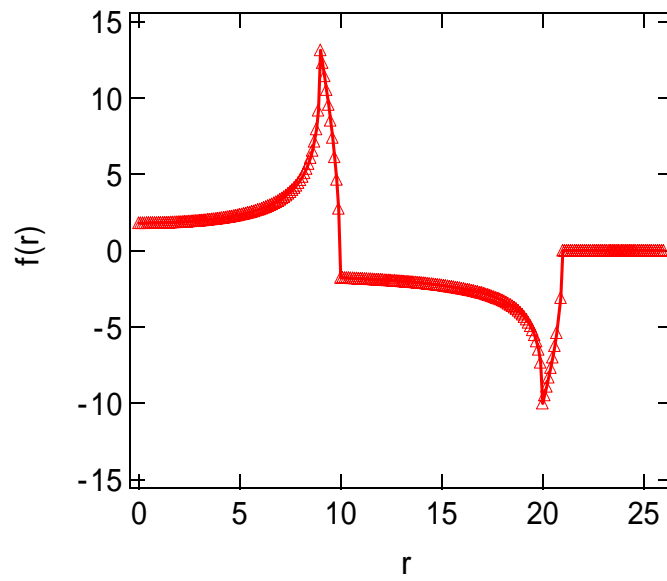


Figure 3.13:Radial distribution applying Abel deconvolution to the test function $Q_I(x)$

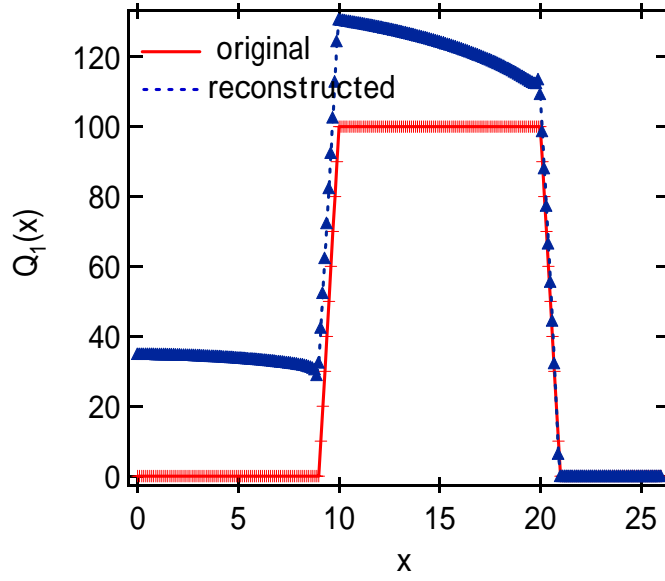


Figure 3.14:Original and reconstructed distributions

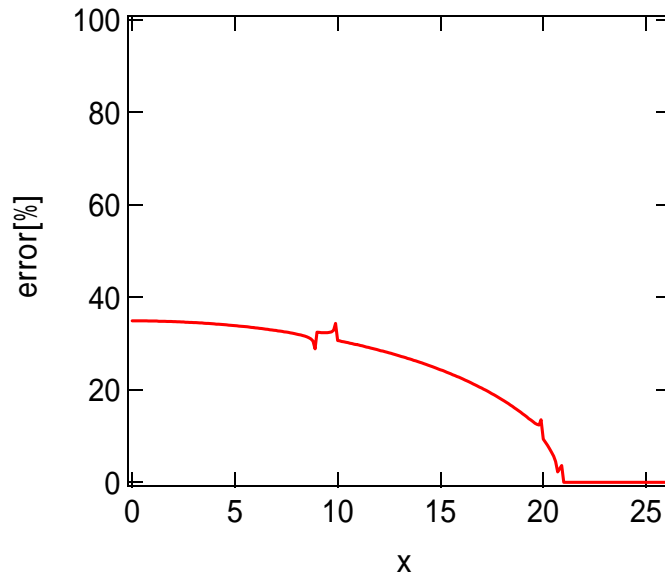


Figure 3.15:Error distribution between the original and reconstructed distribution

From these three tests, the best performance of this algorithm for the functions with discontinuous regime is found to be appeared when the function is divided into equally-spaced discrete points, which interval must be small enough to divide the discontinuous regime into several sections, all over the domain of the function. In addition, the interval is smaller, the performance of this algorithm is better.

3.2.4 Performance of Algorithm using Various Function as test Function

In this section, the algorithm is applied to the other test function $Q_2(x)$, which is the linear combination of three functions, a step function, a gauss function, a polynomial function, in order to confirm the applicability to various functions.

Figure 3.16 shows the original step function $Q_2(x)$ divided equally all over the domain to have ten interval in the discontinuous regime of the step function. Figure 3.17 shows the result of applying the Abel deconvolution to $Q_2(x)$. Figure 3.18 shows the original and reconstructed distribution and Fig.3.19 shows the Abel deconvolution error.

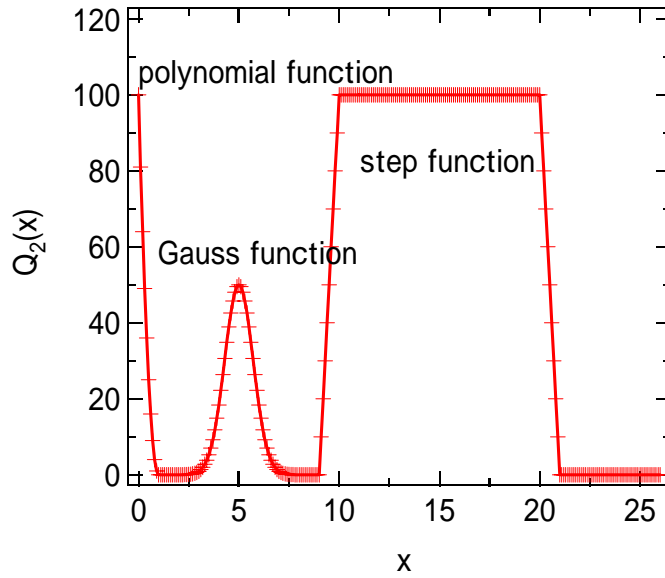


Figure 3.16:Original step function with ten equally-spaced divisions in the discontinuously changing regime of $Q_I(x)$

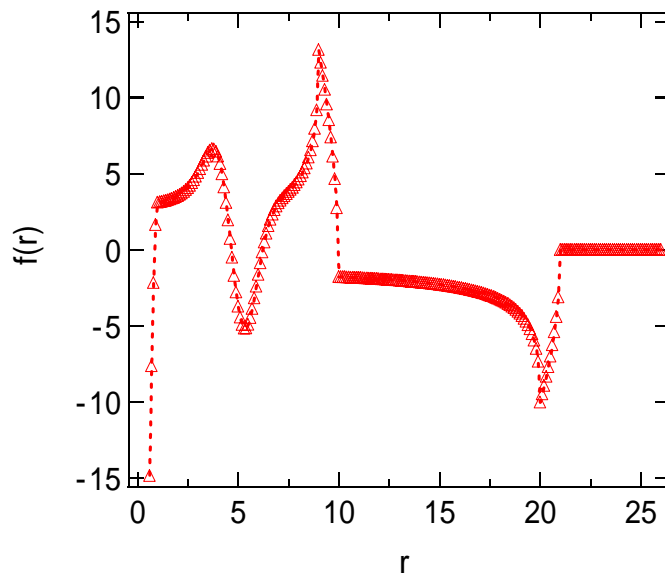


Figure 3.17:Radial distribution applying Abel deconvolution to the test function $Q_I(x)$

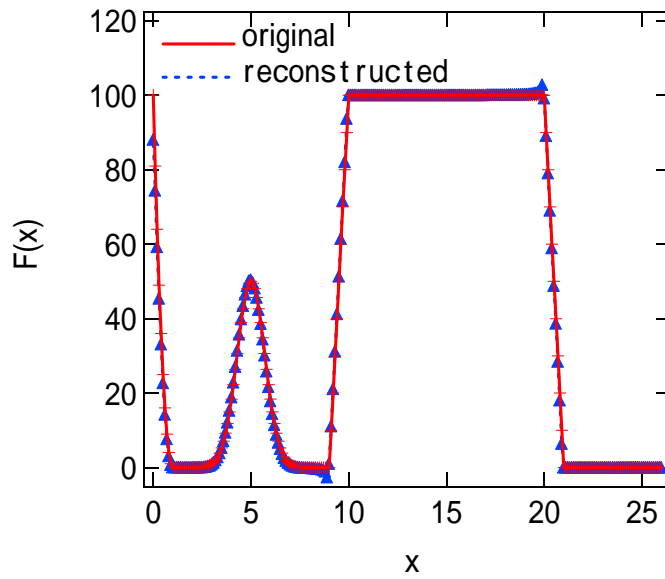


Figure 3.18:Original and reconstructed distributions

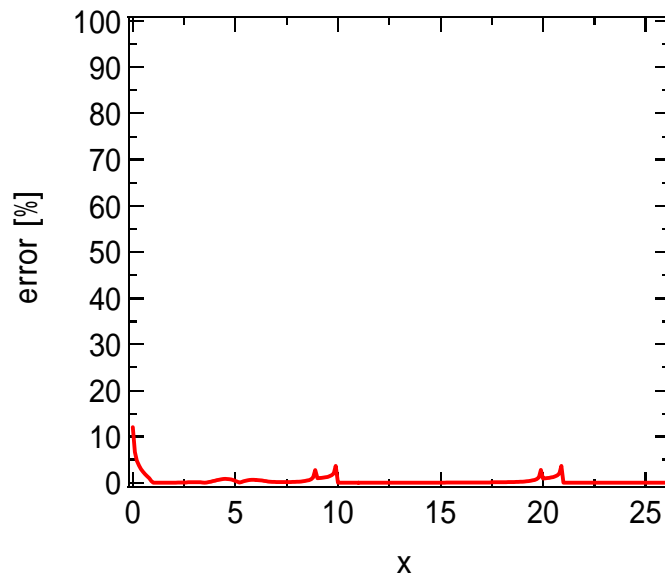


Figure 3.19:Error distribution between the original and reconstructed distribution

From this test, the algorithm is found to be applicable to the linear combination of the three functions, a step function, a gauss function, a polynomial function, in the case of admitting about 10% error around the zero point, where the integrand is diverged.

Data Processing

In this section, data processing, by which the electron density profile is derived from the fringe shift, is described. Numbers of fringe shifts evaluated from interferograms visually are fitted by a 9th polynomial as a function of a distance from an axis on a projecting plane except for near the discontinuous jump of the fringe across the shock front. The numbers of fringe shifts near a shock front could not be well-fitted by any basic function as mentioned above, so a linear interpolation was applied to this region.

Method to Count the Number of Fringe Shifts

The number of the fringe shift distribution on the projected plane is needed to obtain the projected phase distribution ϕ , which are used to derive the refractive index distribution as shown in eq(). In this study, instead of making the auto-tracking fringe system, the fringe number is virtually counted

Figure 3.20 shows the typical interference pattern obtained in this study.

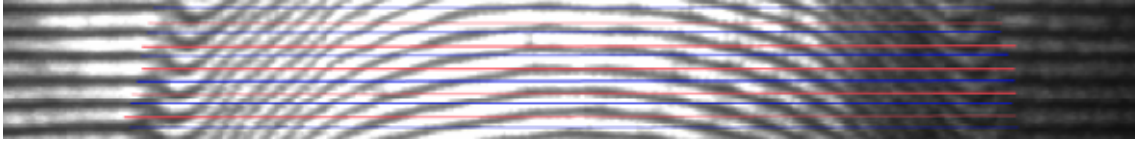


Figure 3.20: Typical interference pattern in our measurement.

Figure 3.21 shows the simple schematic of this fringe pattern, which contains the fringe jump across the shock front, and the way of counting the number of the fringe shifts from the obtained interference figure. Although the number of the fringe shifts is counted generally along the line as shown in Fig.3.20, which is called a tilt method,⁴⁻⁹ the fringe pattern can not be tracked obviously, for example, the fringe pattern behind the fringe jump as illustrated in Fig.3.21. Therefore, in such a region where the accurate tracking is impossible by using the tilt method, the method tracking the nearest fringe pattern from the line is applied in this study. This tracking method would be valid when the fringe pattern has the spatially high resolution compared to the scale length of the variation of the phenomenon.

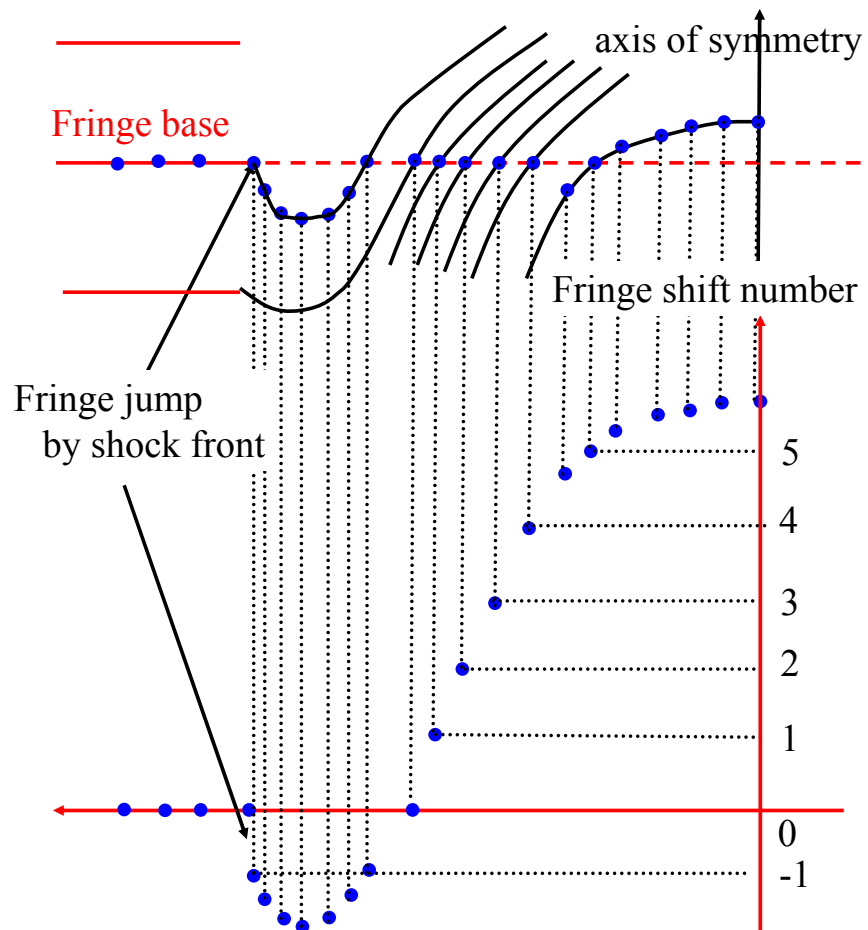


Figure 3.21: The way of counting the fringe shift number from obtained interference pattern

Polynomial Fitting and Numerical Abel Deconvolution of Phase Data

In order to decrease the errors in the Abel deconvolution, the plotted data as shown in Fig.(3.21) was fitted to the 9th order polynomials without the region around the discontinuous fringe shift as shown in Fig.3.22(a). Figure 3.22(a). also shows the reconstructed distribution from the combination of the fitting data and plotted data by using Abel deconvolution. Figure 3.22(b) shows the error distribution of the Abel deconvolution, maximum of which is 6% around the discontinuous regime due to mainly using plotted data. On the other hand, the error around 0 is found to be almost 0% in this fringe pattern.

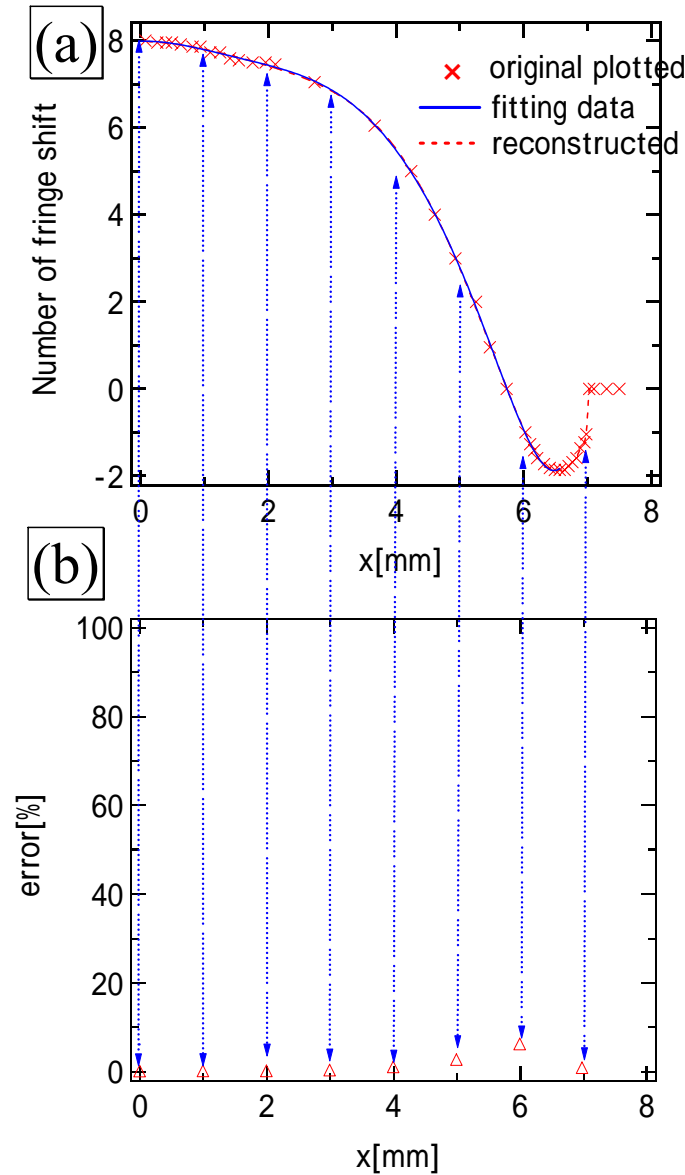


Figure 3.22 (a) Original distribution of the plotted data and the fitted data and reconstructed distribution (b) Error distribution of the Abel deconvolution

Chapter4

Measurement Apparatus and Results

In this chapter, the measurement apparatus, the results, in addition, its measurement conditions are shown. The electron density profile of the 10J- CO₂- pulse-laser-induced plasma with the focusing optics of #f=2.2 were obtained.

4.1 Experimental Apparatus

Laser and focusing optics

Plasma was produced by Transversely Excited Atmospheric (TEA) CO₂ pulse lasers whose nominal energy E_i was 10 J. The lasers were made by Usho optical system, ltd, and their specifications are summarized in Table 4.1. The exterior is shown in Fig. 4.1 (a). The electric circuit is shown schematically in Fig. 4.2. The electric circuits and the diameter of the laser discharge tube of two lasers are the same. On the other hand, the discharge tube of IRL-1201 is 2.4 times as long as that of IRL-0501. In general, the laser pulse energy of CO₂ pulse laser is proportional to the discharge volume.

Laser excitation is initiated by triggering the discharge in the gap-switch shown in Fig. 4.1 (b). Voltage applied to the capacitor is controlled using a slide-regulator, and E_i can be changed slightly using the slide-regulator. E_i also depends on the fill-pressure in the laser-discharge tube. Figure 4.3 shows the relation between E_i and the fill-pressure. E_i increases with the fill-pressure. Pulse energy was measured before and after experiments using a joule-meter; consequent shot-to-shot pulse-energy fluctuations were maintained below 5% throughout experimentation.

The laser beam was in the high-order multi-transverse mode: its beam quality factor was approximately 18. The laser beam cross-section can be approximated by a 30 × 30 mm square for both lasers as shown in Table 4.1. Equivalent beam diameter was 34 mm, which was the diameter of a circular beam having the same cross sectional area as the square beam.

Table 4.1: Specification of TEA CO₂ lasers

Product No.	IRL-1201
Max. E_i	10 J
Repetition	single, 0.1 ~ 0.5 Hz
Gas fill pressure	110 kPa,a
Impressed voltage	~ 10 kV
E_i fluctuation	$< \pm 5 \%$
Beam size	30 mm \times 30 mm
Power source	AC100V 50 / 60Hz 3A
Laser gas composition	He: N ₂ : CO ₂ = 84: 8: 8



(a)



(b)

Figure 4.1: Picture of TEA CO₂ laser. (a) Exterior of IRL-1201, (b) laser-discharge tube and gap-switch

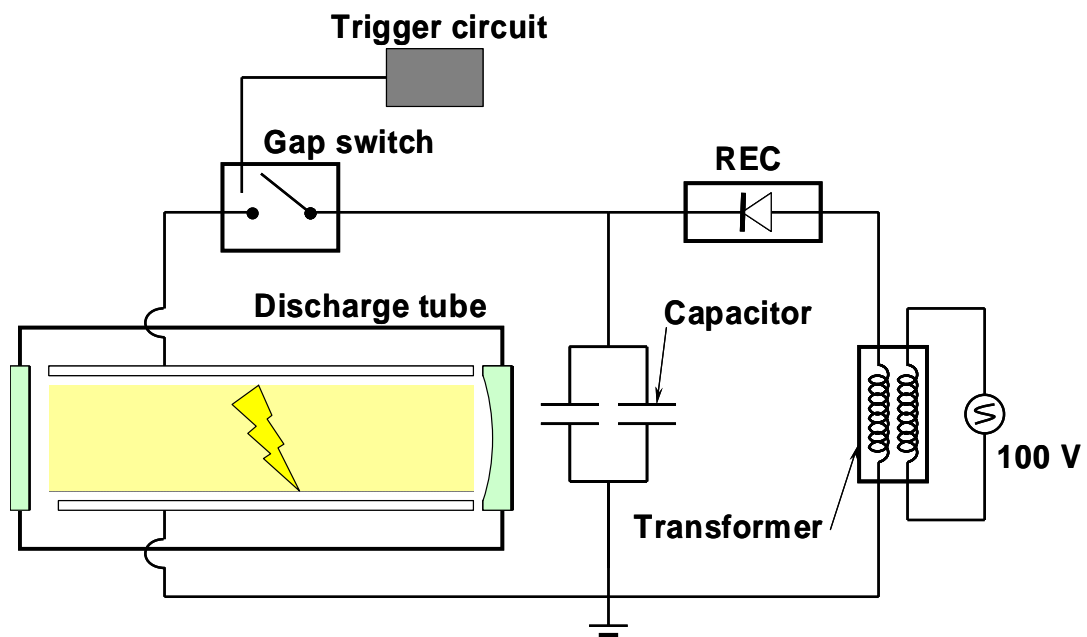


Figure 4.2: Electrical circuit for the TEA CO₂ laser.

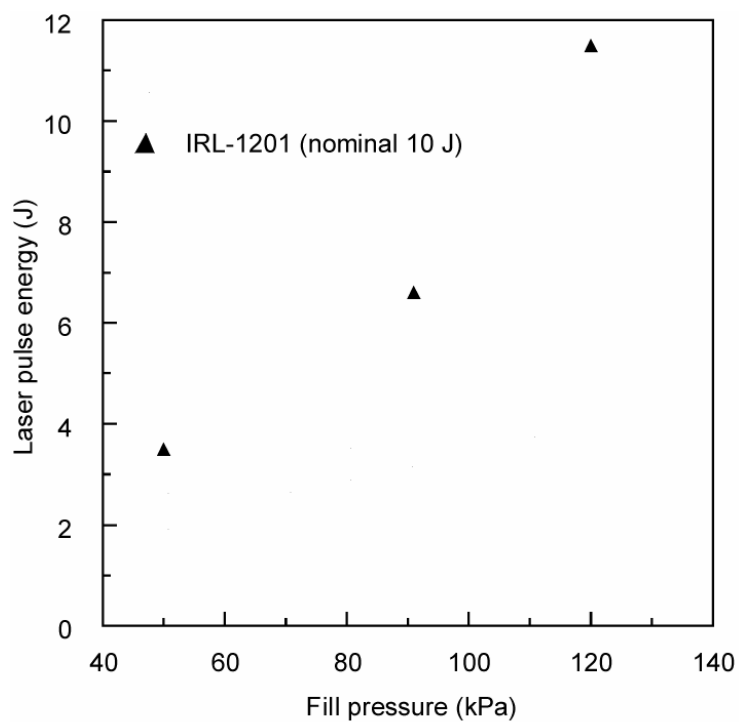


Figure 4.3: Relation between the laser pulse energy and the fill-pressure in the laser-discharge tube.

Pulse shape

Pulse shape was measured using a photon-drag detector (Hamamatsu photonics-B749) shown in Fig. 4.4. The specification of the detector is summarized in Table 4.2. Typical pulse shape is shown in Fig. 4.5. A leading-edge spike appears and an exponentially decaying tail follows. The shape is typical for TEA CO₂ pulse lasers. Full width at half maximum of the spike was $0.12 \pm 0.02 \mu\text{s}$ for $E_i = 10 \text{ J}$ and $0.24 \pm 0.05 \mu\text{s}$ for $E_i = 4 \text{ J}$. The temporal change in the power at the tail $P_{\text{tail}}(t)$ can be approximated as

$$P_{\text{tail}}(t) = P_{0,\text{tail}} \exp\left(-\frac{t}{\tau_d}\right). \quad (4-1)$$

The pulse shape is influenced by the fill pressure in the discharge tube. Figure 4.6 shows the relation between the laser pulse shape and the fill-pressure in the laser discharge tube. The decay-constant of the tail τ_d decreases with the fill-pressure. The duration of the laser irradiation is mostly proportional to the duration of the excitation discharge, which is presumed to decrease with the fill-pressure of the gas in the tube. τ_d depends only on the fill-pressure despite the difference in the discharge volume of two lasers. At the fill-pressure lower than 50 kPa, the reproducibility of the laser pulse shape became quite poor due to the instability of the excitation discharge in the tube. Tests were performed at the fill-pressure lower than 120 kPa for the safety of the discharge tube. With the nominal fill pressure at 110 kPa, the tail decay-constant τ_d was $1.15 \pm 0.05 \mu\text{s}$ for the $E_i = 10 \text{ J}$ and $1.30 \pm 0.03 \mu\text{s}$ for the $E_i = 4 \text{ J}$. The fraction of E_i that is contained in the tail was approximately 75 %. The pulse shape has been measured prior to each experiment.



Figure 4.4: Photon-drag detector

Table 4.2: Specification of Photon-drag detector (Hamamatsu photonics, B749).

Aperture diameter	Sensitivity	Rise time (10~90%)
5 mm	1.2 V/MW	< 1 ns

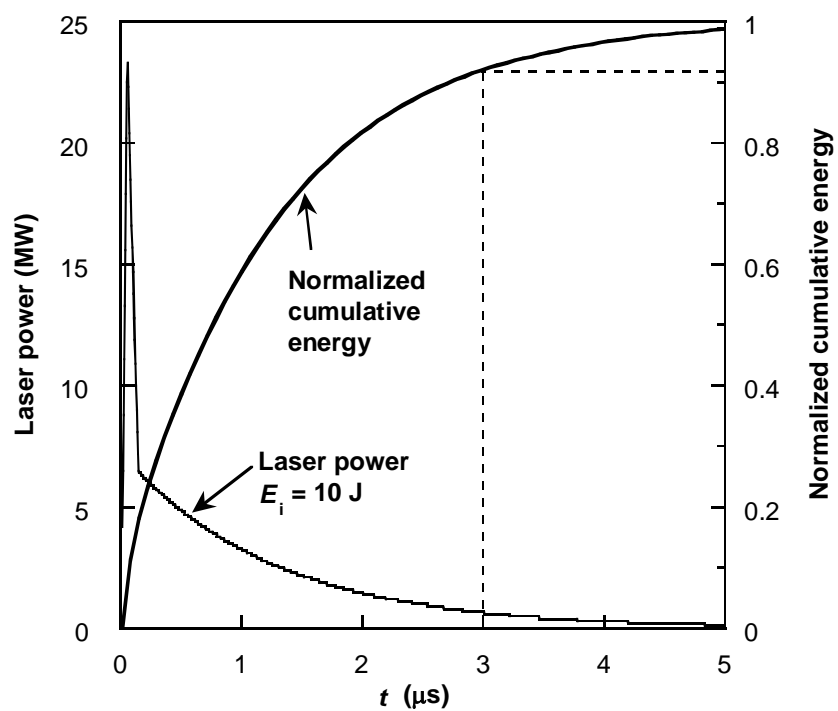


Figure 4.5: Laser pulse shape typical for IRL-1201.

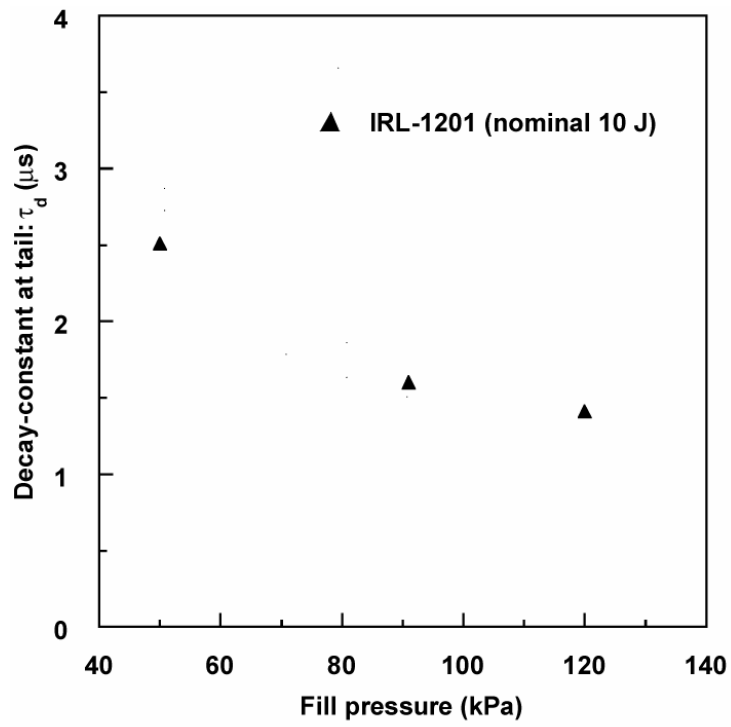


Figure 4.6: Relation between the decay-constant at the exponentially-decaying tail and the fill pressure in the laser discharge tube.

Focusing optic

The laser beam was focused using an off-axis parabola mirror that was free from aberration. The schematic of the mirror is shown in Fig. 4.7. Three mirrors were tested. Their focal lengths were 76.2 mm along the optical axis; their corresponding focusing f -numbers were 2.2. All mirrors reflect an incident laser beam by 90 degrees along the optical axis into focus.

With $f = 2.2$ optics, the minimum spot diameter was estimated at 0.4 mm; the corresponding Rayleigh length was 0.7 mm. In contrast, most of phenomena considered here occurred at 5 - 15 mm upstream of the focus. Hence, laser beam quality was not an important factor in this study.

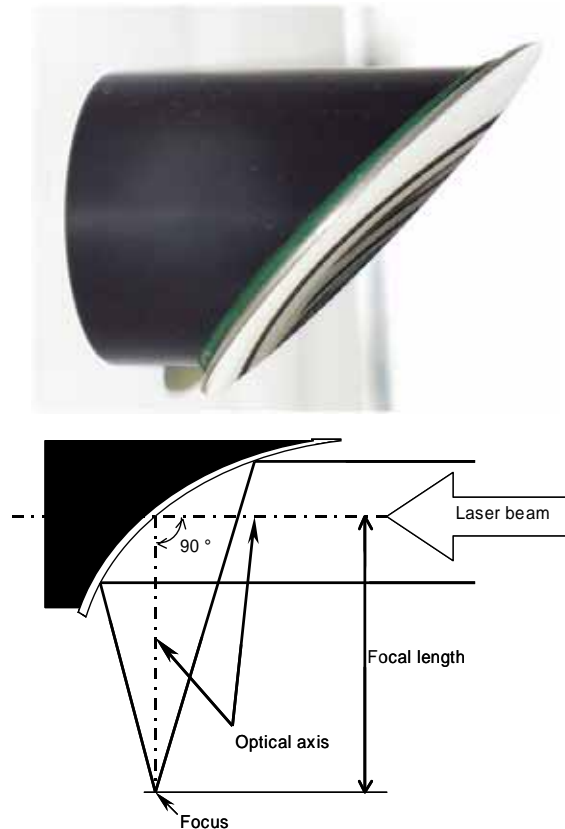


Figure 4.7: Off-axial parabola mirror.

4.2 Imaging Optics

4.2.1 Light Source System

Light Source, Condenser and Source Slit

In order to acquire an accurately parallel fringe with good contrast, the light wave form must be aligned to be homogeneous waves, i.e., waves for which surfaces of a constant phase are simultaneously surfaces of constant amplitude.

Making such homogeneous light waves is required not only in an interferometry method but also in the other various visualization methods, such as shadowgraph or schlieren method. Such homogeneous light waves is produced by the method to focus the laser (or lamp) illumination by condenser lens on a source slit in Figure 4.8, which is originated from the Toepler idea. By using this method, the irregular light is cropped by the source slit. Therefore, a regular approximately-uniform effective light source, which can be sharply defined, is produced. The wave form of the light emitted from this effective light source is approximately a spherical wave form, so this spherical wave form is transformed into the plane wave, which surface has a constant phase, by the collimate lens. Here, it should be noted that, in the case of using laser as the light source, the homogeneous wave could not be strictly realized because of its spatial Gaussian distribution of the amplitude. In addition, in the case of using laser as the light source, its high coherency produce a obstructive fringe pattern like Newton ring, which would be due to interfere the transmitting laser light with the reflected laser light by the condenser lens.

Figure 4.9 shows the set-up image of the light source in this experiment.

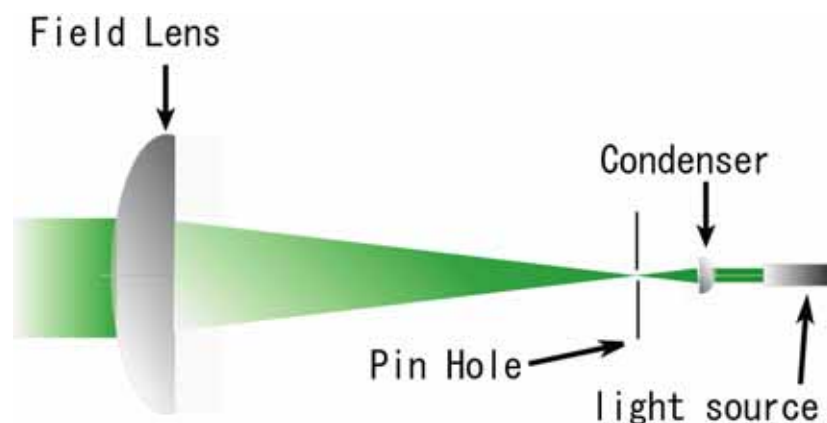


Figure 4.8: Schematic of laser light system

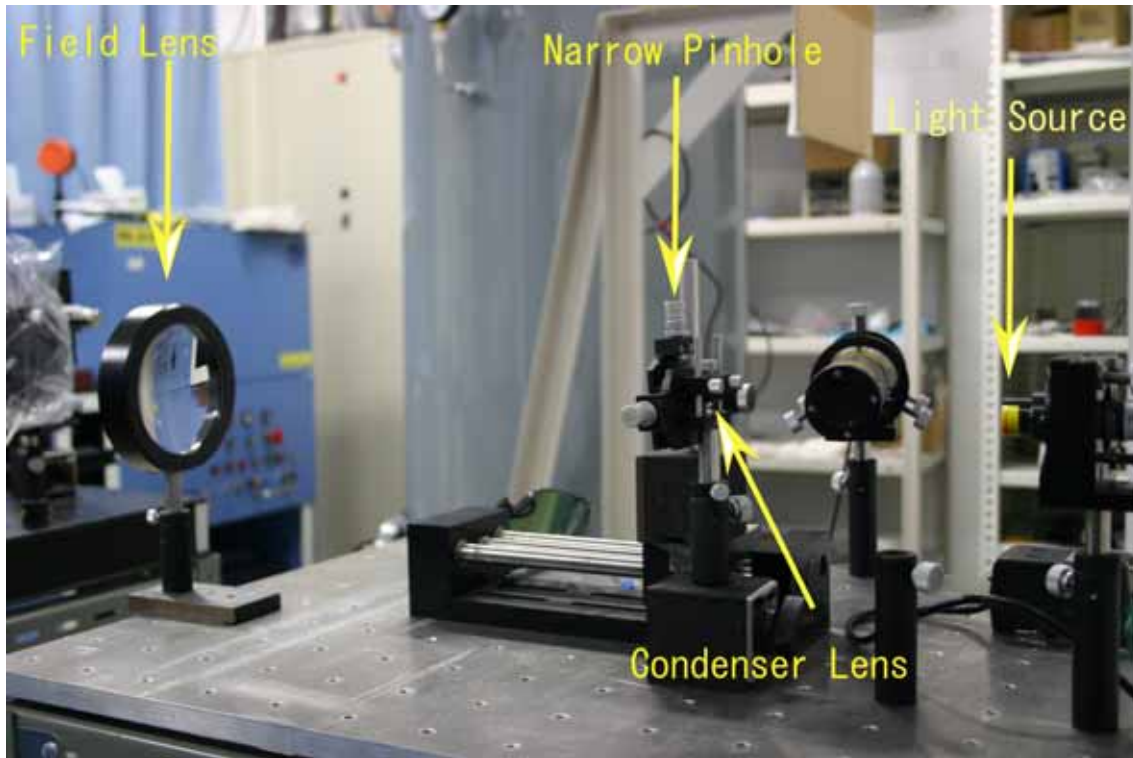


Figure 4.9: Picture of experimental setup of light source system

●Notice in choosing the light source●

In the case of observing a low-emissive phenomenon by shadowgraph or schlieren method, using the low-coherent light source such as flash lamp is recommended to acquire a good contrast figure.

On the other hand, in the case of observing a high-emissive phenomenon by shadowgraph or schlieren method, using laser as a light source, which is a high-monochromatic light source, is recommended because the band path filter are usually used to cut off the emission from the emissive region. In addition, in the case of observing a phenomenon by using interferometry method, using laser as a light source is also recommended due to its easiness in the alignment because of its high coherency.

The comparisons of the applicable light sources classified by the observed region and observing method are summarized in Table 4.3.

●Notice in choosing the collimate lens●

Biconvex (or biconcave) lens and plane-convex (or plane-concave) lens should be used as the situation demand. In the case that conjugate ratio, which is defined as the ratio of the distance from the lens to the image and the distance from the lens to the object, is equal or near to infinity, that is

in the case that the one side of the light is parallel light, plane-convex (or plane- concave) lens should be used. On the other hand, the conjugate ratio is near to 1:1, Biconvex (or biconcave) should be used. Therefore, in choosing the collimate lens, plane-convex (or plane- concave) lens should be chosen. The comparisons of the applicable lens classified by the conjugate ratio are summarized in Table 4.4.

Table 4.3:Comparisons of applicable light sources classified by the observed region and observing method

	Emission region	non-emission region
Shadowgraph (Shlieren)	Laser	Laser
	Lamp	lamp
Interferometry	laser	laser
	Lamp	lamp

Table 4.4: Comparisons of the applicable lens classified by the conjugate ratio

Conjugate ratio	plane-convex	Biconvex	Achromatic
Infinity (parallel beam)			
10:1			
5:1	(pair)		(pair)
1:1	(pair)		(pair)

4.2.2 Built-up Imaging System

Focusing lens

In order to obtain good interference, shadowgraph, and schrielen pictures, the picture system must be built up strictly. Although strictly setting up the picture system is not to be needed if the incident light is completely parallel, such complete parallel light can not be produced pratically. The reasons are as follows

- **The light source is not the complete point source**
- **The accuracy of the collimate lens is not perfect**
- **The position of the collimate lens is not perfect**
- **The measured object refracts the light**

The basic equation to set up the picture system is as follows

$$\frac{1}{a} + \frac{1}{b} = \frac{1}{f} \quad (4.2)$$

a , b show the distance from the lens to the measured object and from the lens to the image is respectively. f shows the focal length.

From Eq.(4.2), the following convenient equation is derived.

$$a = f\left(\frac{1}{m} + 1\right) \quad (4.3)$$

$$b = f(m + 1) \quad (4.4)$$

where m is the magnification.

●**Notice in choosing the focusing lens**●

According to Table 4.4, the biconvex lens is likely to most adaptive to our measurement, in which the conjugate ratio is near to 1:1. However, the plane-convex lens is used in this study because the parallel laser beam must be focused on the pinhole in order to cut off the emission from the plasma. By using the biconvex lens at the permission of the emission effect or using the combination of the plane-convex lens, more beautiful pictures might be obtained.

Camera

To picture a high-speed phenomenon clearly, two types of combination about the light source and the camera are considered. One type is the combination of the pulse light source and the continuous exposure camera, and the other is the combination of the CW light source and the pulse shuttering camera. In this study, the latter type are applied.

To picture a high-speed phenomenon clearly by using the latter type, the exposure time scale of a camera is needed to be shorter than the time scale of the phenomenon. To satisfy this requirement, Intensified Charged-Couple Device (ICCD) camera is used. The shutter timing and the exposure time of ICCD camera is controlled electrically, so high speed shuttering is possible. ICCD camera has the electron amplification channels to compensate the decrease of the photoelectrons by the decrease of the exposure time.

Table 4.5 shows the specification of the ICCD camera used in this study

Figure 4.8 and Figure 4.9 shows the schematics of its image and the Image Intensifier and InstaSpecTMV Head.



Figure 4.10: Picture of ICCD camera

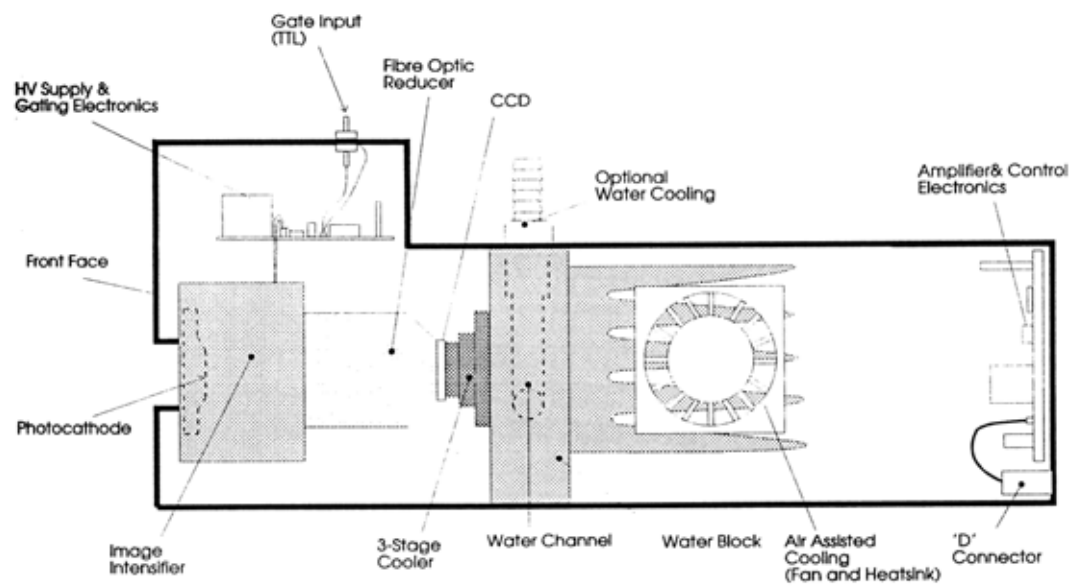


Figure 4.11: Schematic of InstaSpec™ V Head

Apparatus for cutting off the emission

The emission from the plasma in this study exceeds the laser illumination. In order to cut off the emission, the polarized filter and the band path filter are used. The emission from the plasma is non-polarized, on the other hand, the used laser beam is strongly polarized. Therefore, the emission from the plasma is decreased by the polarized filter. In addition, the emission from the plasma is pleochroitic, on the other hand the laser beam is generally strongly monochromatic. Therefore, the emission from the plasma is decreased by the band path filter drastically.

4.2.3 Time Synchronization System

Delay generator

To capture a high speed phenomenon in an arbitrary timing, a trigger signal for photography must be sent into the ICCD camera. The rising edge of TTL pulse, a trigger signal, determines the timing of photography. On the other hand, the width of TTL pulse determines the exposure time. The TTL pulse, which has an arbitrary width, is generated and sent out at an arbitrary timing by the Delay generator, which image and specification are shown in Fig.4.12 and Table 4.5, respectively. The delay time is originated from the timing that the external or internal trigger signal.



Figure 4.12:Image of Delay Generator

Table 4.5: Specification of optical equipments

	Make	Model number	Note
Nd:Yag laser	SUWTECH(China)	DPGL-3005F	W=5[mW]
He Ne laser	NEWPORT	R-30993	W=12[mW]
Condense lens	SIGMA KOKI	SLB-08-15P	$\phi=8[\text{mm}]$ $f=15[\text{mm}]$
Source Slit	SIGMA KOKI	PA-10HEL	$\phi=10[\mu\text{m}]$ $<50\text{MW}/\text{cm}^2$
Collimate lens	SIGMA KOKI	SLB-100-400P	$\phi=100[\text{mm}]$ $f=400[\text{mm}]$
Beam Splitter1,2	=====	=====	$\phi=40[\text{mm}]$
Mirror 1	SIGMA KOKI	TFA-80C12-1	$\phi=80[\text{mm}]$ Quality:λ
Mirror 2	=====	=====	Dielectric multilayer mirror Quality:$\lambda/4$
Polarized filter	SIGMA KOKI	SPF-50C-32	
Imaging lens	SIGMA KOKI	SLB-100-500P	$\phi=100[\text{mm}]$ $f=500[\text{mm}]$
Band-path filter	=====	=====	$=532 \pm 1\text{nm}$ $=633 \pm 1\text{nm}$
ICCD camera	ORIEL INSTRUMRNTS	77193-5	Minimum exposure time 5ns
Delay generator	Stanford Research System,Inc	DG535	Rise time 2ns External Trigger Threshold 2.56V

4.3 Imaging Setup

The experimental set-up is shown in the Fig.4.10. The advance discharge light in the gap switch of the CO₂ laser just before its emission converged by the photo detector into the electric signal, which is the external trigger for the delay generator. The delay generator sent out the trigger signal for photography to ICCD camera at an arbitrary timing with an arbitrary pulse width. By using this system, the pictures at an arbitrary timing could be taken at an arbitrary exposure time.

A Nd:Yag laser was used as a light source for Interferometry. Emission from the plasma was decreased selectively by a band-path filter transmitting the wavelength of $532 \pm 1\text{nm}$ and the polarized filter.

Picture were taken from $t=3.5\mu\text{s}$ to $t=6.0\mu\text{s}$. Here, $t=0$ means the time when the laser pulse incidence began. Laser power decreased to 1% of peak power at $t=5\mu\text{s}$, as shown previously in Fig.4.5. Pictures were taken every 250ns with exposure time 80ns. Pictures were taken three times

for each case.

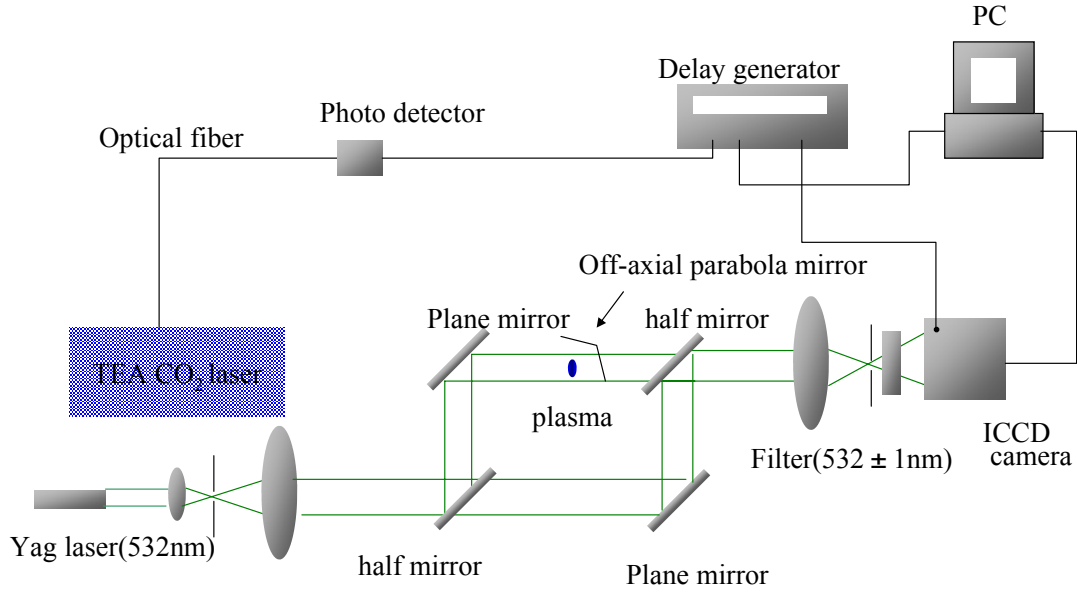


Figure 4.13: Imaging Setup

4.4 Shadowgraph Images

The experimental set-up for the shadowgraph is easily constructed by blocking the reference beam in Fig.4.13. Figure 4.14 shows shadowgraph images in the case of the $E_i=10\text{J}$ and $f=2.2$ in the atmospheric air. Compared with the previous shadowgraphs, the emission from the plasma is completely cut off. However, much information in LSD regime is not obtained by these images because LSD regime is dark because of the refraction or the absorption of the probe beam.

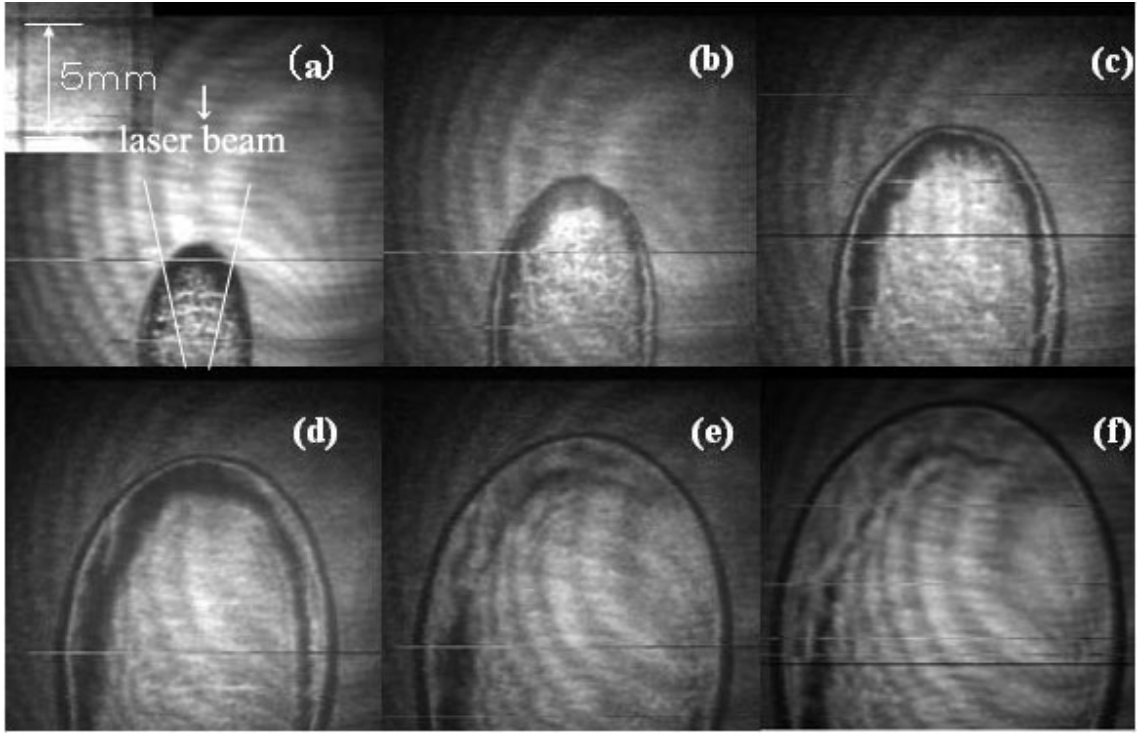


Figure 4.14:Shadowgraphs in the atmospheric air.
t=(a)1.0 μ s,(b)2.0 μ s,(c)3.0 μ s,(d)4.0 μ s,(e)5.0 μ s,(f)6.0 μ s
Exposure time:80ns

4.5 Interference Images

Figure 4.15 shows interference figures in the case of the $E_i=10\text{J}$ and $f=2.2$ in the atmospheric pressure. The laser beam is irradiated from the top in each picture. The spatial frequency of the fringe is estimated to $400\mu\text{m}$. In order to measure the electron density distribution in the area near the laser absorption regime with high spatial resolution, the regime, where the distance from the leading shock front is about 8mm, is expanded and pictured.

As shown in the picture at $t=3.5\mu\text{s}$, the fringe pattern is found to change discontinuously around the plasma surface. In addition, the contrast is inferior compared with the other regime because the laser beam is refracted. The discontinuous fringe shift and the refraction are occurred from the common reason that the refractive index varies drastically at the plasma surface. This is considered as the main reason why a good contrast interference picture could not be obtained in LSD regime because the variance of the refractive index is more drastically in LSD regime,.

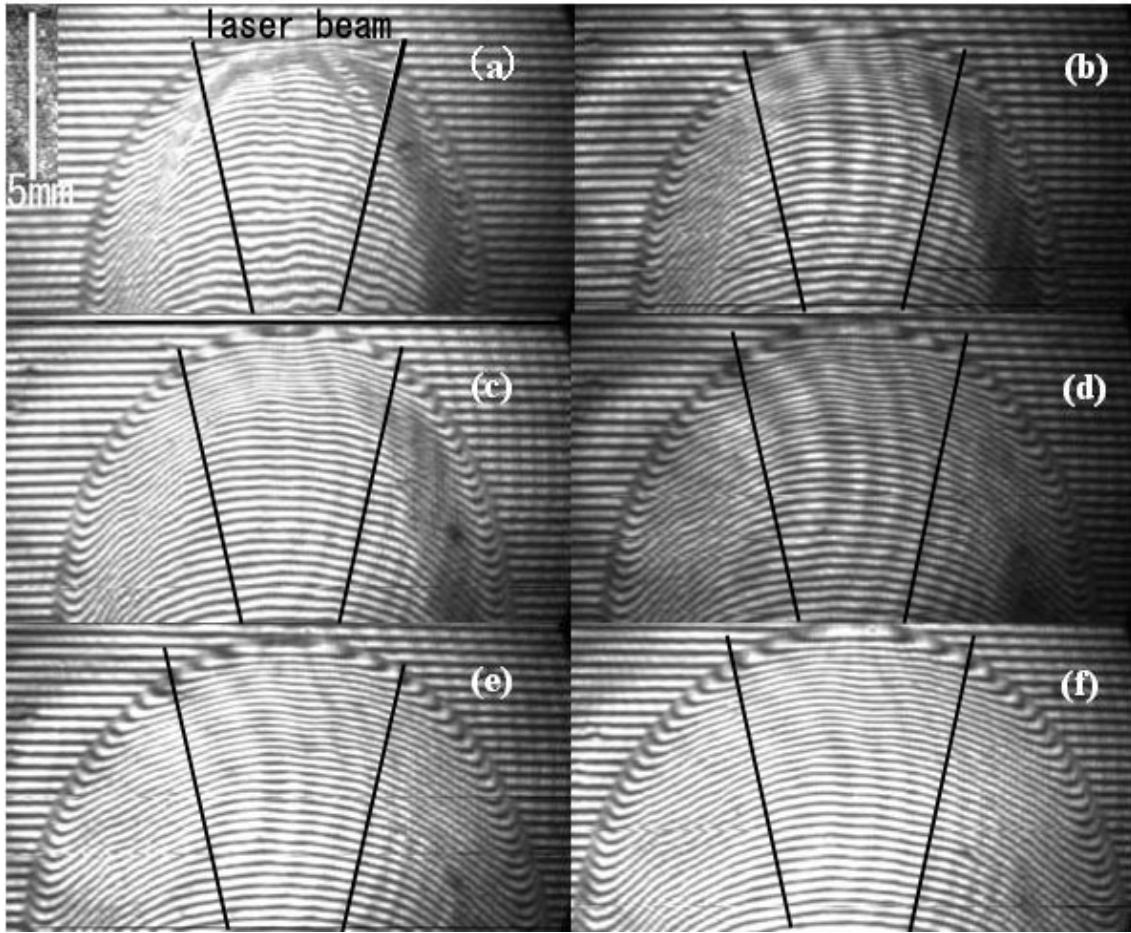


Figure 4.15: Interferograms in the atmospheric air.

$t=(a)3.5\mu s, (b)4.0\mu s, (c)4.5\mu s, (d)5.0\mu s, (e)5.5\mu s, (f)6.0\mu s$ Exposure time: 80ns

4.6 Electron Density Profile

4.6.1 2-Dimensional Electron Density Profile

Figure 4.16 ~ Figure 4.25 show the 2-dimensional electron density profile of the plasma in the decay time of LSD regime from interferograms by using the analytical method as mentioned in the section 3.3. The electron density is found to decrease monotonously with the time.

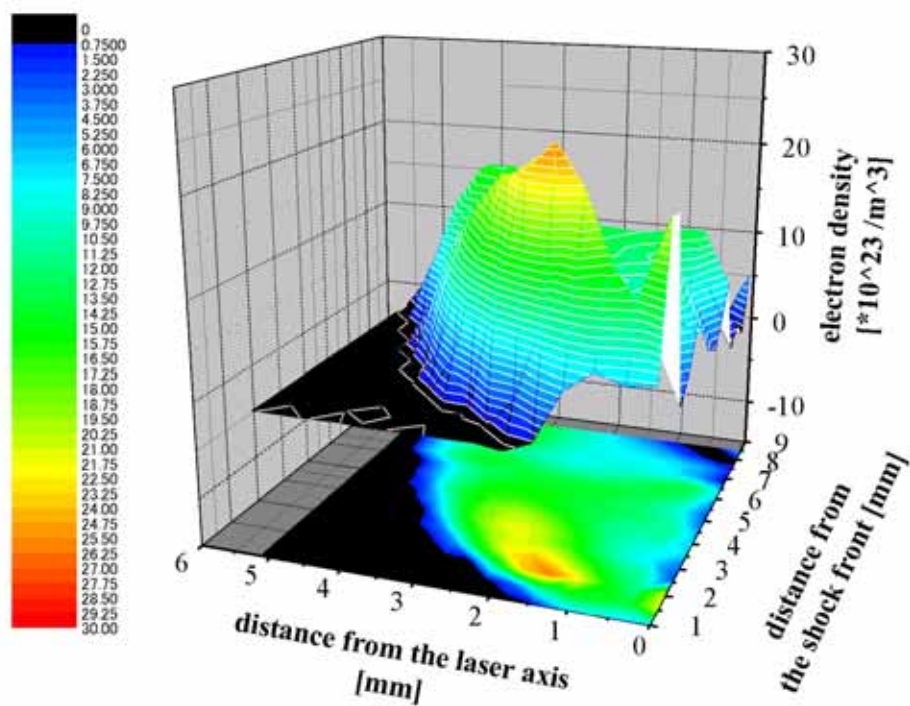


Figure 4.16:2-dimentional electron density profile. $t=3.75\mu s$

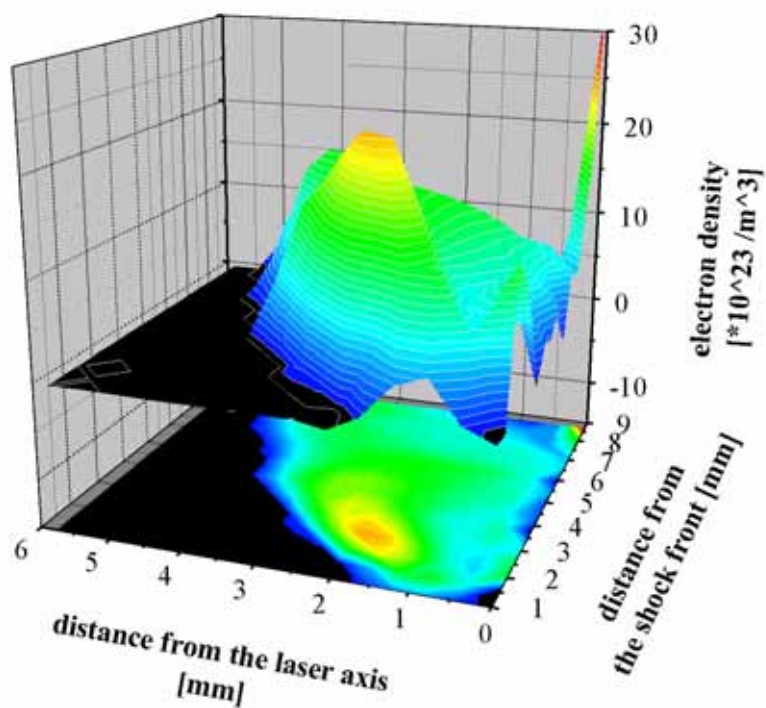


Figure 4.17:2-dimentional electron density profile. $t=4\mu s$

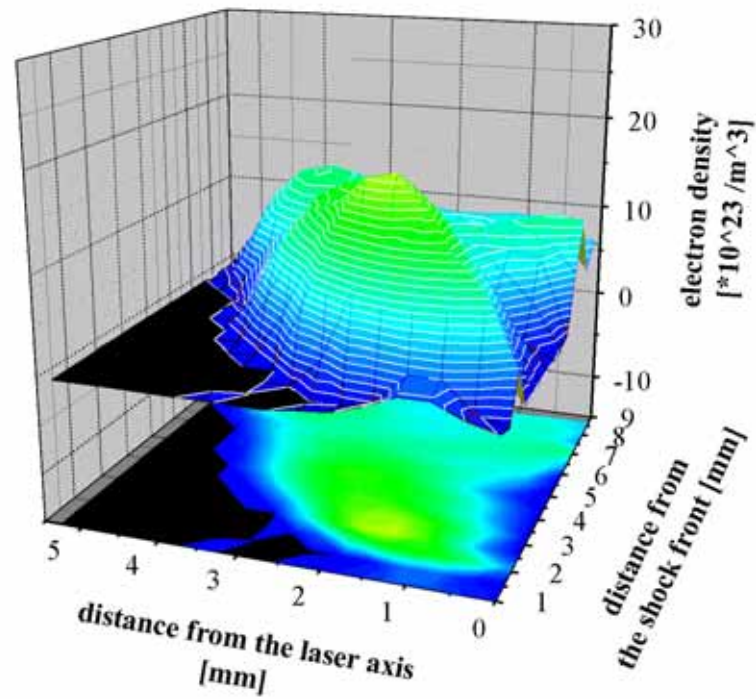


Figure 4.18: 2-dimentional electron density profile. $t = 4.25 \mu\text{s}$

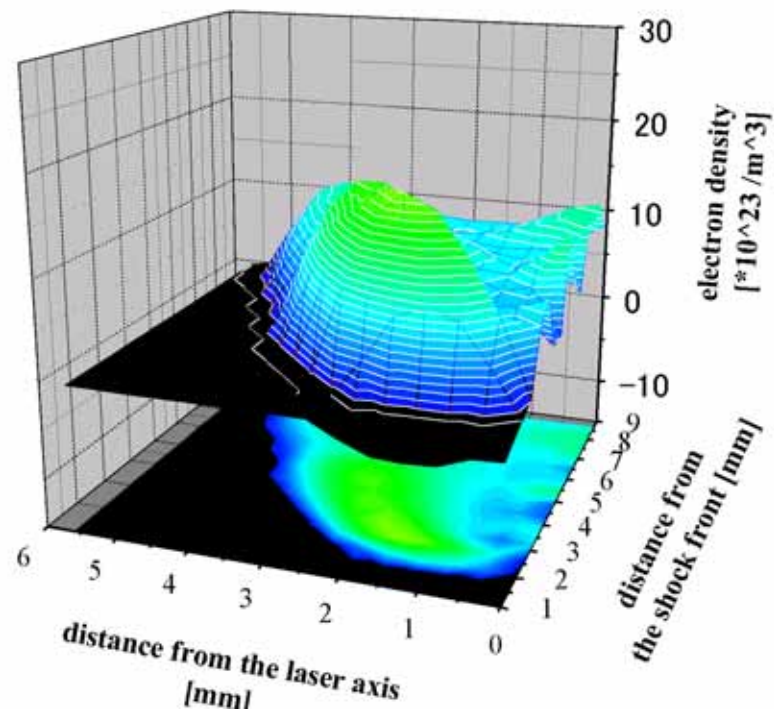


Figure 4.19: 2-dimentional electron density profile. $t = 4.5 \mu\text{s}$

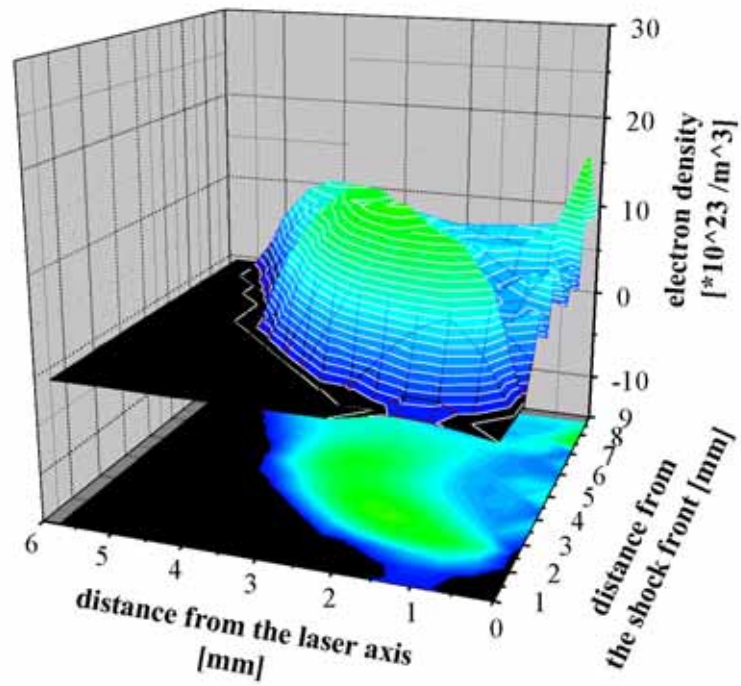


Figure 4.20: 2-dimentional electron density profile. $t=4.75\mu\text{s}$

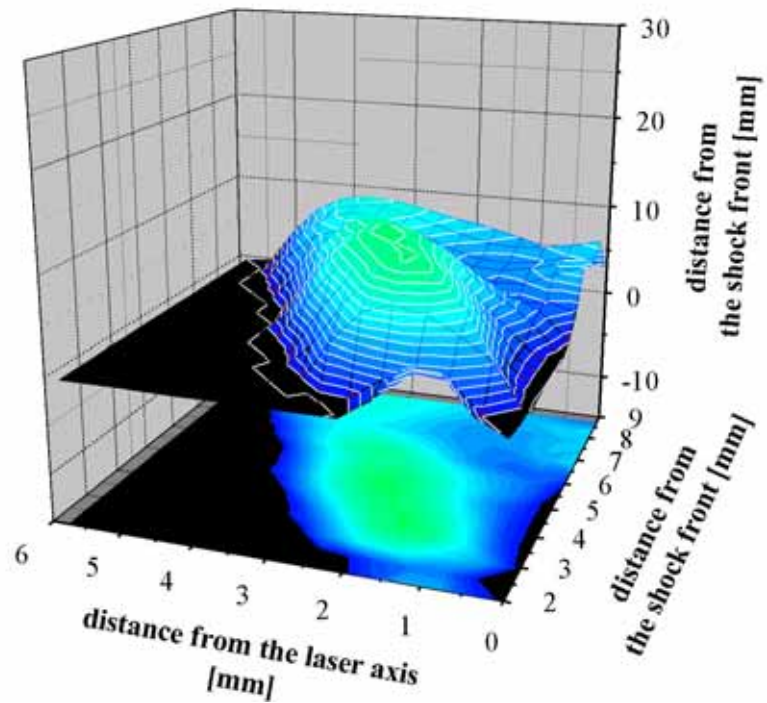


Figure 4.21: 2-dimentional electron density profile. $t=5\mu\text{s}$

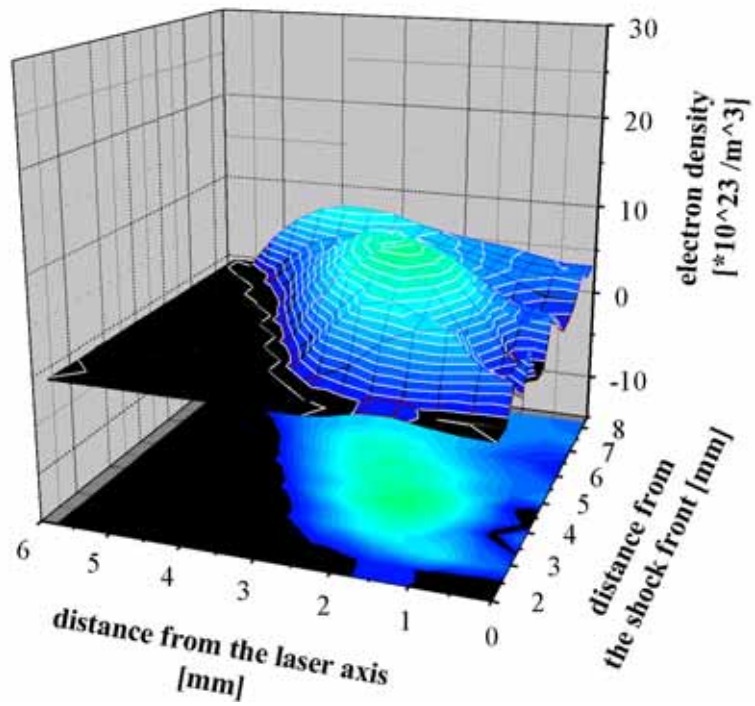


Figure 4.22:2-dimentional electron density profile. $t=5.25\mu\text{s}$

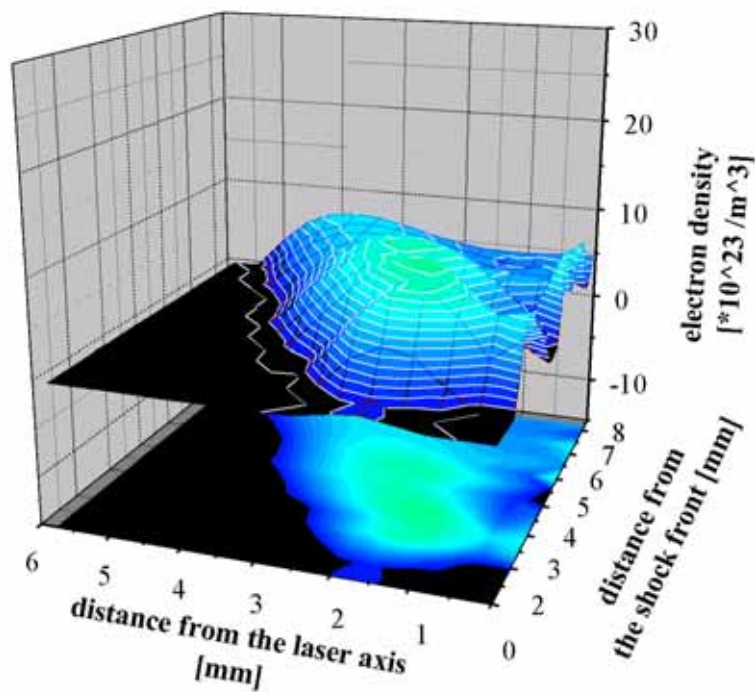


Figure 4.23:2-dimentional electron density profile. $t=5.5\mu\text{s}$

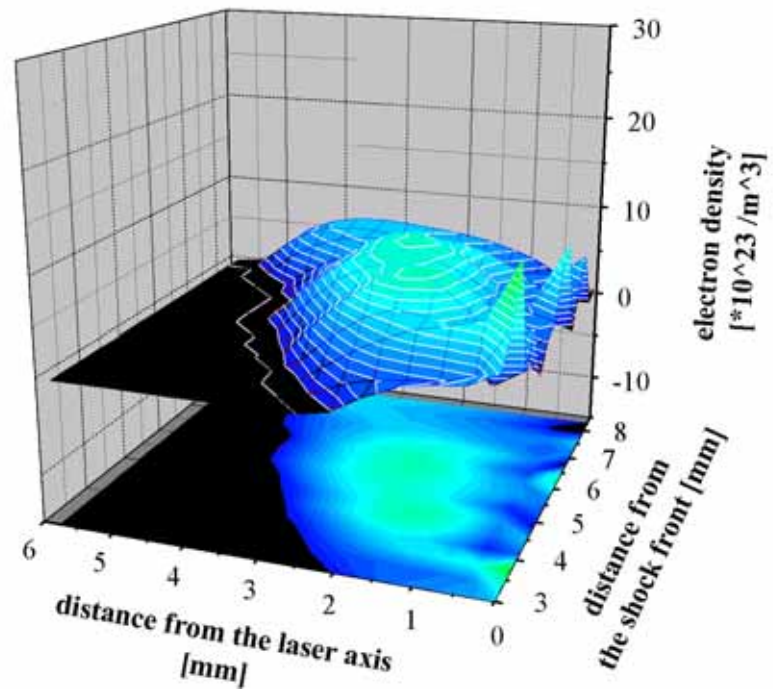


Figure 4.24:2-dimentional electron density profile. $t=5.75\mu\text{s}$

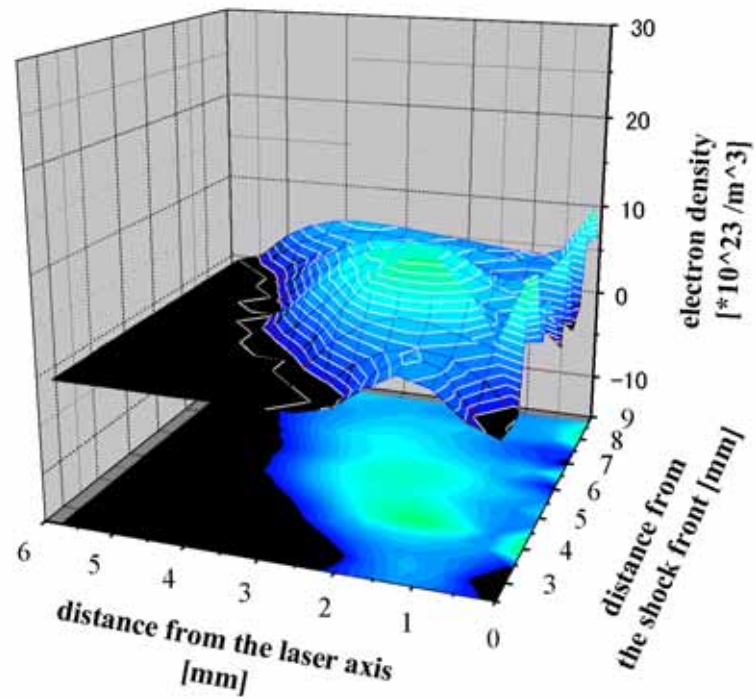
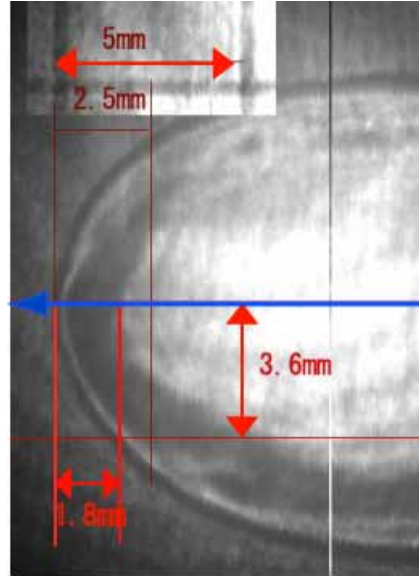


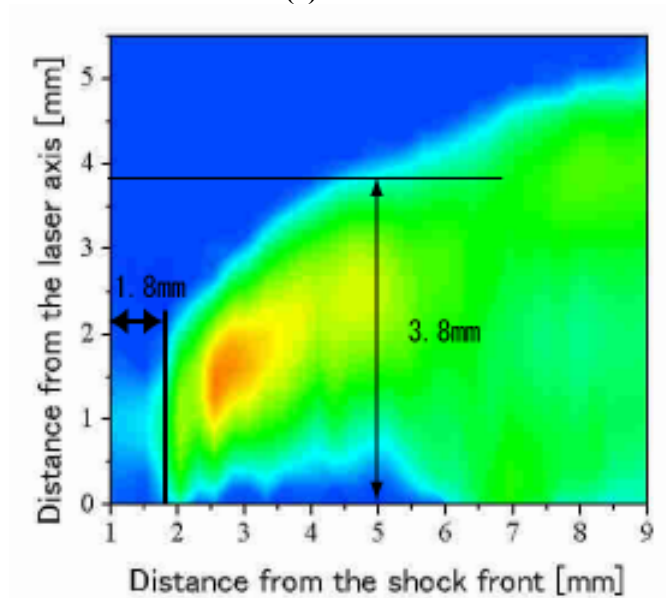
Figure 4.25:2-dimentional electron density profile. $t=6\mu\text{s}$

4.6.2 Comparison of the Plasma Shape

Figure 4.26 shows the comparison of the plasma shape estimated from the electron density distribution derived from interferograms with the plasma shape estimated from the shadowgraph image at $t=4.25\mu\text{s}$. These figures were compared from two points. One is the distance from the shock front to the plasma front, and the other is the plasma radius in the 5mm internal line from the shock front. As shown in the Fig.4.26, the plasma shapes determined both from the electron density profile and from the shadowgraph image give very good agreement.



(a)



(b)

Figure 4.26: Comparison of the shape of the plasma judged from the shadowgraphs image (a) with the shape of the electron distribution judged from interference figure(b)

4.6.3 Radial Electron Density Profile

The radial electron density distribution in the case of the $E_i=10\text{J}$ and $f=2.2$ in an atmospheric air are shown in Figure 4.27, which is obtained by analyzing where the distance from the leading shock front is 3.74mm in the $t=4.25\mu\text{s}$ image

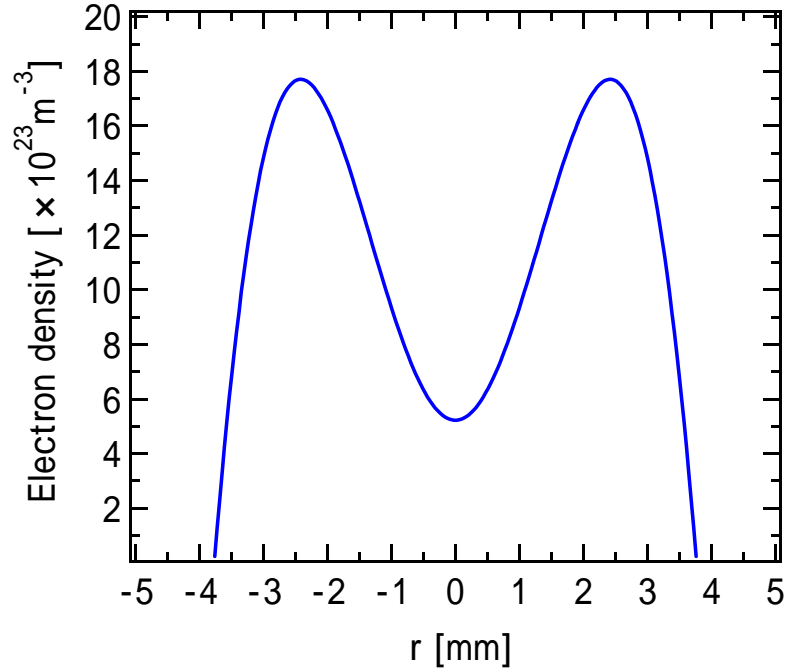


Figure 4.27: Typical radial electron density profile
 $t=4.25\mu\text{s}$
Distance from the shock front is 3.74mm

4.6.4 Longitudinal Electron Density Profile

The electron density along the CO_2 laser axis has an error, which is originated from the error in the fitting process and is amplified through the Abel deconvolution. Therefore, the new axis is defined as shown in Fig.4.28. Here, θ is 5 degree. Figure 4.29 shows the longitudinal electron density profile along this new axis.

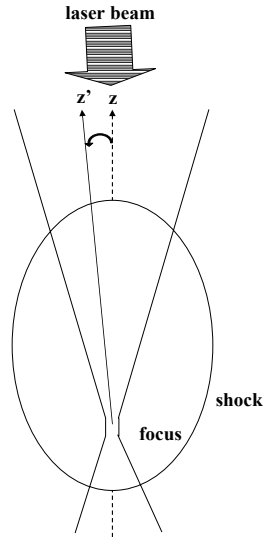


Figure 4.28 : Geometric relationship between the laser axis and assumed axis for the electron density profile

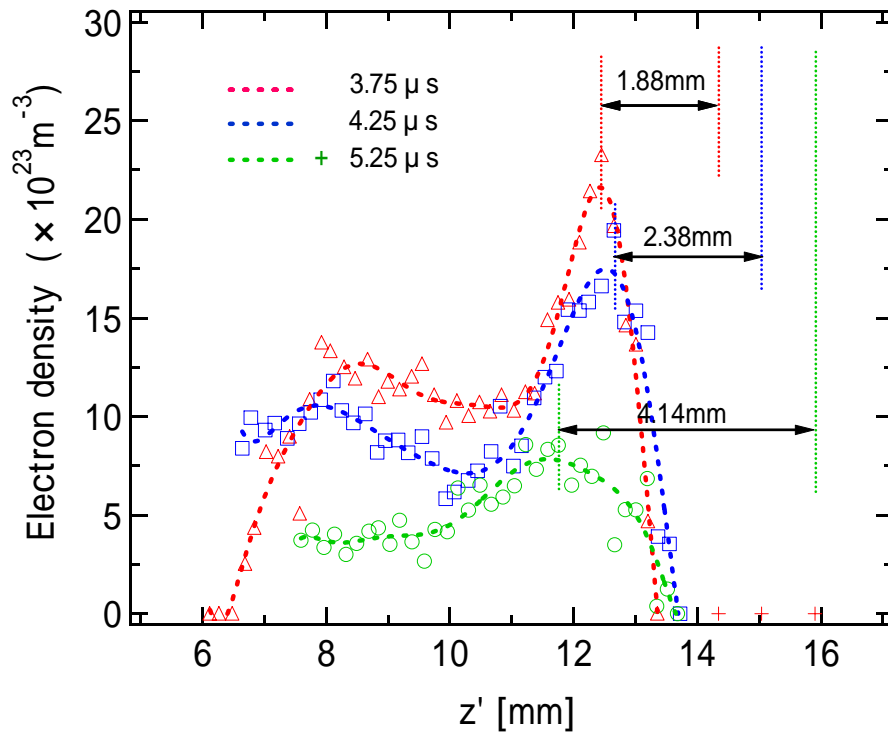


Figure 4.29: Longitudinal distribution of the electron density over a cross section in the laser induced plasma in air at different time

4.6.5 Variation of the electron density around the plasma front

Figure 4.30 shows the history of the electron density gradient after LSD termination, which is obtained from the linear approximation of the steep gradient region around the plasma front.

Figure 4.31 shows the variation of the peak electron density around the plasma front. Figure 4.32 shows the variation of the electron density averaged along with the longitudinal direction.

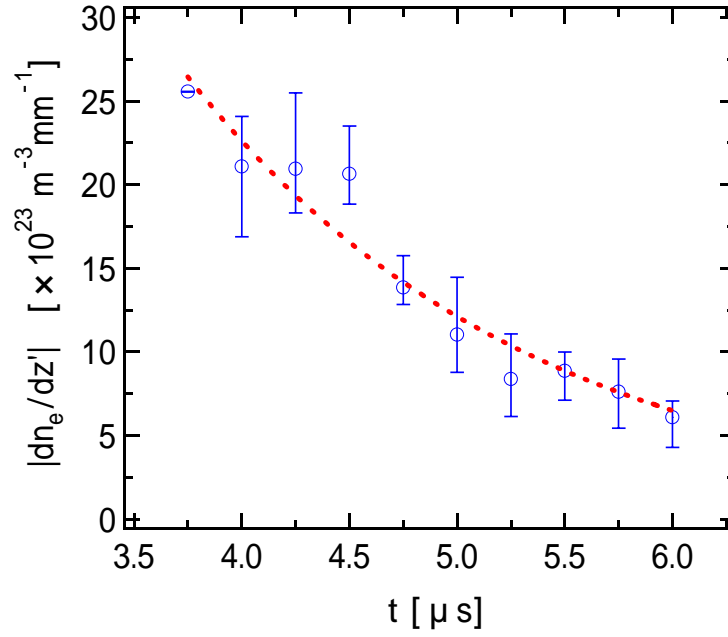


Figure 4.30: Variation of the electron density gradient at the plasma front in the case of Ei=10J, f=2.2, atmospheric air.

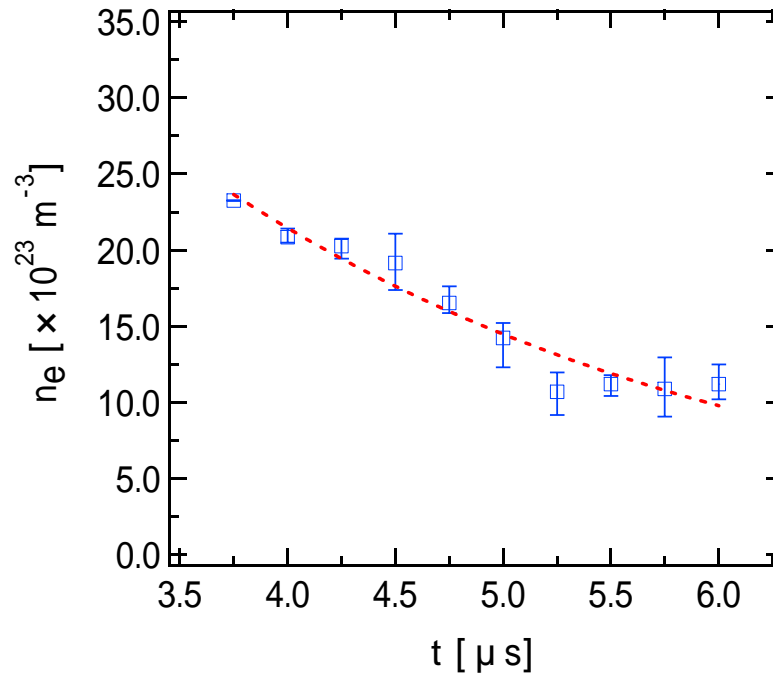


Figure 4.31: Variation of the peak electron density at the plasma front in the case of Ei=10J, f=2.2, atmospheric air.

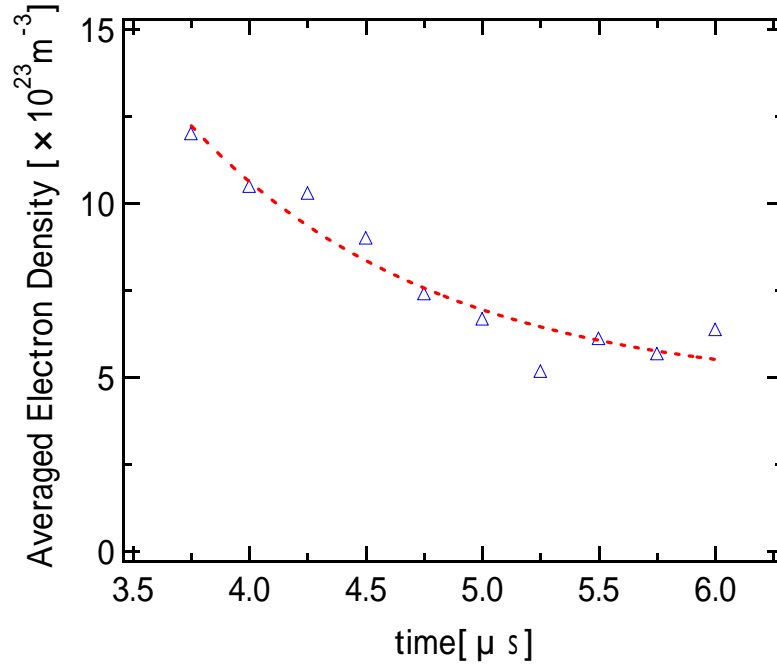


Figure 4.32: Variation of the Averaged Electron Density in the longitudinal direction in the case of $E_i=10\text{J}$, $f=2.2$, atmospheric pressure

Figure 4.33 shows the definition of the width of the laser absorption regime after LSD termination, which is the distance from the position of the peak electron density to the position of the plasma front.

Figure 4.34 shows the variation of the width of the laser absorption regime after LSD termination.

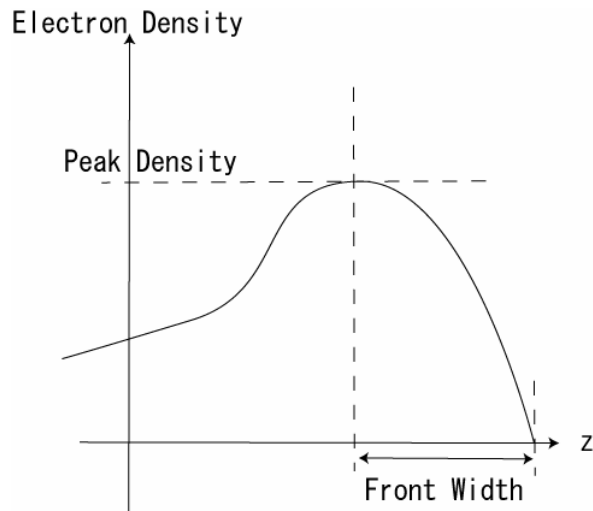


Figure 4.33: Definition of the width of the laser absorption regime after LSD termination

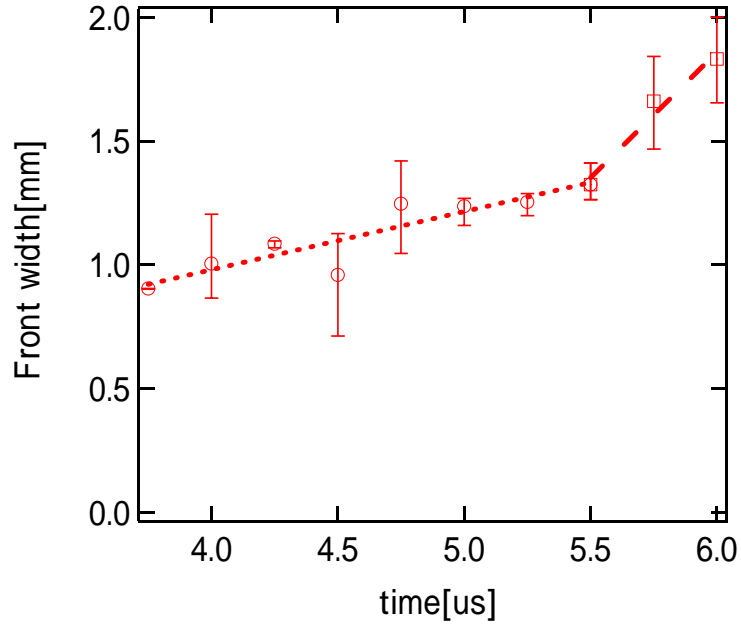


Figure 4.34: Variation of the width of the laser absorption regime after LSD termination

4.6.6 Displacement of Post LSD front

The position of the laser absorption wave front after the LSD termination is defined as the position of the peak electron density near the plasma front. Figure 4.35 shows the displacement of the shock front, emission front and the laser absorption wave front after the LSD termination.

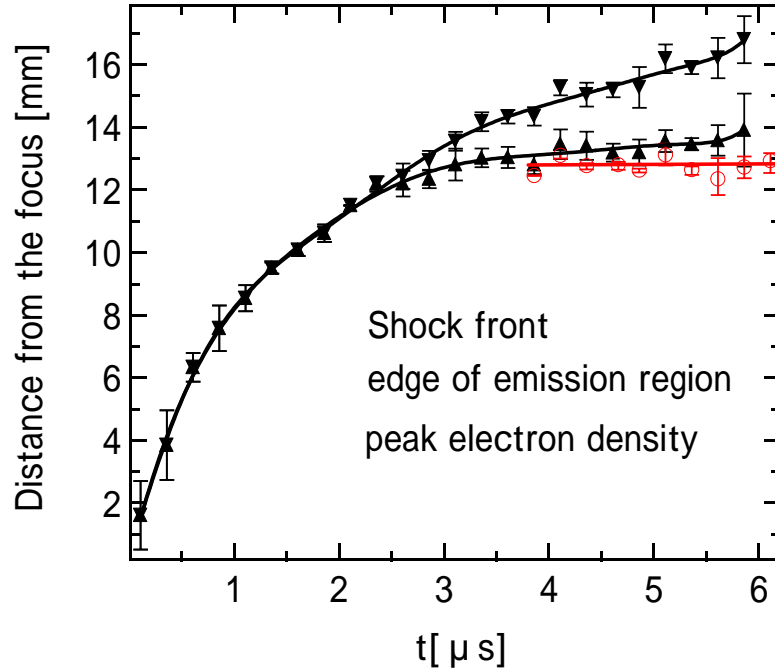


Figure 4.35: Displacement of the shock front, emission front and laser absorption wave front after the LSD termination

4.7 Discussion

4.7.1 Gradient decay of the electron density around the plasma front

Figure 4.16– Figure.4.25 and Figure.4.27 show that the electron is distributed densely around the plasma front and thinly inside the plasma. This tendency of the electron density distribution is matched with the previous other measurements of the electron density in a laser induced plasma. Figure.4.16-Figure.4.25 also show that the electron density totally decreasing with the time.

From Fig 4.29, the electron density around the plasma front is found to hold the steep structure for a moment after LSD termination. At $t=3.75\mu\text{s}$, the electron density gradient around the plasma front $|dn_e/dz|$ is $2.5 \times 10^{24} [\text{mm}^{-1} \text{m}^{-3}]$. However, this steep structure gradually decays.

At $t=3.75\mu\text{s}$ (in Fig. 4.31), the peak electron density is $2.6 \times 10^{24} [\text{m}^{-3}]$, which is near to the critical electron density of CO_2 laser ($\lambda = 10.6\mu\text{m}$), $4.95 \times 10^{24} [\text{m}^{-3}]$. The electron density of LSD regime would be near the critical density considered from its very short scale of laser absorption length, which order is several hundred micrometers by estimating from the emission in LSD regime. Therefore, the measured high electron density region is considered as the remains of LSD regime.

From Fig.4.32, the total electron density is found to decrease, which indicates that the recombination process also contributes to the density decay of the laser absorption regime after the LSD termination.

From Fig.4.35, the laser absorption wave front after the LSD termination is found to be almost rest behind the plasma front after $t=3.75\mu\text{s}$. However, before $t=3.75\mu\text{s}$, the laser absorption wave after the LSD termination is considered to propagate with some velocity because the position of the laser absorption wave front after the LSD termination in this time regime advances from the position of the plasma front at the timing of LSD transition. This propagation of the laser absorption wave front after the LSD termination would be caused by two effects. One is the plasma expansion sustained by the laser absorption in the LSC regime, and the other is the advection.

4.7.2 Plasma temperature

Plasma temperature was estimated from the measured electron density by using the chemical equilibrium calculation. The calculation method is described in the chapter 6 in detail. In this calculation, the self-similar solution of a strong point explosion is adapted because of the ignition of the plasma and the propagation of LSD is similar to the strong point explosion. The self-similar solution of a pressure is shown in Fig.4.36.

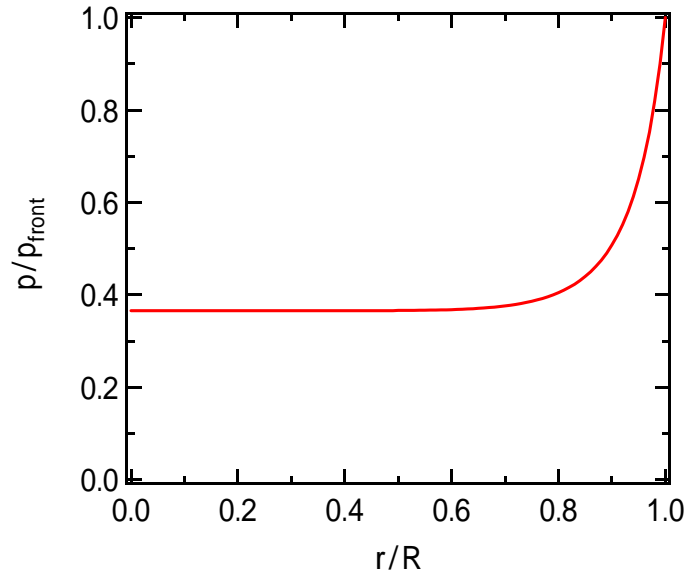


Figure 4.36 Self-similar solution of the strong point explosion⁵⁰

where R is the distance from the explosion point to the shock front and p_{front} is the pressure of the shock front. r is the distance from the explosion point and p is the pressure at the point.

Using the self-similar distribution of pressure, the plasma temperature was estimated as shown in Fig.4.37.

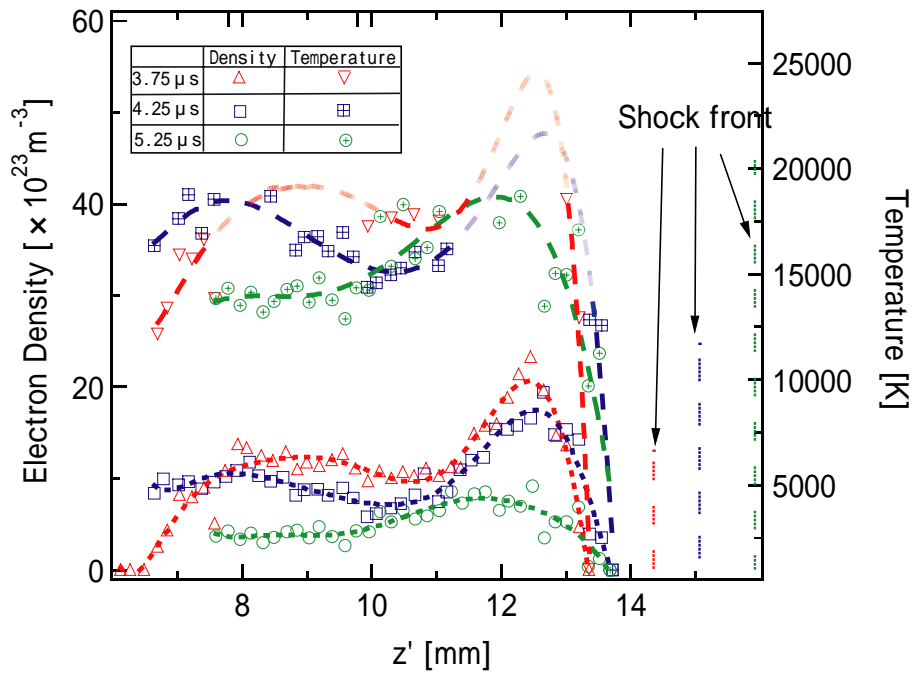


Figure 4.37: Longitudinal distribution of the plasma temperature over a cross section in the laser induced plasma in air at different time

As shown in Fig.4.37, the distribution of the plasma temperature is found to have the steep structure in the plasma edge and the temperature in the laser absorption regime decreases drastically.

Figure 4.38 shows the averaged plasma temperature on the longitudinal axis. The plasma temperature continues to decrease at the time interval from $t=4.5\mu s$ to $t=6\mu s$, which indicate that the energy loss by the radiation in the plasma is not negligible compared with the total thermal energy of the plasma and the energy input by the laser as shown in Fig.4.39. On the other hand, the plasma temperature does not vary so much at the time interval from $t=4.5\mu s$ to $t=5.25\mu s$, τ_{ex} . The reason of this temperature invariance is that the energy loss by the radiation is negligible compared with the total thermal energy of the plasma.

The characteristic time of the energy loss by the bremsstrahlung radiation, τ_{rad-br} is represented by the following equation^{5 1}

$$\tau_{rad-br} = 1.4 \times 10^{17} T_e^{1/2} / N_e \quad (4.4)$$

where T_e [K] is the electron temperature and N_e is the number density of the electron [m^{-3}].

With the electron temperature fixed to 15000[K], τ_{rad-br} varies by the number density of electron as shown in Fig.4.40. From the Fig.4.40, $\tau_{ex} \ll \tau_{rad-br}$ is found to consist. Therefore, the radiation loss by bremsstrahlung at the interval from $t=3.75\mu s$ to $t=6\mu s$ is considered to be negligible to the total thermal energy in the plasma. As a result, the recombination radiation is contributed to the reduction of the plasma temperature dominantly.

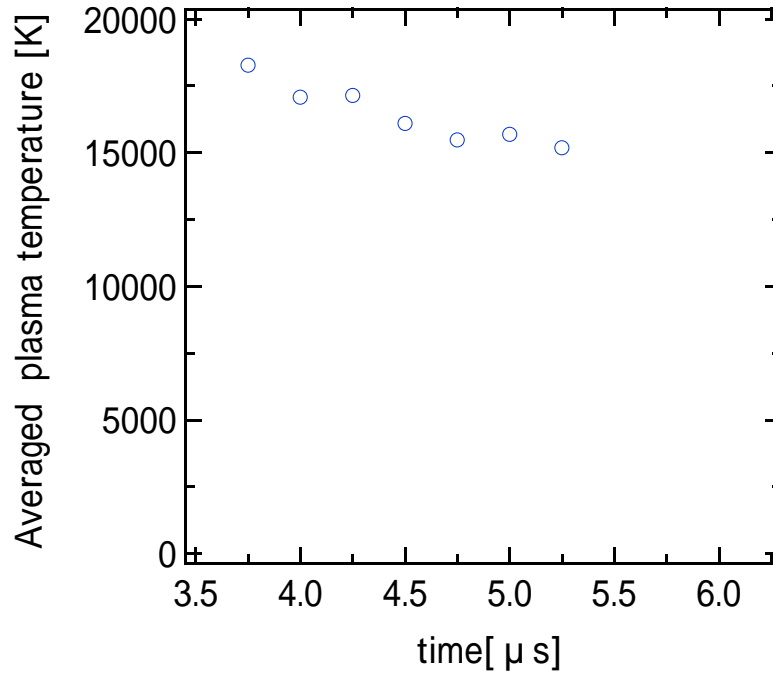


Figure 4.38 Variation of the averaged plasma temperature on the longitudinal axis

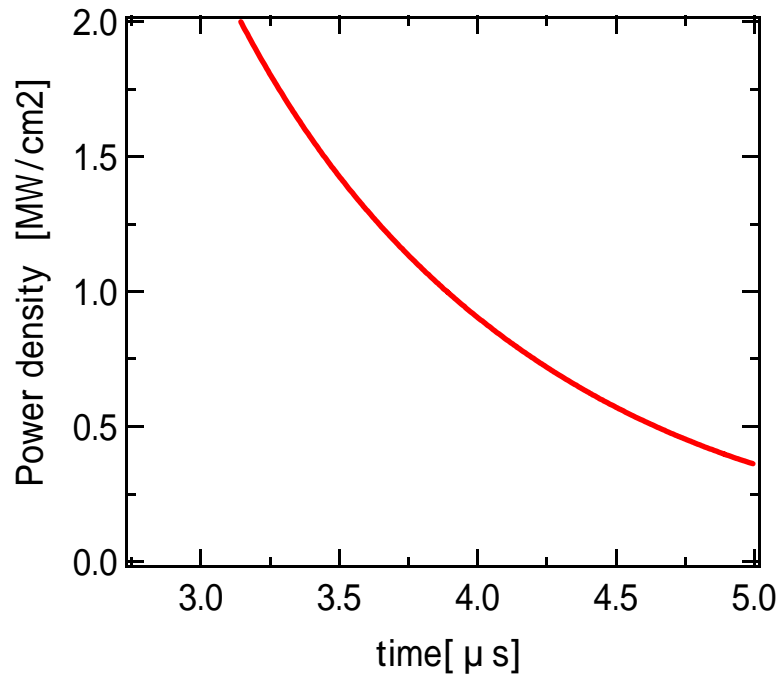


Figure 4.39: Laser power density irradiated on the plasma surface during the laser absorption regime after the LSD termination

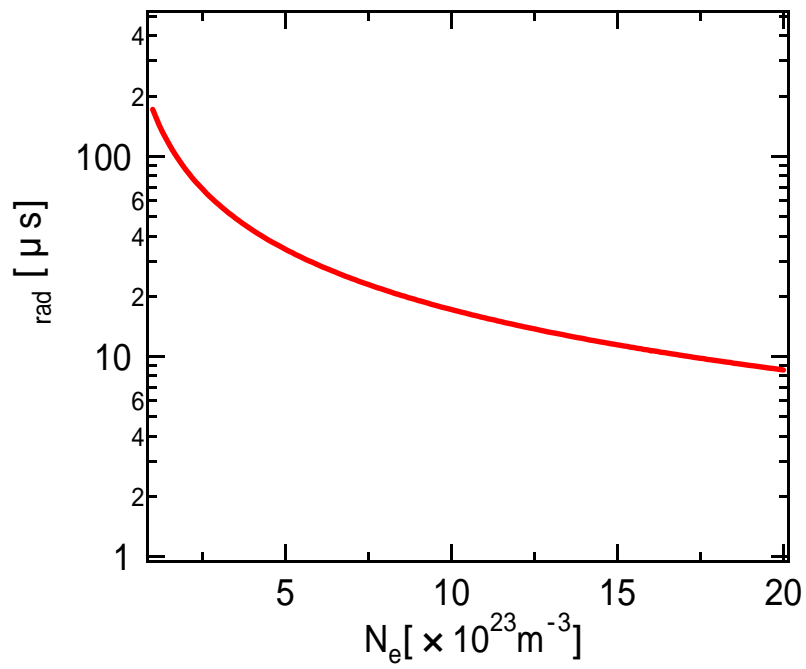


Figure 4.40: Characteristic time of the energy loss by bremsstrahlung radiation with the plasma temperature fixed to 15000K

As shown in Fig.4.37, the plasma temperature in some positions could not be obtained because the calculation does not converge. The reason for the non-convergence is that the pressure distribution in the laser absorption regime after the LSD termination does not completely match with the self-similar solution of pressure. Figure 4.41 shows the calculated electron density with some pressures in the wide range of the temperature. As shown in Fig.4.41, in the typical electron density in this study, which order is 10^{23} [m^{-3}], the convergence of the calculation is strongly dependent on the pressure. The pressure used in this calculation is estimated less than the actual pressure in the laser absorption regime after the LSD termination because the effect of the pressure support by the laser beam are not considered in the point explosion theory.

Although the accurate pressure distribution is not used in this calculation, the calculated temperature is considered to be reliable within the order of several thousand kelvins because the results calculated by using the same electron density ranged in the order of 10^{23} [m^{-3}] and the different pressure ranged from 3×10^5 to 10×10^5 [pa], which are the typical values in this case as shown in Fig.4.42, give the almost same temperature. Therefore, the averaged plasma temperature in the laser absorption regime after the LSD termination is estimated to be 15000 [K].

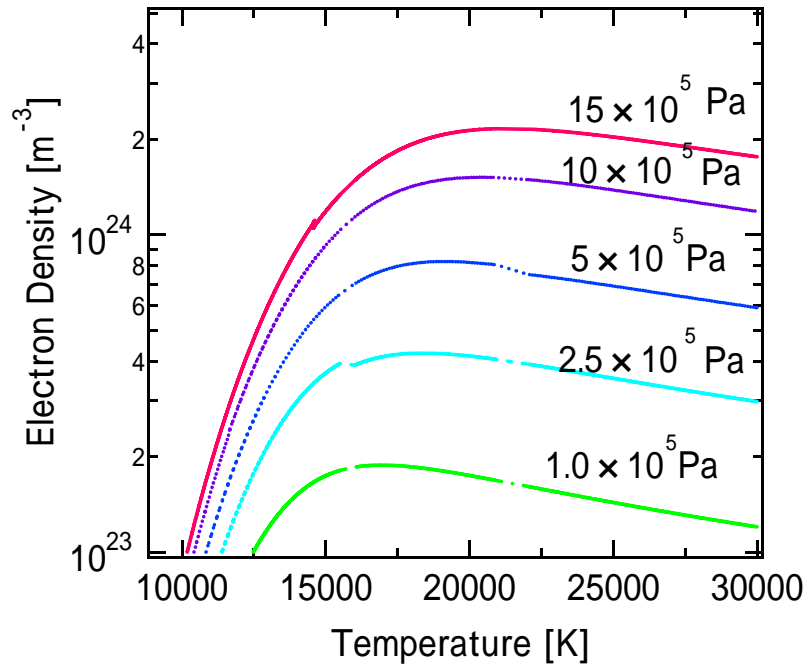


Figure 4.41: Calculated electron density with some pressures in the wide range of the temperature

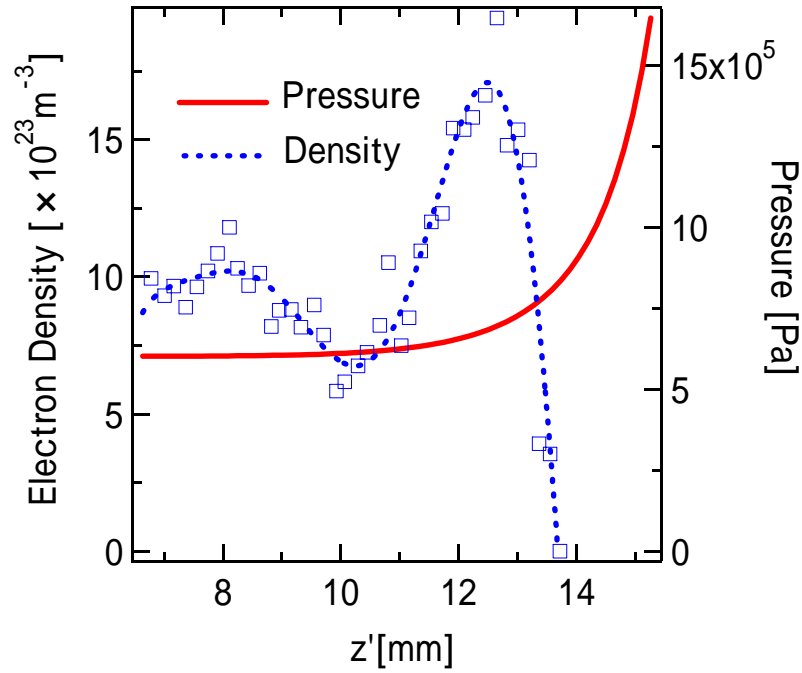


Figure 4.42: Distribution of the electron density and the pressure in the assumption of the strong point explosion at $t = 4.25[\mu s]$

4.7.3 Decay process

The decay process of the electron density gradient in the laser absorption regime after the LSD termination is considered to be caused by two effects. One is the broadening of the laser absorption regime by the electron diffusion or the photoionization by the ultraviolet radiation from the plasma and the other is the decrease in the electron density by the recombination.

The decrease in the laser power density irradiated on the laser absorption regime after the LSD termination causes the plasma to the state of the excessive energy loss by the recombination radiation compared with the energy input. Therefore, the temperature decreases drastically. As a result, the decay of the electron density is occurred.

Chapter5

Calculation of electron Density behind LSD Front

In this chapter, the electron density behind LSD wave and the laser power density for driving LSD wave are calculated by applying the measured velocity of LSD front to the propagation model of the plane LSD wave in an air, which assumes the chemical/thermal equilibrium and the Chapman-Jouguet condition. Contrary to the calculation by applying the measured historical laser power to this model, the calculation by applying the measured velocity of LSD wave could lead to results in consideration of the effect of the energy loss by the enthalpy flow and the radiation out from the laser absorption regime to the all direction and which is also considered the un-uniform laser power density profile.

As a result, the calculated electron density is not enough to propagate LSD wave. The electron density in the laser absorption regime would be less estimated in this calculation by the assumption of the thermal-equilibrium. The thermal non-equilibrium calculation would be needed to obtain more exact physical quantity in the calculation.

5.1 Thermodynamic Relation

The calculation model of the plane LSD wave is shown in Fig.5.1, which assume the uniform distribution of the physical quantities in the plane LSD front. The physical quantities behind LSD wave are calculated by using the following equations, which is consisted of the chemical-equilibrium calculation and the one-dimensional LSD wave relationships^{5 2, 5 3}

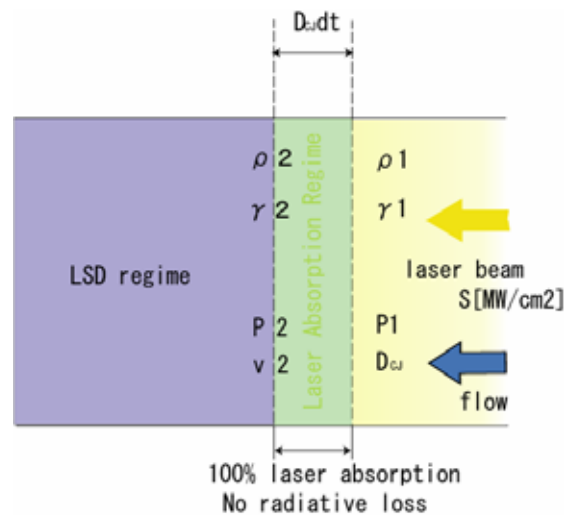


Figure 5.1: Schematic of one dimensional LSD model

$$h_2 + \frac{1}{2}\gamma_2 R_2 T_2 = h_1 + \frac{1}{2}D_{CJ}^2 + \frac{S}{\rho_1 D_{CJ}} \quad (5.1)$$

$$v_2 = \sqrt{\frac{\gamma_2 p_2}{\rho_2}} = \frac{\gamma_2}{\gamma_2 + 1} \left(\frac{p_1 + \rho_1 D_{CJ}^2}{\rho_1 D_{CJ}} \right) \quad (5.2)$$

$$\rho_2 = \frac{(\gamma_2 + 1)\rho_1^2 D_{CJ}^2}{\gamma_2(p_1 + \rho_1 D_{CJ}^2)} \quad (5.3)$$

$$\sum_{s=1}^{n_{sp}} \nu_{r,s} \widetilde{X}_s - \ln K_{eq}^r = 0 \quad (5.4)$$

$$\sum_{s=1}^{n_{sp}} \xi_s^c \exp(\widetilde{X}_s) - Y_0^c \rho_2 = 0 \quad (5.5)$$

The coordinate system moving with the discontinuous wave is used in Eqs.(5.1)-(5.3).

Equation (5.1) shows the energy conservation, in which the subscripts “1” and “2” represent ahead of and behind LSD front. Eq.(5,2) and Eq.(5,3) is derived from the Hugoniot relations in consideration of the Chapman-Jouguet assumptions, in which the flow velocity behind the wave is acoustic velocity, $v_2 = \sqrt{\gamma_2 R_2 T_2}$. Equation (5.4) is the valance equation of the chemical reaction number r and Eq.(2.5) is the mass conservation of the fundamental element, c .

To obtain the electron density and the laser power density behind LSD wave for each time, Eqs.(5.1) ~ (5.1) are solved for $\ln T_2$, S , 2 , \widetilde{X}_s by using the improved Newton-Raphson method.^{5 4}

5.2 Thermodynamic Relationship

In LSD regime, the irradiated laser is first absorbed by the free electron through the inverse bremsstrahlung process and make the electron excite more highly energy state. The excited electron, however, dissipates its kinetic energy by colliding with the heavy particles and, as a result, decrease the electron temperature. On the other hand, the non-excited heavy particle, which does not acquire the laser energy directly, is excited by the colliding with the high-energy electron and, as a result, increase the heavy particle translational temperature. The electron temperature and the heavy particle temperature becomes finally equal after the so-called relaxation time. If the collision between the electron and the heavy particle occurs frequently enough to neglect the relaxation time in comparison with the time scale of the collision between the photon and the electron, one temperature model could be assumed. In this study, a simple one temperature model is applied for examining the validity of the thermal equilibrium assumption in LSD regime.

In the one temperature model, the internal energy and enthalpy of the species s is defined as the

following

$$e_s = \int_{T_{ref}}^T C_{v,s}(T) dT + \Delta e_s^f \quad (5.5)$$

$$h_s = \int_{T_{ref}}^T C_{p,s}(T) dT + \Delta h_s^f \quad (5.6)$$

Here, $C_{p,s} = C_{v,s} + R_s$ and in the case of $T_{ref}=0$, $\Delta h_s^f = \Delta e_s^f$. In this study, $T_{ref}=0$ is applied.

$C_{p,s}$ depends on the temperature because some energy mode begin to excite with the temperature increase, vibration mode and electric-excite mode in addition to the translational mode and the rotational mode. In this calculation, $C_{p,s}$ under 30000K and over 30000K is estimated from the following polynomial fitting function of the temperature respectively

$$C_{p,s} = R_s \sum_{k=1}^5 A_k^s T^{k-1} (T \leq 30000[K]) \quad (5.7)$$

$$C_{p,s} = a_s + b_s + \frac{c_s}{T^2} (T \geq 30000[K]) \quad (5.8)$$

5.3 Chemical Equilibrium Calculation

The assumption of the chemical equilibrium state is realized when the time to reach the chemical equilibrium state is small enough to neglect the characteristic time of the flow. If the collision frequency in LSD regime is high, the chemical reaction rate becomes high enough to the characteristic time of flow. Therefore, in this calculation, the assumption of the chemical equilibrium state is applied.

The considering species are the 11 species, N_2 , O_2 , NO , N , O , N_2^+ , O_2^+ , NO^+ , N^+ , O^+ and e^- . E.q.(5.4) needs $(n_{sp}-n_c)$ chemical equations, so in this case, 8 chemical equations, shown in Table 5.1, are needed. Table 5.2 shows the numbers of the fundamental element c in species s , ξ_s^c . Y_0^c is defined as follows.

$$Y_0^c = \sum_s \frac{\xi_s^c X_{s1}}{\rho_1} \quad (5.9)$$

X_{s1} is the mole number of the species s in the unite volume before the laser heating.

K_{eq} is obtained from the polynomial fitting expression of the temperature as the following.

$$\ln K_{eq}^r = A_{K_{eq}}^r Z^5 + B_{K_{eq}}^r Z^4 + C_{K_{eq}}^r Z^3 + D_{K_{eq}}^r Z^2 + E_{K_{eq}}^r Z + F_{K_{eq}}^r \quad (5.10)$$

$$Z = \ln \frac{10^4}{T} \quad (5.11)$$

Table 5.1: Chemical equations used in the equilibrium calculation in air with 11 species

No.	Reaction
1	$\text{N}_2 \rightleftharpoons 2\text{N}$
2	$\text{O}_2 \rightleftharpoons 2\text{O}$
3	$\text{NO} \rightleftharpoons \text{N} + \text{O}$
4	$\text{N} \rightleftharpoons \text{N}^+ + \text{e}^-$
5	$\text{O} \rightleftharpoons \text{O}^+ + \text{e}^-$
6	$\text{N} + \text{O} \rightleftharpoons \text{NO}^+ + \text{e}^-$
7	$2\text{O} \rightleftharpoons \text{O}_2^+ + \text{e}^-$
8	$2\text{N} \rightleftharpoons \text{N}_2^+ + \text{e}^-$

Table 5.2: Numbers of the fundamental element c in species s

Species	ζ^{N}	ζ^{O}	ζ^{e^-}
N_2	2	0	0
N_2^+	2	0	-1
NO	1	1	0
NO^+	1	1	-1
N	1	0	0
N^+	1	0	-1
O_2	0	2	0
O_2^+	0	2	-1
O	0	1	0
O^+	0	1	-1
e^-	0	0	1

5.4 Computational Results

The measured history of the displacement and the velocity of LSD wave with focusing lens, which f number is 2.2, in the atmospheric air are shown in Fig.5.2.and Fig.5.3. The timing of LSD termination is considered when shock front separates from the emission edge as shown in Fig.5.2. In this calculation, the measured history of LSD wave velocity as shown in Fig.5.3. Fig.5.4 were used. Fig.5.5 shows the calculated results of the electron density, the temperature behind LSD front and the laser power density irradiated on LSD wave surface. Figure 5.7 shows the mole fraction behind LSD front.

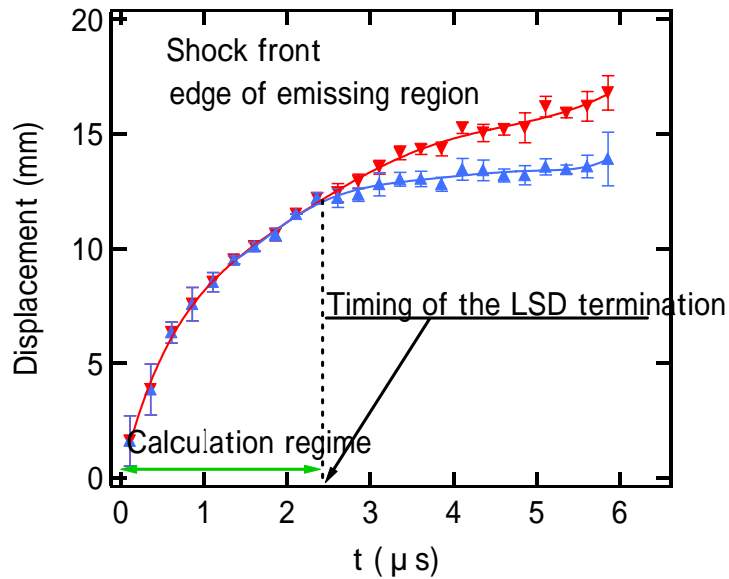


Figure 5.2: Measured history of LSD wave displacement and the timing of LSD termination with $f=2.2$ in the atmospheric air

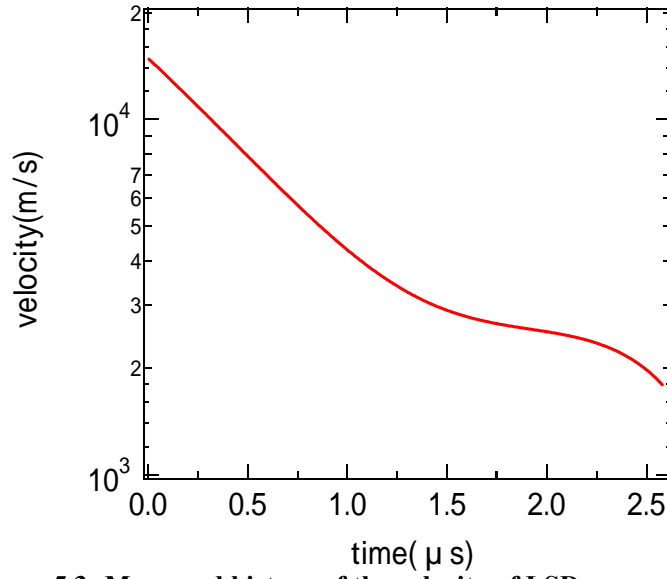


Figure 5.3: Measured history of the velocity of LSD wave with $f=2.2$ in the atmospheric air used in this calculation

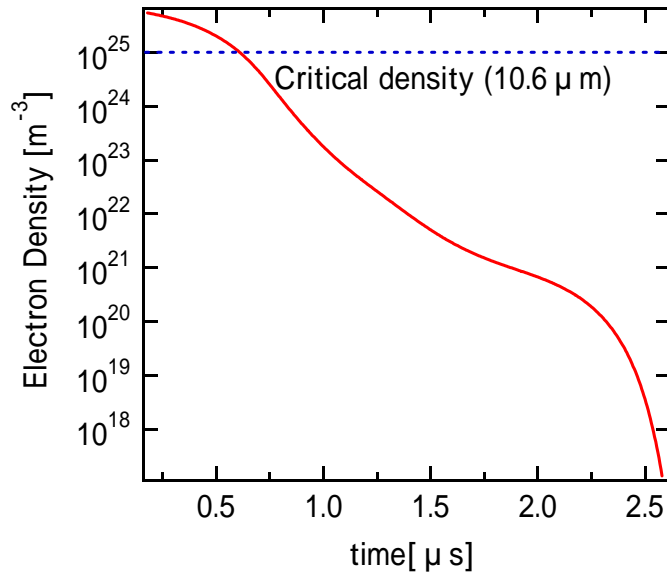


Figure 5.4: Calculated history of the electron density behind LSD wave front with the focusing lens with $f=2.2$ in atmospheric air and the critical density of the electromagnetic wave, which wavelength is 10.6 μ m.

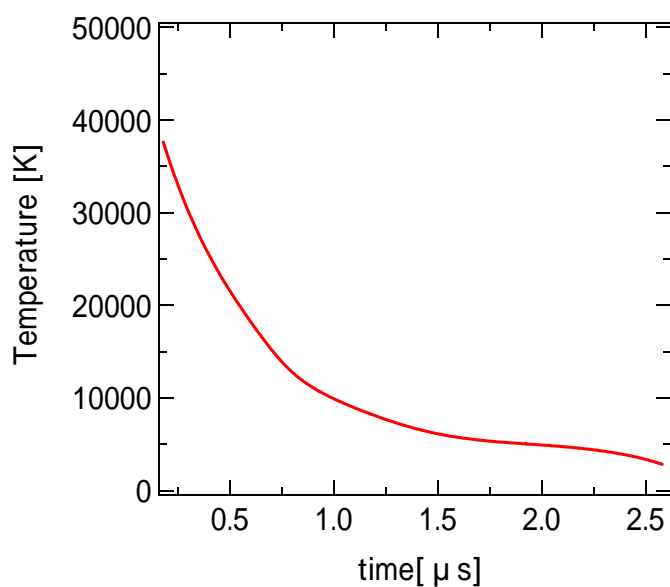


Figure 5.5: Calculated history of the temperature behind LSD wave front with $f=2.2$ in atmospheric air

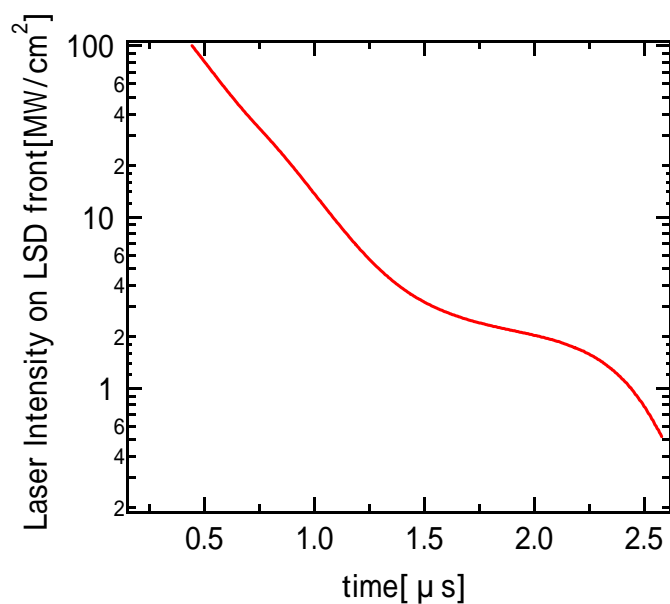


Figure 5.6: Calculated history of the laser power density irradiated on LSD wave front with $f=2.2$ in the atmospheric air

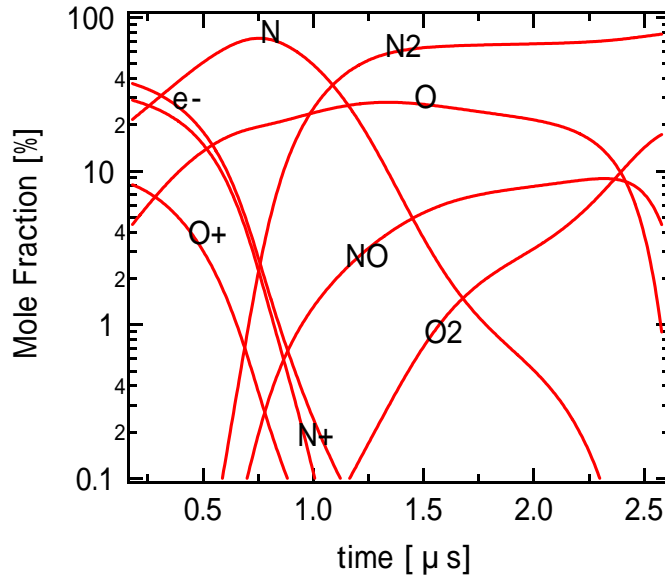


Figure 5.7: Calculated history of the mole fraction behind LSD wave front with $f=2.2$ in the atmospheric air

5.5 Discussion

The calculated electron density behind LSD wave front would be not enough to support LSD wave. One of the reasons for this disagreement between the calculated results and the experimental results is considered that the assumption of the chemical/thermal equilibrium state in LSD regime is inappropriate. The unsuitability for this assumption is supported by the fact that this calculated results is considered for the effects of the enthalpy flow by the radiation and the advection out from the laser absorption regime into its surrounding regime. Therefore, this effect is no longer the reasons of the disagreement between the calculated results and the experimental results.

Chapter6

Conclusion

- Interferometry method was applied to the measurement of the electron density in the LSD regime and laser absorption regime after the LSD termination. Although the electron density in the LSD regime could not be measured due to the strong refraction and absorption effect, the electron density in the laser absorption regime after the LSD termination could measure. The measured electron density was found to have the steep structure, which was considered as the remnant of the strong laser absorption region in the LSD regime.
- The decay process of the electron density gradient in the laser absorption regime after the LSD termination was considered to be dominated by two effects. One is the decrease in the electron density around the plasma front due to the electron diffusion and the photoionization by the radiative plasma regime and the other is the drastic temperature decrease due to the energy loss by the recombination radiation.
- The electron density behind the LSD front is calculated by using the measured velocity of the LSD front in the assumption of the chemical/thermal equilibrium. The calculated electron density in the LSD regime was much less than the measured electron density in the laser absorption regime after the LSD termination. In order to calculate the propagation of the LSD, thermal-nonequilibrium model should be adapted.

Reference

- ¹ *Space Factory on International Space Station*, ed by Ebisuzaki, T., Handa, T., and Takahashi, Y., Universal Academy Press, Tokyo, Japan, 2000.
- ² Glaser, P., “Power from the Sun: Its Future,” *Science Magazine*, Vol 162, 1968, pp 857-861.
- ³ Nishioka, K., Arno, R. D., Alexander, A. D., and Slye, R. E., “Feasibility of Mining Lunar Resources for Earth Use: Circa 2000 A.D., vols. I, II,” vol. 1, NASA TM X-62, 267; vol. 2, NASA TM X-62, 268, 1973.
- ⁴ Sutton, G. P. and Boblarz, O., *Rocket Propulsion Elements*, 7th ed., Wiley-Interscience, New York, 2000.
- ⁵ *Reducing Space Mission Cost*, ed. by Wertz, J., and Larson, W., Kluwer Academic Publishers, Boston, 1996.
- ⁶ http://spaceinfo.jaxa.jp/note/rocket/e/roc13_e.html
- ⁷ Kantrovitz, A. “Propulsion to Orbit by Ground Based Lasers,” *Aeronautics and Astronautics*, vol.10, 1972, pp. 74-76.
- ⁸ Hettche, L. R., Schriempf, J. T., and Stegman, R. L., “Impulse reaction resulting from the in-air irradiation of aluminum by a pulsed CO₂ laser,” *Journal of Applied Physics*, Vol. 44, 1973, pp. 4079-4085.
- ⁹ Pirri, A. N., Schler, R., and Northam, D., “Momentum transfer and plasma formation above a surface with a high-power CO₂ laser,” *Applied Physics Letters*, Vol. 21, 1972, pp. 79-81.
- ¹⁰ Simons, G. A., “Momentum Transfer to a Surface When Irradiated by a High-Power Laser,” *AIAA Journal*, Vol. 22, 1984, pp. 1275-1280.
- ¹¹ Simons, G. A., and Pirri, A. N. “The Fluid Mechanics of Pulsed Laser Propulsion,” *AIAA Journal*, Vol.15, 1977, pp. 835-842.
- ¹² Pirri, A. N., and Monsler, M. J., “Propulsion by Absorption of Laser Radiation,” *AIAA Journal*, Vol. 12, 1974, pp. 1254-1261.
- ¹³ Ageev, V. P., Barchukov, A. I., Bunkin, F. V., Konov, V. I., Korobeinikov, V. P., Putjatin, B. V., and Hudjakov, V. M., “Experimental and theoretical modeling of laser propulsion,” *Acta Astronautica*, Vol. 7, 1980, pp. 79-90.
- ¹⁴ Bohn, W. L. “Laser Lightcraft Performance,” *Proceedings of SPIE*, Vol. 3885, 2000, pp. 48-53.
- ¹⁵ Myrabo, L. M., Messitt, D. G., and Mead, Jr., F. B., “Ground and Flight Tests of Laser Propelled Vehicle,” *AIAA Paper* 98-1001, 1998.
- ¹⁶ Sasoh, A., “Laser-Propelled Ram Accelerator,” *Journal of Physics IV France*, Vol.10, 2000, pp.41-47.

-
- ^{1 7} Myrabo, L. N., Libeau, M. A., Meloney, E. D., Bracken, R. L., and Knowls, T. B., "Pulsed Laser Propulsion Performance of 11-cm Parabolic 'Bell' Engines Within the Atmosphere," AIAA paper 2002-2206, 2002.
- ^{1 8} Wang, T., Chen, Y., Liu, J., Myrabo, L. N., and Mead, F. B. Jr., "Advanced Performance Modeling of Experimental Laser Lightcraft," *Journal of Propulsion and Power*, Vol.18, 2002, pp. 1129-1138.
- ^{1 9} Bohn, W. L., and Schall, W. O., "Laser Propulsion Activities in Germany" in Proceedings of First International Symposium on Beamed Energy Propulsion (AIP Proceedings, Vol. 664) ed. by A.V. Pakhomov, 2003, pp. 79-91.
- ^{2 0} Sasoh, A., Kister, M., Urabe, N., and Takayama, K., "Laser-Powered Launch in Tube," *Transaction of Japan Society of Aeronautical and Space Sciences*, Vol. 46, 2003, pp. 52-54.
- ^{2 1} Katsurayama, H., Komurasaki, K., Momozawa, A., and Arakawa, Y., "Numerical and Engine Cycle Analysis of a Pulse Laser Ramjet Vehicle," *Transaction of JSASS Space Technology Japan*, Vol. 1, 2003, pp. 9-16.
- ^{2 2} Kalinin, V. P., Goryachkin, D. A., Gromovenko, V. M., Romanov, N. A., Rodionov, A. Y., Dimakov, S. A., Irtuganov, V. M., Kuprenyuk, V. I., Sherstobitov, V. E., and Rezunkov, Y. A., "Feasible configurations of a repetitively pulsed TEA CO₂ laser with small angular divergence and 1- kJ pulse energy," *Proceedings of SPIE*, Vol. 3574, 1998, pp. 187-202.
- ^{2 3} *Power Laser Technology*, ed. by Nakai, S., Ohm-sha, Tokyo, Japan, 1999 (in Japanese).
- ^{2 4} Ready, J. F., *Effect of High-Power Laser Radiation*, Academic Press, New York, 1979, p. 213.
- ^{2 5} Koichi, M., "Energy Conversion Processes in Air-Breathing Pulse-Laser Propulsion", Doctor Thesis, University of Tokyo, 2003.
- ^{2 6} Tomochika, M., Bachelor Thesis, University of Tokyo, 2000.(In Japanese)
- ^{2 7} Nobuyuki, H., Master Thesis, University of Tokyo, 2001. (In Japanese)
- ^{2 8} Yasuro, H., Master Thesis, University of Tokyo, 2003.(In Japanese)
- ^{2 9} Hiroshi, K., "Energy Conversion Process in a Pulse-Laser Boosted Vehicle and its Flight Performance", Doctor Thesis, University of Tokyo, 2004.(In Japanese)
- ^{3 0} Masato, U., Bachelor Thesis, University of Tokyo, 2003.(In Japanese)
- ^{3 1} Zel'dovich, Y. B., and Raizer, Yu. P., *Physics of Shock waves and High-temperature Hydrodynamics Phenomena*, Dover, New York, 2002, p340
- ^{3 2} Fischer, V. I., *Soviet Physics: Technical Physics*, Vol.28, 1984.
- ^{3 3} Nielsen, P. E., "Hydrodynamic calculations of surface response in the presence of laser-supported detonation waves," *Journal of Applied Physics*, Vol. 46, 1975, pp. 4501-4505.
- ^{3 4} Jumper, E. J., *Physics of Fluids*, Vol.21, 1978, p. 549.

-
- ^{3 5} Kazuyasu, M., "Compressible Flow Dynamics," *Rikougakusha*, p184, 1994.(In Japanese)
- ^{3 6} Batenin,V.M., Klimovskii,I.I.,Lysov,G.V., and Troitskii,V.N., "Superhigh Frequency Generators of Plasma", *CRC Press,Inc.*,2000.
- ^{3 7} Hiroyuki, S., "Numerical Analysis of Generation and Propagation Mechanism of Laser-Supported Detonation in Argon Gas", Doctor thesis, the university of Nagoya,2000.
- ^{3 8} K.Mori,K.Komurasaki, and Y.Arakawa, *J.Appl.Phys* 92,5663 (2002)
- ^{3 9} Harilal, S.S.,and Tillack,S.M., "Laser plasma density measurements usinginterfeerometry",p1, University of California, 2004.
- ^{4 0} Griem,H.R., "Principles of Plasma Spectroscopy",Cambridge University Press,Cambridge, United Kingdom, 1997
- ^{4 1} Katsunori, M., "Principle of Laser Thomson Scattering by Plamsas", plasma nuclear fusion, vol.78, 2000.(In Japanese)
- ^{4 2} Glenzer,S.H., "Thomson Scattering in Inertial Confinment Fusion Research"
- ^{4 3} Katsunori, M., and Mitsuo, M., "Applied Plasma Diagonostic",*Sangyoutosho*,Tokyo,1995.
- ^{4 4} Chen,F.F., "INTRODUCTION TO PLASMA PHYSICS AND CONTROLLED FUSION", p115,*Plenum Press*, New York, 1974
- ^{4 5} Houwing, F., and Takayama, K. "Automated interactive analysis of finite fringe interferograms including deconvolution of data from axisymmetric flows ", Internal Report for Institute of Fluid Science, Tohoku University, Sendai, Japan
- ^{4 7} Cameron, J.D., "One-dimensional tomography: a comparison of Abel, onion-peeling, and filtered backprojection methods",*Applied Optics*,Vol.31,No.8,1992.
- ^{4 8} Milan,K.,Keith, A.N., "Abel inversion using fast Fourier transforms", *Appllied Optics*,vol.27,No.10.
- ^{4 9} Toshihiko, O.,and Tomio,K., "LASERMETRICS",p81-82, *Shokabo*,Tokyo,2003.
- ^{5 0} Sedov,L.I., "Similarity and Dimensional Methods in Mechanism", *Academic Press*, New York,1959.
- ^{5 1} Wilson, R., "The spectroscopy of non-thermal plasmas," *J.Quant.Spectrosc. Radiat. Transfer*, Vol.2,pp.477-490,1962.
- ^{5 2} Raizer,Y.P., "Laser-Induced Discharge Phenomena ",pp.77-76,1972.
- ^{5 3} Lasndau,L.D. and Lifshitz, E.M., "Fluid Mechanica, 2nd ed.", Ch.14, *Butterworth-Heinemann*, Oxford,1978.
- ^{5 4} Botton,B.,Abeele,D.V.,Carbonaro,M. and Degrez ,G., "Thermodynamic and Transport Properties for Inductive Plasma Modeling ", *Journal of Thermophysics and Heat Transfer*, 13, 1999,

pp.343-350.

^{5 5} Gupta, R.N., Yos, J.M., Thompson R.A. and Lee, K.P., "A Review of Reaction Rates and Thermodynamic Transports Properties for an 11-Species Air Model for Chemical and Thermal Nonequilibrium Calculations to 30,000K ", *NASA, RP*, 1232, 1990.

^{5 6} Balakrishnan, A., "Correlation for Specific Heats of Air Species to 50,000K", *AIAA Paper*, 86-1277, 1986.

学会発表

- 平成 15 年度 衝撃波シンポジウム,千葉, 3 月
“*Measurement of Electron Density Behind Laser Induced Blast wave*”
- 24th International Symposium on space Technology and Science , Miyazaki, June
“*Measurement of Electron Density in RP-Laser Thruster Using Mach-Zehnder Interferometry*”
- 35th AIAA Plasmadynamics and Lasers Conference, Portland, Oregon, June
“*Electron Density Measurement of Laser Supported Detonation Wave*”
- 平成 16 年度宇宙輸送シンポジウム,神奈川, 1 月
“大気吸い込み型レーザー推進機におけるレーザー誘起プラズマの電子密度の測定”

誌上発表

- 平成 16 年度 『サイレント超音速飛行実現のための基礎実験・計算融合研究』・
『レーザー駆動管内加速装置：基礎物理の解明と実用展開』 合同シンポジウム,仙台,12 月
“*Clarification of the Laser Supported Detonation Wave Decay by Measuring the Electron Density Using the Interferometry*”

学会誌掲載

- 平成 15 年度衝撃波シンポジウム講演論文集 pp47-p50,2003
- Proceeding of 24th International Symposium on space Technology and Science, pp.216,2004
- AIAA paper ,2004-2565,2004
- 平成 16 年度 『サイレント超音速飛行実現のための基礎実験・計算融合研究』・
『レーザー駆動管内加速装置：基礎物理の解明と実用展開』 合同シンポジウム
発表論文集 pp.161-pp.164, 2004